The Bolocam Galactic Plane Survey: $\lambda = 1.1$ and 0.35 mm Dust Continuum Emission in the Galactic Center Region

John Bally[1], James Aguirre[2], Cara Battersby[3], Eric Todd Bradley[4], Claudia Cyganowski[5], Darren Dowell[6], Meredith Drosback[7], Miranda K Dunham [8], Neal J. Evans II [9], Adam Ginsburg[10], Jason Glenn[11], Paul Harvey[12], Elisabeth Mills [13], Manuel Merello [14] Erik Rosolowsky [15], Wayne Schlingman [16], Yancy L. Shirley [17], Guy S. Stringfellow[18], Josh Walawender[19], and Jonathan Williams[20]

[1]*CASA, University of Colorado, UCB 389, Boulder, CO 80309,*

John.Bally@casa.colorado.edu

[2]*Department of Physics and Astronomy, University of Pennsylvania, Philadelphia, PA ,*

jaguirre@sas.upenn.edu

[3]*CASA, University of Colorado, UCB 389, Boulder, CO 80309,*

Cara.Battersby@colorado.edu

[4]*Department of Physics and Astronomy, University of Central Florida, ,*

tbradley@physics.ucf.edu

[5]*Department of Astronomy, University of Wisconsin, Madison, WI 53706 ,*

ccyganow@astro.wisc.edu

[6]*Jet Propulsion Laboratory, California Institute of Technology, 4800 Oak Grove Dr. , Pasadena, CA 91104,*

cdd@submm.caltech.edu

[7]*Department of Astronomy, University of Virginia, P. O. Box 400325, Charlotesville, VA 22904,*

drosback@virginia.edu

[8]*Department of Astronomy, University of Texas, 1 University Station C1400, Austin, TX 78712,*

nordhaus@astro.as.utexas.edu

[9]*Department of Astronomy, University of Texas, 1 University Station C1400, Austin, TX 78712,*

nje@astro.as.utexas.edu

[10]*CASA, University of Colorado, UCB 389 Boulder, CO 80309,*

Adam.Ginsburg@colorado.edu

[11]*CASA, University of Colorado, UCB 389, Boulder, CO 80309,*

Jason.Glenn@colorado.edu

[12]*CASA, University of Colorado, UCB 389, Boulder, CO 80309,*

pmh@astro.as.utexas.edu

[13]*Department of Physics Astronomy, University of California, Los Angeles, Los Angeles, CA 90095,*

millsb@astro.ucla.edu

[14]*Department of Astronomy, University of Texas, 1 University Station C1400, Austin, TX 78712,*

manuel@astro.as.utexas.edu

[15]*Department of Physics and Astronomy, University of British Columbia, Okanagan, 3333 University Way, Kelowna BC V1V 1V7 Canada ,*

erik.rosolowsky@ubc.ca

[16]*Steward Observatory, University of Arizona, 933 North Cherry Ave., Tucson, AZ 85721 ,*

wschlingman@as.arizona.edu

[17]*Steward Observatory, University of Arizona, 933 North Cherry Ave., Tucson, AZ 85721 ,*

yshirley@as.arizona.edu

[18]*CASA, University of Colorado, UCB 389, Boulder, CO 80309,*

Guy.Stringfellow@colorado.edu

[19]*Institute for Astronomy (IfA), University of Hawaii, 640 N. Aohoku Pl., Hilo, HI 96720,*

joshw@ifa.hawaii.edu

[20]*Institute for Astronomy (IfA), University of Hawaii, 2680 Woodlawn Dr., Honolulu, HI 96822,*

jpw@ifa.hawaii.edu

ABSTRACT

The Bolocam Galactic Plane Survey (BGPS) data for a six square degree region of the Galactic plane containing the Galactic center is analyzed and compared to infrared and radio continuum data. The BGPS 1.1 mm emission consists of clumps interconnected by a network of fainter filaments surrounding cavities, a few of which are filled with diffuse near-IR emission indicating the presence of warm dust or with radio continuum characteristic of HII regions or supernova remnants. New 350 μm images of the environments of the two brightest regions, Sgr A and B, are presented. Sgr B2 is the brightest mm-emitting clump in the Central Molecular Zone and may be forming the closest analog to a super star cluster in the Galaxy. The Central Molecular Zone (CMZ) contains the highest concentration of mm and sub-mm emitting dense clumps in the Galaxy. Most 1.1 mm features at positive longitudes are seen in silhouette against the 3.6 to 24 μm background observed by the Spitzer Space Telescope. However, only a few clumps at negative longitudes are seen in absorption, confirming the hypothesis that positive longitude clumps in the CMZ tend to be on the near-side of the Galactic center, consistent with the suspected orientation of the central bar in our Galaxy. Some 1.1 mm cloud surfaces are seen in emission at 8 μm, presumably due to polycyclic aromatic hydrocarbons (PAHs). A $\sim$0.2° ($\sim$30 pc) diameter cavity and infrared bubble between $l \approx 0.0$° and 0.2° surrounds the Arches and Quintuplet clusters and Sgr A. The bubble contains several clumpy dust filaments that point toward Sgr A*; its potential role in their formation is explored.

Bania's Clump 2, a feature near $l = 3$° to 3.5° which exhibits extremely broad molecular emission lines ($\Delta V > 150$ km s^{-1}), contains dozens of 1.1 mm clumps. These clumps are deficient in near- and mid-infrared emission in the Spitzer images when compared to both the inner Galactic plane and the Central Molecular Zone. Thus, Bania's Clump 2 is either inefficient in forming stars or is in a pre-stellar phase of clump evolution.

The Bolocat catalog of 1.1 mm clumps contains 1428 entries in the Galactic center between $l = 358.5$° to $l = 4.5$° of which about 80% are likely to be within about 500 pc of the center. The mass-spectrum above about 80 M$_\odot$ can be

described by a power-law $\Delta N/\Delta M = N_0 M^{-2.14(+0.1,-0.4)}$. The power-law index is somewhat sensitive to systematic grain temperature variations, may be highly biased by source confusion, and is very sensitive to the spatial filtering inherent in the data acquisition and reduction.

Subject headings: Galaxy: center (ISM): clouds (ISM): dust, extinction stars: formation surveys-

1. Introduction

The formation of massive stars and star clusters remains one of the outstanding problems in star formation research (Stahler et al. 2000; Bally & Zinnecker 2005). The Central Molecular Zone (CMZ) of our Galaxy, located within about 500 pc of the nucleus, contains about 5 to 10% of the molecular gas mass and the largest concentration of massive stars and star clusters in the Milky Way (Morris & Serabyn 1996; Ferrière et al. 2007). The CMZ hosts two of the most massive, densest, and remarkable star forming complexes in the Milky Way, Sgr A and Sgr B2 (Yusef-Zadeh et al. 2008, 2009). Giant molecular clouds (GMCs) in the CMZ are one to two orders of magnitude denser and have over an order of magnitude larger line-widths than typical GMCs in the Galactic plane beyond 3 kpc from the nucleus (Bally et al. 1987, 1988; Oka et al. 1998; Tsuboi et al. 1999; Oka et al. 2001b). The study of the interstellar medium in the CMZ and the immediate vicinity of the central black hole is an essential step towards understanding star and cluster formation in extreme environments such as starburst galaxies and active galactic nuclei. The CMZ may be a Galactic analog of the nuclear star-forming rings observed in the centers of star forming barred galaxies (Kormendy & Kennicutt 2004; Kormendy & Cornell 2004; Liszt 2009).

The Galactic plane just outside the CMZ between $l = 1.3°$ to $5°$ contains several remarkable, localized cloud complexes with unusually large velocity extents. Longitude-velocity diagrams in species such as HI, CO, and high-density gas tracers such as CS and HCO$^+$ show that near $l = 355°$, $1.3°$, $3°$, and $5°$, these cloud complexes have velocity extents of 100 to 200 km s^{-1} in regions less than $0.5°$ (~ 75 pc) in diameter (Dame et al. 2001; Liszt 2006, 2008). These remarkable cloud complexes may trace the locations where gas is entering the dust lanes at the leading edges of the bar in the center of our Galaxy and passing through a series of shocks (Liszt 2006), or dust lanes along the bar's leading edge seen nearly end-on.

A crucial step in the observational study of massive star and cluster formation is the identification and characterization of clumps that will soon form or are actively forming stars, without biases introduced by targeting sources with already known signposts of star

formation such as masers, IR sources, or HII regions. Massive stars and clusters form from cool high-density clumps with very large column densities and extinctions that can sometimes exceed $A_V = 100$ magnitudes. Such clumps are best investigated at millimeter and sub-millimeter wavelengths. Spectral lines provide excellent diagnostics of line-of-sight motions in a cloud. However, the interpretation of various gas tracers that produce emission lines in this portion of the spectrum can be very difficult. Variations in tracer abundances caused by depletions and complex chemical processing, uncertainties in excitation conditions, and the impacts of radiation fields and shocks make the derivation of column densities, masses, and other physical properties of clumps highly uncertain.

The continuum emission from warm dust provides a somewhat more reliable tracer of the column density and clump masses. At 1.1 mm, $h\nu/k \approx 13$ K, and most sources are expected to be optically thin. Thus, the column density is roughly proportional to the temperature and optical depth of the emitting medium. Shorter wavelength observations can be more difficult to obtain due to lower atmospheric transmission and greater variations in sky emission ("atmospheric" or "sky noise"). Furthermore, the stronger dependence of column density on temperature when $h\nu/k > T_{dust}$ makes the derivation of physical parameters more difficult.

Contamination of the dust continuum emission in the Bolocam 1.1 mm filter by spectral lines and free-free emission is likely to be small, less than a few percent in almost all cases. As discussed in detail in Aguirre et al. (2010), the Bolocam 1.1 mm filter excludes the bright 1.3 mm CO lines. In the worst case, that of the hot cores in Sgr B2, contamination by other spectral lines can account for at most 20% of the detected 1.1 mm flux. Such spectral line emission is much weaker in the other clumps. Contamination by free-free emission would only occur from ultra-compact HII regions. However, such objects tend to be only a few arc-seconds in diameter, and will be beam diluted and completely overwhelmed by the larger-angular scale dust continuum. Comparison of the 20 cm radio continuum emission (see discussion of Figure 11 below) shows that 20 cm radio and 1.1 mm dust continuum emission are not correlated, supporting the argument that there is little contamination of the 1.1 mm fluxes by free-free emission.

This paper presents two new data sets obtained with the 10.4 meter Caltech Submillimeter Observatory; 1.1 mm continuum observations obtained with Bolocam, and 350 μm data obtained with SHARC-II. These data are compared with a variety of previously published infrared and radio continuum data. The new data presented here are part of a 1.1 mm continuum Bolocam Galactic Plane Survey (BGPS) (Aguirre et al. 2010; Rosolowsky et al. 2009; Dunham et al. 2009) that has mapped about 170 square degrees of the northern Galactic Plane. The BGPS data were released into the public domain on 24 June 2009 through the

Infrared Processing and Analysis Center (IPAC) at the California Institute for Technology (http://irsa.ipac.caltech.edu/data/BOLOCAM_GPS/).

This paper presents an analysis of BGPS clumps in the region between $l = 358.5$ and $+4.5°$ which contains the Galactic nucleus, the Central Molecular Zone (CMZ) of dense, turbulent, and warm molecular clouds (Morris & Serabyn 1996), and the most prominent high-velocity-dispersion cloud complex, Bania's Clump 2 (Stark & Bania 1986) located at $l = 3.2°$. Additionally, 350 μm images are presented of the two most luminous star forming complexes in the CMZ, Sgr A and its neighboring cloud complexes, and the Sgr B2 region. Previous (sub)millimeter studies of the Galactic center (Lis et al. 1991, 1994; Lis & Carlstrom 1994; Lis & Menten 1998; Lis et al. 2001) tend to be based on maps of small fields. The wide-field BGPS data are presented and compared to images obtained with the Spitzer Space Telescope at 3.6 to 8.0 μm (Arendt et al. 2008) and Spitzer 24 μm images now in the public domain (Yusef-Zadeh et al. 2009). BGPS is also compared with the SCUBA / JCMT 450 and 850 μm dust continuum maps (Pierce-Price et al. 2000) from an approximately 2° by 0.5° region containing the CMZ. Finally, the 1.1 mm data are compared with the 20 cm radio continuum (Yusef-Zadeh et al. 2004) to constrain recent and on-going massive star formation activity in the CMZ and Bania's Clump 2.

This paper is organized as follows: Section 2 describes the observations and analysis methods, including a discussion of mass estimation (Section 2.1), and the determination of dust properties for the two fields where 350 μm observations are presented (Section 2.2). Section 3 presents the observational results. Section 3.1 presents a discussion of clump mass spectra extracted from the Bolocat catalog (Rosolowsky et al. 2009). Section 3.2 describes the emission from the Central Molecular Zone containing the Sgr A, B1, B2, and C complexes and its relationship to objects detected at other wavelengths. Section 3.3 presents a more detailed discussion of the environment of Sgr A. Section 3.4 presents a discussion of the emission along the inner Galactic plane and Bania's Clump 2. Section 3.5 presents a short discussion of features likely to be located in front of or behind the center of the Galaxy in the Galactic plane. Section 4.1 explores the energetics of the cavity in the Sgr A region. Section 4.2 discusses the clumps that may be fueling star formation in Sgr A. Section 4.3 discusses the low star formation rate in Bania's Clump 2. Conclusions are presented in Section 5. Detailed descriptions of some of the brighter or otherwise more noteworthy sources are given in an Appendix. A tabulation of Bolocat clumps located within the field of view covered by Figure 1 and 2 along with their derived properties is given in Table 3 in the electronic version of this paper.

2.   Observations

The observations reported here were obtained with Bolocam[1] between June 2005 and July 2007 on the Caltech Submillimeter Observatory (CSO) 10-meter diameter telescope. SHARC-II observations were obtained during the best weather on these observing runs and in April 2008. The observations used in this paper were obtained on the dates listed in Table 1.

Bolocam (Glenn et al. 2003) is a 144-element bolometer array with between 110 and 115 detectors working during the observations reported here. The instrument consists of a monolithic wafer of silicon nitride micromesh AC-biased bolometers cooled to 260 mK. All data were obtained with a 45 GHz bandwidth filter centered at 268 GHz ($\lambda = 1.1$ mm) which excludes the bright 230 GHz J=2-1 CO line. However, as discussed in Aguirre et al. (2010), the effective central frequency is 271.1 GHz. The individual bolometers are arranged on a uniform hexagonal grid. Each bolometer has an effective Gaussian beam with a FWHM diameter of $31''$, but the maps presented here have an effective resolution of $33''$ due to beam-smearing by the scanning strategy, data sampling rate, and data reduction as discussed by Aguirre et al. (2010). At an assumed distance of 8.5 kpc to the Galactic center, the $33''$ diameter Bolocam effective resolution corresponds to a length-scale of 1.36 pc and $1°$ corresponds to about 148.7 pc. The instantaneous field-of-view (FOV) of the focal-plane array is $7'.5$ but the effective filter function limits spatial frequency sensitivity to about $3'$ to $5'$. Bolocam observations were only obtained when atmospheric conditions were clear with a 225 GHz zenith opacity ranging from 0.06 to 0.15. During better observing conditions, 350 μm SHARC-II observations were obtained as discussed below.

Data were obtained by raster-scanning Bolocam on the sky at a rate of $120''$ per second. Each 'observation' consisted of three pairs of orthogonal raster-scans each covering a full square-degree or a $3°$ by $1°$ field in Galactic coordinates with scan-lines separated by $162''$ on the sky. The second and third pairs of orthogonal raster-scans were offset from the first pair by $\pm 42''$. Four to over a dozen 'observations' taken on different days were averaged to obtain the maps presented here.

The Bolocam raw data were reduced using the methods described in detail in Aguirre et al. (2010) based on the earlier techniques described in Enoch et al. (2006) and Laurent et al. (2005). The new reduction pipeline handles the large dynamic range and complex structure characteristic of Galactic star forming regions better. In summary, real-time pointing data were merged with the time-series data from each bolometer whose exact location in the

---

[1]http://www.cso.caltech.edu/bolocam

CSO focal-plane is known. Principal component analysis (PCA) is used to remove signals common to all bolometer channels, such as the DC level from atmospheric loading and sky brightness fluctuations. Simulations have shown that for data containing faint sources which are sparsely distributed, the removal of the first three orthogonal PCA components suffices to correct for atmospheric effects produced by sky noise (see Enoch et al. 2006 for details). However, in the Galactic plane the presence of bright ($>$ few Jansky) sources and crowding required the removal of 13 PCA components. Following removal of signals attributed to the atmosphere, the maps are then "iteratively mapped" to restore astronomical structure on angular scales comparable to the size of the Bolocam array (Enoch et al. 2006; Aguirre et al. 2010). The final data were sampled onto a uniform $7''.2$ grid. The data were flux calibrated using observations of the planets Mars, Uranus, and Neptune. In the Galactic center fields presented here, the 3 σ r.m.s. noise is about 40 mJy beam^{-1}.

The V1.0 data released at the IPCA site use $7''.2$ pixels. The data value in each pixel corresponds to the flux measured at that location on the sky by the $33''$ effective beam and is in units of Jy/beam. The area under a $33''$ gaussian beam is the same as the area under a top-hat beam with a radius of $r_B = FWHM/(4ln2)^{1/2} = 19.8''$ or an aperture with a diameter of $\approx 40''$. There are $\pi r_B^2/7.2^2 = 23.8$ pixels in such an aperture. Thus, to convert the data in the V1.0 images from Jy/beam to Jy/pixel where each pixel is a $7''.2$ square, divide the data by 23.8. To measure the total flux over some aperture, sum the pixels values in the aperture (after converting to Jy/pixel units).

Only flux produced by structure smaller than about one-half of the Bolocam array-size of approximately $7.5'$ can be measured reliably. Larger-scale emission smoothly distributed in 2 dimensions is under-represented. However, long filaments or structure in which at least one dimension is compact compared to the Bolocam array size can be recovered. A more detailed discussion of the spatial transfer-function of the BGPS is given in Aguirre et al. (2010).

Comparison between Bolocam and 1.2 mm data acquired with two other instruments, MAMBO on the IRAM 30 meter (Motte et al. 2003, 2007) and SIMBA on the SEST (Matthews et al. 2009) 15 meter, are presented in Aguirre et al. (2010). (Aguirre et al. 2010) find that the BGPS Version 1.0 Bolocat and image data release nead a mean correction factor of 1.5 to be applied to align BGPS fluxes with these previous measurements and to yield dust spectral indices when compared to data at other wavelengths.

During the very best weather conditions at the CSO when the zenith sky opacity at 225 GHz was less than about 0.06, observations of selected fields were obtained at 350 μm with the 384 element SHARC-II focal plane array (Dowell et al. 2003). SHARC-II consists of a 12 by 32 pixel array of "pop-up" bolometers providing an effective resolution (beam diameter) of

about $9''$ on the CSO. The SHARC-II 350 μm filter is matched to the atmospheric window in this part of the spectrum and has an effective passband of $\Delta\lambda/\lambda = 0.13$ (111 GHz) centered at λ 350 μm.

Observations of five slightly overlapping fields in the Sgr A region were obtained in June 2005 using 10$'$ by 10$'$ BOX_SCANs. A second set of observations were obtained on 6 April 2008 using a 30$'$ by 30$'$ BOX_SCAN covering the fields near Sgr A using a scan rate of 60$''$ per second for a total integration time of 40 minutes. The Sgr B2 observations were obtained on 31 March 2004 with a 13$'$ $\times$ 15$'$ BOX_SCAN with a scan-rate of 30$''$ per second. The total integration time was 20 minutes. While the June 2005 data were reduced with the facility software package, CRUSH (Kovács 2008), the 350 μm images shown in the figures were processed with the code SHARCSOLVE written by co-I Dowell. Minimal filtering was used; many iterations fit only an offset and gain to each bolometer time-stream, a spatially flat atmospheric signal at each time, ending with a few iterations of fitting an atmospheric gradient over the detector array.

Due to their better uniformity, only the March 2004 and April 2008 images are used in the figures. The June 2005 observations were used as an independent check on flux calibration and image fidelity. Although there are slight differences in the background intensities, the overall structure of the emission during the two epochs agrees extremely well. The flux calibration on compact objects such as G359.984,-0.0088] agrees to within 10% (29 vs 32 Jy/beam) once an annular background is subtracted. The 3σ sensitivity of these observations is about 1Jy/beam at 350 μm.

2.1. Mass and Column Density Estimation

Estimation of the dust column densities and masses from the 1.1 mm emission requires knowledge of the dust properties such as emissivity, spectral index, and temperature, which requires input from additional data. Column densities, densities, and masses are estimated for a subset of the brightest clumps based on dust parameters appropriate for the Solar neighborhood (Table 2). Masses, column densities, and densities estimated for all Bolocat entries are tabulated in Table 3 in the electronic version of this paper. For all mass estimation given in this paper, the images and fluxes reported in the V1.0 data release have been multiplied by an empirically determined scaling factor of 1.5 as discussed above.

The mass within the 33$''$ BGPS effective beam (or equivalently, in a 40$''$ diameter circular aperture) is given by

$$M = \frac{1.0 \times 10^{-23} \, S_{1.1}(Jy)D^2}{\kappa_{1.1}B_{1.1}(T)}$$

where $B_{1.1}(T)$ is the Planck function for dust temperature T, and $\kappa_{1.1}$ is the dust opacity at $\lambda = 1.1$ mm in units of cm^2 g^{-1}. As a function of wavelength, $\kappa_\lambda = \kappa_0(\lambda_0/\lambda)^\beta$ where β is the dust emissivity. Hildebrand (1983) calibrated κ at $\lambda = 0.25$ mm, giving a value $\kappa_{0.25} = 0.1$ cm^2 g^{-1} for interstellar dust and a gas-to-dust ratio of 100. For $\beta = 1.5$, the Hildebrand opacity implies $\kappa_{1.1} = 1.08 \times 10^{-2}$ cm^2 g^{-1}. Ossenkopf & Henning (1994) (OH94) calculated the opacity of grains with ice mantles that have coagulated for 10^5 years at a gas density of 10^6 cm^{-3}. Enoch et al. (2006) interpolated logarithmically the OH94 opacities to obtain $\kappa_{1.1} = 1.14 \times 10^{-2}$ cm^2 g^{-1}, close to the estimate based on the Hildebrand opacity. As discussed in Aguirre et al. (2010) the effective central frequency of the Bolocam 1.1 mm filter is 271.1 GHz. Log-interpolating the OH94 opacity at 1.00 mm to this frequency implies $\kappa_{1.1} = 1.14 \times 10^{-2}$ cm^2 g^{-1}. Adopting this value gives

$$M = 14.26(e^{13.01/T(K)} - 1)S(Jy)D_{kpc}^2 \qquad (M_\odot)$$

where D_{kpc}^2 is in units of 1.0 kpc and T is in Kelvin.

The greater metallicity of the Galactic center may result in a larger dust opacity, and possibly a different dust emissivity law. This effect has not been taken into account in the present analysis. The spatial filtering inherent in BGPS, and large uncertainties inherent in the estimation of masses using spectral lines, it is not at present possible to determine clump masses with sufficient precision to detect a difference in the dust properties. Use of a larger dust opacity would decrease the estimated masses and column densities given here.

The dust temperature in the Central Molecular Zone has been studied by Sodroski et al. (1994) who used COBE/DIRBE 140 to 240 μm data to conclude that 15 to 30% of the emission arises from molecular clouds with temperatures of about 19 K, 70 to 75% arises from the HI phase with a dust temperature of 17 to 22 K and less than 10% comes from ~ 29 K dust in the extended HII phase. Rodríguez-Fernández et al. (2004) used the Infrared Space Observatory (ISO) to study a representative sample of 18 molecular clouds not associated with prominent thermal radio continuum emission. They found typical dust temperatures, measured from $\lambda = 40$ to 190 μm, required a combination of a cold, 15 K component and a warm component with a temperature ranging from 27 to 42 K. Thus, in the analysis presented here, the dust column densities and masses are parameterized in terms of a fiducial dust temperature of 20 K. For T = 20 K,

$$M = 13.07 \, S(Jy)D_{kpc}^2 \qquad (M_\odot)$$

which at the 8.5 kpc distance to the Galactic center gives $M = 944 \, S(Jy) \, M_\odot$. This mass can be converted to a column density averaged over the beam,

$$N(H_2) = \frac{M}{\pi \mu_{H2} m_H r_B^2} \qquad (cm^{-2})$$

where M is in grams, $\mu_{H2} = 2.8$ is the mean molecular weight per hydrogen molecule (Kauffmann et al. 2008), $r_B = D_{GC} \times FWHM/(205265 \times \sqrt{4 \, ln2})$ is the effective beam radius in centimeters at the Galactic center, and $D_{GC} = 8.5$ kpc. Following Kauffmann et al. (2008), the mean molecular weight per particle, $\mu_p \approx 2.37$ should be used when estimating quantities such as collision rate or pressure. For BGPS, $FWHM \approx 33''$, giving effective beam radius or $R_B = 19.8''$, which at a distance of 1 kpc corresponds to $r_B(kpc) = 2.97 \times 10^{17}$ cm and at the distance to the Galactic center is $r_B = 2.52 \times 10^{18}$ cm. The resulting column density per beam is

$$N(H_2) = 2.19 \times 10^{22}[e^{13.0/T(K)} - 1] \, S(Jy) \approx 2.0 \times 10^{22} \, S(Jy) \qquad (cm^{-2})$$

where the right side was evaluated for T = 20 K. This column density corresponds to a visual extinction of $A_V \approx 10.7$ magnitudes assuming the usual Bohlin & Savage conversion of $N(H) = 1.9 \times 10^{20} \, cm^{-2}$ per visual magnitude in the standard Johnson / Cousins V filter centered at 0.55 μm . These column densities can be converted into surface densities; $\Sigma(g \, cm^{-2}) = 4.65 \times 10^{-24}N(H_2)$ or $\Sigma(M_\odot \, pc^{-2}) = 0.048A_V$.

For extended sources, masses are given by $M = \mu m_H N(H_2)A_S$ where A_S is the area subtended by the aperture used to estimate the flux. At the Galactic center, the mass is given by $M_{tot} = 944 \, \langle S_{1.1}(Jy) \rangle \, [\Omega_S/\Omega_B] \, M_\odot$ where $< S_{1.1}(Jy) >$ is the flux averaged over the solid angle Ω_S subtended by the measurement aperture and $\Omega_B = \pi r_B^2 \approx 2.9 \times 10^{-8}$ is the BGPS beam solid angle in steradians. A temperature of $T = 20$ K is assumed to evaluate the numerical coefficient.

An estimate of the volume density can be made by assuming that each clump is spherical and uniformly filled with emitting matter. Table 2, columns 9 and 10 give the densities estimated from the fluxes measured in $40''$ and $300''$ diameter apertures under the assumption that each clump is either $40''$ or $300''$ in diameter. Interferometric measurement of clumps in the Solar vicinity show that much of the millimeter continuum emission arises from regions having diameters of order 10^3 AU or less. Thus, BGPS clumps are likely to consist of clusters of unresolved objects much smaller than the beam. The BGPS-based density estimates are volume averaged quantities. Inside cores, the densities are likely to be much higher while in-between cores, densities may be lower.

Table 2 lists the locations, fluxes, masses and densities for a sample of regions, many of which are marked in Figure 9. S_{40} gives the flux measured with the FWHM = $33''$ Bolocam effective resolution at the location of the brightest emission in each source. The uncertainties in the listed quantity range from about 20% to over 30% for bright sources due to a combination of calibration errors, and incomplete flux recovery in the iterative mapping phase of data reduction. The 1.1 mm images have also been smoothed with a "tophat" function having a 20 pixel radius to provide an estimate of the total flux produced

by extended objects in a $300''$ diameter, circular region. At the distance of the Galactic center (8.5 kpc), these masses are given by $M(300) = 5.0 \times 10^4 \ S_{300}(Jy)$ M$_\odot$ for 20 K dust where $S_{300}(Jy)$ is the average flux density in the $300''$ aperture. (Note that for several high-latitude regions suspected to be in the foreground, a distance of 3.9 kpc is assumed in estimating masses as indicated in the comments column.) These mass estimates are lower bounds because they only refer to the flux in small-scale structure to which Bolocam is most sensitive. Because BGPS data starts to lose sensitivity to structure on scales ranging from $3'$ to $6'$, $300''$ is the largest aperture for which reliable photometry can be obtained. As discussed below, comparison of mass determinations in the $300''$ aperture to previously published measurements for regions such as Sgr A and Sgr B2 agree to within the estimated uncertainties.

2.2. Dust Properties From 350 μm and 1.1 mm data

Two fields around Sgr A and Sgr B2 were observed at 350 μm. The 350 μm to 1100 μm flux ratio can be used to constrain dust temperatures or emissivities. Three corrections must be applied to the SHARC-II data prior to comparisons with BGPS; matching of angular resolution, correction for signals-picked up in the sidelobes, and matching of the spatial frequency response functions. No correction has been made for contamination by spectral lines.

The SHARC-II 350 μm images were obtained with a $9''$ FWHM beam. Thus, they have to be convolved with a gaussian function with $\sigma = 13.5''$ to match the $33''$ effective BGPS beam. Because the data values in both the 350 and 1100 μm images are in units of Janskys per beam, the pixel values in the convolved SHARC-II images must be multiplied by the ratio of beam areas (13.4 when scaling from $9''$ to a $33''$ beam).

Inspection of the 350 μm beam delivered by the CSO on bright point sources such as planets shows that in addition to the main $9''$ beam, there is a low-level error pattern several arc-minute diameter with a roughly hexagonal shape. The main-beam efficiency of the CSO at 350 μm is only about 0.4 ± 0.15. In a complex field such as the Galactic center with an abundance of bright, extended emission, fluxes will be over-estaimated when compared with a point source calibrator in the main beam due to the signal entering the sidelobes. Because bright emission near both Sgr A and Sgr B2 is extended on scales of many arc-minutes, we assume that about 30% of the signal at a typical location in the maps arises from signal picked up in the sidelobes. As an approximate correction for this effect, we scale the convolved 350 μm images by a factor 0.7 to correct for clumps contributing emission through the side-lobes.

Comparison of the two 350 μm maps of the Sgr A region discussed above shows that the rapidly-scanned SHARC-II images recover flux on larger angular scales than the 1.1 mm BGPS images. Thus, the SHARC-II images are spatially filtered with an "unsharp mask". The mask in constructed by convolving the 350 μm with a gaussian function having a kernel σ_k, and subtracting a fraction, f of the mask from the original image. The optimal values of σ_k and f were chosen by finding the closest match between the spatial structure of the resulting "unsharp-masked" SHARC-II image with the corresponding BGPS image. For the Sgr A field, the best choice is $\sigma_k = 90''$ (FWHM $= 212''$) and $f = 0.8$; for Sgr B2, $\sigma_k = 68''$ (FWHM $= 160''$) and $f = 0.5$. The beam-matched, spatially filtered 350 μm images were divided by the corresponding 1.1 mm BGPS images to form flux-ratio maps.

The observed intensity of continuum emission at each location in a map is given by $S_\nu = \Omega_{beam}[1 - e^{-\tau_\nu d}]B_\nu(T)$ (Jy) where $\Omega_{beam} \approx 2.9 \times 10^{-8} sr$ is the beam solid angle corresponding to the $33''$ effective resolution of the 1.1 mm data and the convolved, beam-matched, 350 μm observations, τ_ν is the optical depth of the emitting dust, and $B_\nu(T)$ is the Planck function at each frequency. The optical depth in the sub-mm to mm regime scales with frequency as ν^β where β is the emissivity power-law index. For small grains, β is close to 2 in the mm to sub-mm regime but can be smaller if the grains have experienced substantial growth or are coated by ice mantles (Ossenkopf & Henning 1994). In the optically thin limit, the flux-ratio at each point in a ratio map is given by

$$R = S_{350\mu m}/S_{1.1mm} = \frac{\nu_{350}^{3+\beta}[exp(h\nu_{1.1}/kT_d) - 1]}{\nu_{1.1}^{3+\beta}[exp(h\nu_{350}/kT_d) - 1]}$$

which can not be solved analytically for T_d. A look-up table is generated for each choice of β and T_d and used to analyze points in the ratio maps. For hot β=2.0 dust where both 350 μm and 1100 μm are in the Rayleigh-Jeans limit, the observed intensity ratio should be around $R = 100$. Larger ratios require $\beta > 2$. Where the pixels have good signal at both 350 μm and 1.1mm, flux ratios have values $R < 70$, corresponding to dust temperatures less than 70 K for $\beta = 2$ dust. The interpretation of these results will be discussed below.

3. Results

The inner two degrees of the Galactic plane (Figures 1 and 2) contain the brightest millimeter-wave continuum emission in the sky. The Central Molecular Zone (CMZ, which consists of the high-surface brightness region between $l \approx 359°$ to $1.8°$) has a radius of about 200 to 300 pc and contains the highest concentration of dense gas and dust in the Galaxy (Morris & Serabyn 1996).

Figure 3 shows an image of the peak antenna temperature of the ^{12}CO J = 1 – 0 line taken from the data set presented by Bally et al. (1987, 1988). Comparison of Figures 1 through 3 and maps of dense gas tracers such as CS (Miyazaki & Tsuboi 2000) shows that the brightest 1.1 mm continuum emission is closely associated with the brightest CO and CS emission.

Figure 4 shows the spatial-velocity behavior of CO-emitting gas at positive latitudes integrated from $b = 0.20$ to $0.48°$. Emission from the Galactic disk is confined to velocities between $V_{LSR} = -70$ and $+10$ km s^{-1} and can be distinguished from the Galactic center gas by its relatively narrow line-widths of order $\Delta V \sim$ few km sec^{-1}. Foreground CO emission is mostly associated with the nearby Sagittarius Arm (near $V_{LSR} = 0$ km s^{-1}), the Scutum-Centaurus Arm (near $V_{LSR} = -35$ km s^{-1}), and the 3 kilo-parsec Arm (near $V_{LSR} = -60$ km s^{-1}). The systematic progression in (negative) radial velocity as one approaches the Galactic center provides evidence for the presence of a central bar (Binney et al. 1991). The high velocity CO feature (near $V_{LSR} = 100$ to 200 km s^{-1}) between $l = -1.5°$ and $+2°$ has been called the "expanding molecular ring" (EMR) which in the barred models of the Galaxy is interpreted as gas in x_1 orbits located mostly along the leading edge of the central bar (labeled as "leading edge of the bar" in Figure 4) whose positive longitude side is thought to be closer to us (Morris & Serabyn 1996). The major axis of the bar is thought to have an angle with respect to our line-of-sight between $20°$ to $45°$ (Binney et al. 1991; Bissantz et al. 2003; Ferrière et al. 2007; Pohl et al. 2008).

Figures 3 and 4 show the remarkable molecular feature known as Bania's Clump 2 (Stark & Bania 1986). This feature is localized to a roughly 1/2 degree diameter ($\sim$70 pc) region in the spatial direction. But, as illustrated by Figure 4, it extends over a velocity range of order 200 km s^{-1}. Figures 1 and 2 show that Bania's Clump 2 is prominent at 1.1 mm, consistent with the previous detection of emission by high density gas tracers. Throughout the Galactic plane, bright dust continuum sources generally indicate the presence of embedded massive stars or clusters. But, as discussed below, there is virtually no massive star or cluster formation in this region as indicated by the lack of infrared and radio continuum emission.

The 1.1 mm data presented here are qualitatively similar to the recent ATLASGAL survey of the Galactic plane conducted with the LABOCA array on the APEX 12 meter diameter telescope in Chile at a wavelength of 870 μm (Schuller et al. 2009). Although the angular resolution of ATLASGAL is nearly a factor of two better than BGPS, the images presented in Schuller et al. (2009) show similar structures to what is seen in BGPS. Specifically, the CMZ and Bania's Clump 2 dominate the emission in the region between $l = 358.5°$ and $4.5°$. A quantitative comparison of fluxes in ATLASGAL, BGPS, and eventually

Herschel Space Observatory images, will enable the measurement of dust temperatures and emissivities.

3.1. Clump Mass Spectra in the Galactic center

The Bolocat clump catalog contains the highest concentration of clumps in the sky towards the inner few degrees of the Galaxy, and the 1.1 mm emission is about 5 times brighter than adjacent parts of Galactic plane. The region between $l = 0°$ to $1.5°$ contains 542 Bolocat entries, or 361 objects per square degree. In contrast, the Galactic disk away from the Galactic center between $l = 5.5°$ and $11.5°$ contains 511 entries in 6 square degrees or 85 objects per square degree on average. This field is chosen for comparison since it likely has a similar surface density of foreground BGPS clumps as the Galactic center region. The symmetrically located field in the 4-th quadrant was not observed to comparable depth due to its lower elevation as seen from Mauna Kea. The surface density of clumps is somewhat larger around $l = 20°$ to $35°$ where the line-of-sight passes through the tangent points in the Molecular Ring. Thus, the surface density of clumps in the CMZ is about 4.3 times higher than in the plane. When Bolocat entries located at higher latitudes above and below the CMZ are excluded, the surface density of Bolocat clumps located close to the Galactic center is more than a factor of 5 higher. This is a lower limit since confusion is likely to make Bolocat have lower fidelity in the Galactic center. Thus, at least 80% of Bolocat entries in the inner few degrees of the Galaxy are likely to be within 500 pc of the nucleus, located at approximately 8.5 kpc from the Sun. Less than 20% are likely to be located in the molecular ring at distances of 2 to 6 or 11 to 14 kpc from the Sun.

The concentration of clumps in the CMZ permits the generation of a clump mass spectrum for a large sample of objects located at a common distance between about 8 and 9 kpc. The formulae in section 2.1 are used to estimate individual clump masses from the peak flux per beam in a $40''$ diameter (1.64 pc at D = 8.5 kpc) aperture tabulated in column 13 in Bolocat. Figure 5 shows the mass spectrum using the assumption that all clumps have the same temperature of $T_{dust} = 20$ K. For masses above about 100 $M_\odot$, the mass spectrum can be fit by a power-law, $dN/dM = kM^\alpha$ with an index $\alpha \approx$ –2.14 $\pm$ 0.1. On this scale, the Salpeter Initial Mass Function (IMF) of stars has a slope of –2.35. Between about 400 and 10^4 $M_\odot$, the slope is slightly steeper with $\alpha \approx$ –2.58 $\pm$ 0.1, but there are several very massive clumps such as Sgr B2 which lie well above the extrapolated curve. Figures 6 to 8 show mass-spectra under different assumptions about the dust temperature and its variation with either Galacto-centric distance or the peak 1.1 mm flux in each clump. These spectra are based on the fluxes reported in the V1.0 data release and have not been scaled by the factor

of 1.5.

Great caution must be exercised in generating mass-spectra for diffuse objects and in the comparison of such spectra with those obtained with different telescopes, at different wavelengths, and using different tracers. Mass-spectra will be biased by the properties of the data acquisition strategy, the properties of reduction pipelines, the definitions and algorithms used to define 'objects'. Nevertheless, mass-spectra are frequently presented in the literature on molecular clouds and their condensations. Despite their potential pitfalls, mass-spectra were computed because BGPS contains one of the largest samples of dense clumps ever obtained.

Miyazaki & Tsuboi (2000) present a mass spectrum for molecular clouds in the Galactic center, finding that for masses greater than 10^4 $M_\odot$, the slope of the mass function is $\alpha = -1.59 \pm 0.07$, considerably shallower than the slope of BGPS clumps. Inspection of their $J = 1 - 0$ CS images shows that the emission is continuous, area-filling, and dominated by extended structure in both the $l-b$ and $l-V$ maps; it is far less 'lumpy' than the BGPS maps which are dominated by small-scale strucutre. Thus, it is not surprising that the overlap in mass between the CS and BGPS mass-spectra is small or that the majority of CS features are considerably more massive than the BGPS clumps. The slope of the 1.1 mm BGPS mass spectrum above about 100 $M_\odot$ is similar to the mass spectrum of low-mass cloud cores in the Solar vicinity which has a slope of around –2.3, similar to the stellar initial mass function (Motte et al. 1998, 2001; André et al. 2007; Enoch et al. 2008); it is considerably steeper than found for CO-emitting GMCs in the Galactic plane.

Because at the distance of the Galactic center, most BGPS clumps will form clusters rather than individual (or multiple) stars, it may be more appropriate to compare the BGPS mass spectra with the mass spectra of star clusters. Observations of Galactic star clusters (Battinelli et al. 1994) and OB associations (McKee & Williams 1997) reveal steep mass spectra scaling as M^{-2}. Massive young star clusters in the merging galaxy pair known as the 'Antennae' also have $dN/dM = N_0 M^{-2}$ (Zhang & Fall 1999) in the mass range $10^{3.5}$ to $10^{6.5}$ $M_\odot$. Similar results have been found for clusters in M51 (Bik et al. 2003) and older clusters in the Large Magellanic Cloud (de Grijs & Anders 2006). Nearby low-mass star-forming cores, more distant and more massive BGPS clumps in the Galactic center, and Galactic and extra-galactic star clusters share the common trait of having steep mass spectra. That all three classes of object are gravitationally bound may have something to do with this trait.

The BGPS data acquisition and reduction pipeline results in images with highly attenuated response to extended structure, effectively acting as a high-pass filter that attenuates low-spatial frequencies (Aguirre et al. 2010). Furthermore, the Bolocat watershed algorithm

(Rosolowsky et al. 2009) tends to subdivide sources with complex structure into multiple clumps. The Sgr B2 complex provides a good example. While single dish maps in tracers such as CO or other high-dipole moment molecules such as CS show that this region consists of a single cloud complex about $0.2°$ by $0.3°$ in extent (e.g. Figure 3), the BGPS images such as Figures 9 highlight local maxima and interconnecting ridges. Bolocat subdivides the Sgr B2 complex into several dozen clumps. Attenuation of low spatial frequencies combined with the watershed algorithm of Bolocat may remove objects from the high-mass, large-extent portion of the mass-spectrum and re-distribute the flux into a larger number of lower-mass entries. This has the effect of steepening the power-law index of the derived mass-spectrum. Detailed simulations to quantify this effect are needed and will be the subject of a future paper. In complex fields such as the Galactic plane, line-of-sight blending of physically unrelated sources may lead to further confusion which can alter the slope of the mass function. We urge the reader to exercise great caution in the interpretation of mass spectra of diffuse objects.

Bolocat (Rosolowsky et al. 2009) tabulates fluxes in four different ways. In addition to the flux in a $40''$ aperture, fluxes are also measured in $80''$ and $120''$ apertures. The catalog also tabulates the total flux in the area assigned to each clump along with a beam-deconvolved "effective" radius of the clump (the radius of a circle that has the same area as the clump). Mass-spectra based on fluxes measured in larger apertures have shallower slopes by about 0.1 to 0.2.

The mass-spectrum derived from the Bolocat fluxes measured in a $120''$ diameter aperture using a constant dust temperature of 20 K has a power-law index $\alpha = -2.04$ (Figure 6), slightly shallower than the index based on measurements in a $40''$ aperture. This difference may be due to increased source confusion within the larger aperture. The relatively small slope change may suggest that source blending and confusion already affects the slope based on fluxes in the smaller aperture. The slope also depends slightly on the widths of the bins used to generate the histograms.

A curious puzzle about the Galactic center is that the dust temperature appears to be lower than the gas temperature despite the high average density. Both the COBE and ISO satellites determined that the average dust temperature in the CMZ ranges from 15 to 22 K (Reach et al. 1995; Lis et al. 2001). Thus, the use of $T_{dust} = 20$ K in mass estimation is justified. However, the dense gas associated with this dust is considerably warmer with 80% of the ammonia having temperatures between 20 and 80 K and 18% warmer than 80 K (Nagayama et al. 2007).

Is the slope of the derived mass spectrum sensitive to variations in T_{dust}? Two types of dust temperature variations are considered to answer this question: First, the dust temper-

ature of a clump is assumed to decrease with increasing projected distance from Sgr A as a power law. Second, the dust temperature of each clump is assigned a value depending on the observed flux; a 100 Jy source such as Sgr B2 is assumed to have dust with T = 50 K while a 1 Jy source is assumed to have T = 20 K. This corresponds to a dust temperature varying with flux, F, as $F^{0.2}$.

Given a source of luminosity L located at a distance r from a grain, the mean grain temperature depends on the luminosity L and distance r as

$$T(r) = T_0 L^{1/\gamma_g} r^{-2/\gamma_g}$$

(Scoville & Kwan 1976) where T_0 is a normalization constant. For blackbodies larger than the emitted and absorbed wavelengths, $\gamma_g = 4$. For interstellar grains, γ_g ranges between 5 and 6 for grain emissivity power-law indices ranging from 1 to 2. Assume that the heating luminosity L is generated by stars in Galactic disk and bulge, that the luminosity-to-mass ratio is constant, and grains at a given distance r from the Galactic center are heated mostly by the stars within a sphere of radius r centered on the Galactic center. Thus, the enclosed luminosity, $L(r)$, is a function of r which can be estimated by assuming that the density of stars decreases with increasing distance from the Galactic center as $\rho(r') = \rho_0 r'^{-\delta}$. For $\delta = 2$ (the singular isothermal sphere), integrating the mass distribution from $r' = 0$ to r implies that the mass enclosed within a radius r is proportional to r. Thus, the luminosity $L(r)$ is also proportional to r. Inserting this in the above equation for $T(r)$ gives a simple approximation for the radial variation of the grain temperature

$$T(r) = T_0 r^{-1/\gamma_g}$$

where T_0 is normalized to a temperature at some radius. This estimate applies to grains which are located mostly at cloud surfaces or otherwise are exposed to the visual and near-IR component of starlight. As a concrete example, choose $\beta = 1$ and $\gamma_g = 5$ so that $T(d) = T_0 r^{-0.2}$ because it yields reasonable cloud surface temperatures over a wide range of Galactocentric distances. Taking $T_0 = 50$ K at $r = 10$ pc implies $T = 27.5$ K at $r = 200$ pc, 15.5 K at $r = 3$ kpc, and 12.5 K at 8.5 kpc. This parametrization provides reasonable base temperatures at the surfaces of clouds lacking internal or close-by heating sources. It is used to test the sensitivity of the mass spectrum to a systematic decrease of grain temperature with increasing galacto-centric distance.

Systematic temperature variations do not have a large impact on the derived slope of the mass spectrum. However, the elevated temperature does decrease the estimates of total mass. The mass-spectrum for $\gamma_g = 5$ corresponding to a radial temperature gradient expected for a grain emissivity that decreases with wavelength as a power-law with index $\beta = 1$ has a slope of $\alpha = -2.44$ (Figure 7).

Finally, it is possible that internal heating by massive stars results in an average dust temperature that is a function of 1.1 mm flux. To determine the consequences of such a model on the derived mass-spectrum, we assume that the dust temperature varies as $T = T_0 F_{1.1}^{0.2}$ where the normalization constant T_0 is chosen to give a dust temperature of 20 K for a 1.1 mm flux density per beam of 1 Jy. This model results in a steeper mass spectrum shown in Figure 8 with a slope of α = -2.64.

These results show that the mass spectrum of mm clumps having masses above about 70 $M_\odot$ is represented by a steep power-law comparable to low-mass star forming cores with masses below about 10 $M_\odot$ (Motte et al. 1998, 2001; André et al. 2007). The derived power-law index is relatively insensitive to assumptions about the dust temperature. In summary, the power-law index of Bolocat clumps in the Galactic center is 2.14 (+0.4,–0.1). The mass-spectrum in the Galactic center is steeper than GMC mass-spectra in the inner galaxy and LMC and comparable to the outer Galaxy and M33 (Rosolowsky 2005). However, great caution must be exercised in the interpretation of these mass spectra owing to the data acquisition and reduction methodology.

The total H_2 mass of the 1428 Bolocat clumps between $l = -1.5°$ to $4.5°$, measured in a $40''$ aperture, assuming that all are located at a distance of 8.5 kpc, have a dust temperature of 20 K, and multiplied by the empirically determined scaling factor of 1.5 needed to bring BGPS fluxes into agreement with MAMBO (Motte et al. 2003, 2007) and SIMBA (Matthews et al. 2009) gives $M(H_2) \sim 6.6 \pm 1 \times 10^5$ $M_\odot$. Assuming a temperature gradient that decreases with distance from Sgr A as proposed above gives the lowest total mass of order $\sim 5.7 \pm 1.2 \times 10^5$ $M_\odot$. Assuming a dust temperature that scales with detected 1.1 mm flux as described above gives a total mass of $\sim 1.1 \pm 0.23 \times 10^6$ $M_\odot$ in a $40''$ aperture. In the $120''$ aperture, (assuming a constant dust temperature of 20 K) this mass grows to $\sim 5.5 \pm 1.2 \times 10^6$ $M_\odot$. Using the total integrated flux (Bolocat column 19) within the effective radius (Bolocat column 12) results in a total mass $\sim 6.2 \pm 1.8 \times 10^6$ $M_\odot$.

Summing all BGPS flux in this field above 100 mJy gives a mass of about $\sim 6.3 \pm 1.8 \times 10^6$ $M_\odot$. The total mass of molecular gas within 500 pc of the center has been estimated to be between 3 to 8×10^7 $M_\odot$ (Sodroski et al. 1994; Dahmen et al. 1998; Tsuboi et al. 1999). Thus, the total 1.1 mm emission from clumps in a $40''$ aperture represents about 0.7% to 2.2% of the total mass in molecular gas while the mass in a $120''$ aperture is about 7% to 18% of the total. Summing the flux above 100 mJy correponds to 8% to 21% of the total molecular gas mass. This is about a factor of several larger than what was found in the Gem OB1 association toward the Galactic anticenter (Dunham et al. 2009), indicating that a larger fraction of the molecular gas near the Galactic center is in compact clumps.

It is important to recall that BGPS filters out extended emission on scales larger than

about 5$'$ and that the 1.1 mm data is only sensitive to dust in compact structure. Such spatial-filtering is not present present in the single-dish spectral line data which therefore can trace gas in extended regions. Thus, the small mass fraction detected by BGPS may be a consequence of the spatial filtering or diffuse, extended emission. Spatial filtering of the spectral line data to match BGPS could be used to constrain the relative abundances of dust and the tracers producing the lines.

3.2. The Central Molecular Zone

Figure 1 shows an image of the 1.1 mm emission from the Galactic center region. Figure 2 shows this image as contours superimposed on the Spitzer Space Telescope IRAC 8μm image. As at most long IR, sub-mm, and radio wavelengths, the area-integrated 1.1 mm emission is about 5 times brighter than in adjacent portions of the inner Galactic plane. While most of the Galactic plane mm-wave continuum emission is dominated by discrete clumps (Aguirre et al. 2010; Rosolowsky et al. 2009; Dunham et al. 2009), the CMZ contains bright arcminute-scale extended structures interconnected by a lacy network of filaments. Figure 9 shows the inner 2 square degrees of the Galactic plane at 1.1 mm. Figure 10 shows the same field at 8.0 μm as observed by the Spitzer Space Telescope (Arendt et al. 2008) with contours of 1.1 mm emission superimposed.

The chain of bright 1.1 mm clumps extending from Sgr B2 (G0.68,–0.03) to G0.26+0.03 and the surrounding lower level diffuse emission is seen in silhouette against the bright background in the infrared image. The 20$'$ halo of 1.1 mm emission surrounding Sgr B2 can also be seen in silhouette against the infrared background. Thus, most of BGPS emission between $l = 1.0°$ and $0.25°$ must originate in front of most of the stars and mid-infrared light in the central bulge of the Galaxy. This is consistent with the suspected orientation of the central bar whose positive longitude part is closer.

Several features of the dust continuum emission from the CMZ are apparent. First, most of the 1.1 mm emission with a flux density greater than about 1 Jy / beam originates from a few dozen clumps (in the Bolocat clump catalog, many of these objects are subdivided further). The two brightest peaks correspond to Sgr B2 and the Sgr A*. At lower levels, the CMZ can be decomposed into hundreds of individual clumps and filaments. Bolocat contains 1428 entries in the field covered in Figure 1. Second, most of the 1.1 mm emission in the CMZ closely follows the distribution of dense molecular gas traced by high-dipole moment molecules and the large line-width CO emission (Bally et al. 1987, 1988; Oka et al. 1998, 2001b). In the inner square degree, both the 1.1 mm dust continuum and the molecular tracers of the CMZ exhibit a smaller scale-height than emission from the Galactic disk

measured beyond $|l| > 1°$. Near Sgr A ($l \approx 0°$), the vertical extent (orthogonal to the Galactic plane) of the brightest BGPS emission and broad-line molecular gas is only about $2'$ to $3'$ (5 to 8 pc); near Sgr B2 around $l \approx 0.7°$ this layer has a thickness of about $10'$ to $15'$ (25 to 40 pc). Beyond $|l| \sim 1°$, the scale-height of 1.1 mm clumps associated with the CMZ increases dramatically. Around $l = 1.3°$ and $3.2°$ the gas layer is nearly $60'$ (150 pc) thick. Away from the Galactic center, between $l = 5°$ and $35°$ the dust layer has an average thickness of about $0.8°$ or 125 pc. The spatially averaged 1.1 mm flux from the Galactic center features is about 3 to 5 times higher than the average flux from the roughly $\pm 0.4°$ scale-height clump population of the Molecular Ring which is at least 3 kpc in front of (or behind) the Galactic center. Third, many 1.1 mm features can be seen in silhouette in the 8 μm IRAC and 24 μm MIPS images. Fourth, at levels up to several hundred mJy/beam, a complex network of filaments forms a frothy background of emission which surrounds voids. The filaments may either trace the walls of stellar-wind bubbles or SNR, the warm edges of molecular clouds, cavities produced by HII regions, or "fossil" cavities whose energy sources are extinct.

Comparison with the 20 cm radio maps (Figure 11) shows that only a small subset of these 1.1 mm cavities are associated with radio continuum emission. Figure 11 shows the 20 cm emission imaged with $30''$ resolution (Yusef-Zadeh et al. 2004) superimposed on the 1.1 mm image. The Sgr A, B1, B2, C, and D regions that contain young massive stars and star clusters stand out in both the radio continuum and at 1.1 mm. The non-thermal radio continuum filaments tend to be located adjacent to 1.1 mm clumps. For example, the largest and brightest group of filaments near $l = 0.18°$ crosses the Galactic plane at the positive latitude end of the ridge of clumps associated with the 50 km s^{-1} cloud that stretches from $l = 0°$ to $0.17°$. The fainter non-thermal filament located directly above (in latitude) Sgr A known as N5 (Yusef-Zadeh et al. 2004) passes through the cluster of clumps associated with the HII region G359.96,+0.17. The brightest part of filament N8 abuts a diffuse 200 mJy BGPS clump at [359.78,0.17] (not marked).

Some of the diffuse 1.1 mm emission between $l = 0.24°$ and $-359.6°$ located at positive latitudes is visible in emission at 8 μm. At positive longitudes, this region contains the thermal "arched filaments" near the Arches cluster. The 1.1 mm emission may either trace warm dust or free-free emission from dense, photo-ionized plasma illuminated by the Arches Cluster. At negative longitudes, 1.1 mm clumps associated with the high-latitude, positive velocity portion of the "expanding molecular ring" ($b = 0.0°$ to about $0.2°$; $V_{LSR} = 100$ to 200 km s^{-1}) are also associated with 8 μm emission. At negative longitudes, the 20 km s^{-1} cloud located south of Sgr A* is visible in silhouette and must therefore be in front of the central cluster. A pair of oppositely facing comet-shaped clouds near the right edge of Figures 9 through 11 (associated with Sgr C and G359.62–0.24) are both seen prominently

in extinction. Except for these clouds, few of the 1.1 mm sources at negative longitudes are visible in extinction in the IRAC data.

The fainter 1.1 mm continuum is structured and organized into a filamentary network of arcs and circular features. This is most evident in left half of Figure 9. Some rings and partial rings surround radio continuum features and therefore probably mark dust heated in PDRs and the edges of cavities created by massive stars and star clusters. However, most rings, arcs, and filaments are not associated with known HII regions or supernova remnants. Massive stars that have shed their natal cocoons are hard to separate from the multitude of intrinsically fainter foreground stars, because in the IR distant massive stars and closer lower-mass stars have similar colors and spectral shapes. These cavities may also be the remnants of older generations of stars and clusters whose most massive members have either exploded as supernovae more than a million years ago so that all radio continuum has long since faded, or whose stars were ejected by dynamical processes that create run-away, high-velocity stars. Run-away stars are most common among spectral type O (Gies & Bolton 1986; Gies 1987); many of these stars were ejected by dynamic interactions in dense clusters (Gualandris et al. 2004). The shells and filaments may be tracers of fossil star and cluster formation in the CMZ. However, it is also possible that randomly superimposed filaments create the impression of cavities.

The large kidney-bean-shaped clump at [0.26,0.03] (see Figures 9 and 12) is remarkable for being one of the brightest features at 1.1 mm and for being the most prominent infrared dark cloud (IRDC) in the entire Galactic center region (Liszt 2009). This feature is seen in absorption at 24 μ (Figure 14). Although Bolocat lists two entries for this object (Nos. 96 and 99), dense gas tracers such as CO, CS, and HCN indicate that the entire structure is at approximately the same radial velocity ($V_{LSR} \approx 40$ km s^{-1} with a line-width extending from 20 to 60 km s^{-1}). Liszt (2009) use the MSX data to set a lower bound on the column density of $N(H_2) > 1.0 \times 10^{23}$ cm^{-2} ($A_V > 53$ magnitudes), consistent with the 1.1 mm-based column density estimate in a 40$''$ aperture. The higher resolution 350 μm observations (Figure 12) indicate that it has considerable sub-structure with consequently larger column densities.

Figure 13 shows the ratio map formed from the 350 μm and 1.1 mm data in the vicinity of Sgr A. In regions with significant emission at both wavelengths, there is a general trend that the clump centers where the fluxes peak have the smallest flux ratios. The flux ratios tend to increase towards the clump edges. Ratios at a number of locations in Figure 13 are indicated by the blue arrows. In Figure 13, the flux in the 1.1 mm BGPS maps have been scaled-up by a factor of 1.5. Without this scaling, a large fraction of the pixels have ratios larger than 100. Figure 13 shows that clumps in the CMZ have warmer dust than either

foreground or background clumps in the Molecular Ring.

Sgr B2 is the brightest clump in the entire BGPS survey. Figure 15 shows the 350 μm image. As shown in Table 2, it has the largest total mass ($> 5 \times 10^5$ M$_\odot$), highest volume-averaged density ($n(H_2) > 10^4$ cm^{-3}), and greatest column density ($N(H_2) > 2 \times 10^{24}$ cm^{-2} in 33″ beams centered on Sgr B2 Main and North) of any BGPS clump. Thus, the average extinction towards Sgr B2 M and N corresponds to at least 1,000 magnitudes at visual wavelengths. Molecular line measurements indicate that the Sgr B2 complex has a mass of at least 5×10^6 M$_\odot$, at least a factor of 10 greater than implied by the total 1.1 mm flux detected by BGPS and listed in Table 2 (Jones et al. 2008). Over 50 compact HII regions and powerful masers indicate that a major burst of star formation is occurring here (Gaume et al. 1995; de Pree et al. 1998; De Pree et al. 2005). The molecular line data provide evidence that the intense burst of star formation occurring in Sgr B2 may have been caused by the supersonic collisions between two giant Galactic center molecular clouds (Jones et al. 2008; Liszt 2009). Sgr B2 may be located near the high-longitude end of 'x2' family of orbits in a bared potential (Contopoulos & Papayannopoulos 1980) where it may encounter gas moving along the 'x1' family of orbits. Sgr B2 is located at the high-longitude end of a chain of 1.1 mm clouds, mid-IR extinction features, embedded 24 μm sources, and HII regions starting near the less-extincted and older Sgr B1 complex (Yusef-Zadeh et al. 2009). Sgr B2 may represent the most recent event in a chain of sequential star formation that started near Sgr B1. The Sgr B2 complex may be giving birth to a massive star cluster or even a super star cluster comparable to the somewhat older Arches and Quintuplet clusters located in the CMZ.

Figures 17 and 18 show the BGPS 1.1 mm contours superimposed on the Spitzer 8 and 24 μm images respectively. These images clearly show that most of the dust associated with the Sgr B2 region is in front of the bulk of the 8 and 24 μm emission. Furthermore, several of the roughly circular cavities in the BGPS images are translucent in the IR data. The large Sgr B1 complex of HII regions and infrared sources has created a giant cavity on the low-longitude and low-latitude side of Sgr B2. Highly obscured nebulosity and IR sources abut the the Sgr B2 sub-mm/mm peaks on the low-latitude side. However, no IR sources can be seen at the locations of Sgr B2N and Sgr B2M. More discussion of the Sgr B2 region is given in the Appendix.

Figure 16 shows the 350 μm / 1.1 mm flux ratio map derived from the 350 μm image matched in spatial frequency response to BGPS divided by a 1.1 mm map scaled-up by a factor of 1.5. No correction for line contamination has been applied. Sgr B2 is likely to be most affected by such contamination; Lis & Goldsmith (1991) found about 30% of the 350 GHz flux is due to lines and contamination. The two brightest peaks, corresponding to Sgr

B2 North and Sgr B2 Middle (or Main) have the smallest flux ratios (25 and 34, respectively) which for $\beta = 2$ dust, implies temperatures of $14 - 17$ K. It is likely that the dust is internally heated by forming massive stars to at least 20 K, and possibly 40 K (Lis et al. 1991). As these authors proposed, it is possible that the low flux ratio is the result of an unusually low β; for $\beta = 1.5$, ratios of 25 and 34 imply 21 K and 33 K.

3.3. Sgr A* and its Environment

The second most prominent peak in the 1.1 mm data (Sgr B2 is the first) is centered on Sgr A* which is thought to mark the location of the $4.5 \pm 0.4 \times 10^6$ M$_\odot$ black hole at the Galactic center (Genzel et al. 2003; Ghez et al. 2008). The extended radio source known as Sgr A consists of Sgr A East, a several arc-minute diameter oval of non-thermal radio continuum emission thought to trace a supernova remnant, and Sgr A West, an HII region which consists of a "mini-spiral" of dense, thermal plasma with the central black hole, Sgr A* at its center. The "mini-spiral" is surrounded by the ~ 2 pc radius "circum-nuclear-ring" (also referred to as the "circum-nuclear disk" – CND) of dense molecular gas and dust (Morris & Serabyn 1996). The CND is clearly seen in the 350 μm image shown in Figure 12.

Emission from Sgr A* peaks near a wavelength of 1 mm (Serabyn et al. 1997). Between 1993 and 1996 the peak flux near this wavelength was around 3.5 Jy (Figure 2 in Serabyn et al. (1997)). In July 2005, Sgr A* was about 1.6 times brighter at 1.1 mm with a flux density of 5.7 Jy. This may be an underestimate because the BGPS pipeline may not fully recover the flux of bright sources or those surrounded by an extended envelope (Aguirre et al. 2010; Rosolowsky et al. 2009). Diffuse emission produced by dust or hot plasma along the line of sight contributes at most 1 Jy per beam. Thus, the increased brightness of Sgr A* in the 1.1 mm maps is most likely due to variability which is consistent with a non-thermal origin for most of the 1.1 mm continuum emission from that source.

Figure 12 shows the 350 μm SHARC-II image of the $30'$ field surrounding Sgr A. Figure 14 shows contours of 350 μm emission superimposed on the Spitzer 24 μm image. In contrast to 1.1 mm, there is very little 350 μm emission from Sgr A* itself. At 350 μm, Sgr A* has a flux density between 0.5 and 1.5 Jy depending on how the large background flux is subtracted. While emission from the CND and Sgr A* are blended at 1.1 mm by the $33''$ effective resolution, in the 350 μm image, the CND is resolved (Figure 12) and appears as a nearly complete oval. Several dozen discrete clumps and filaments can be identified in the region surrounding the ring in addition to the prominent 20 and 50 km s^{-1} clouds. Interferometric observations of molecules such as HCN resolve the CND into a collection of dense clumps (Christopher et al. 2005). The detection of maser emission and hyper-compact

sources of radio continuum emission indicates on-going massive star formation in the CND (Yusef-Zadeh et al. 2008).

The central 30′ region contains several chains of 1.1 mm clumps and filaments elongated towards Sgr A (turquoise lines in Figures 9 through 11 red lines in Figures 12 and 14). These chains are narrower at the end facing Sgr A and may therefore be cometary clouds sculpted by this source. The two most prominent chains are located about 1′ south of the Arches cluster and 2′ south of the Quintuplet cluster and Pistol Star; these chains are each about 6′ to 8′ long. A shorter, fainter chain is located between the Arches and Quintuplet clusters, and a nearly 10′ long chain is located about 3′ north of the Arches cluster. These features are also seen in the 350 μm image (Figures 12 and 14) where they break-up into complicated substructures with an overall elongation towards or away from Sgr A.

About a half dozen compact clumps located between the IRDC at [0.26,0.03] and the Quintuplet cluster near $l \sim 0.22°$ are also elongated along the Galactic plane and may be smaller cometary clouds less than 1′ to 2′ in length. These are best seen in Figure 9. Figure 11, shows that these clumps are located at the high-longitude side of the prominent non-thermal filaments that cross the Galactic plane at $l \approx 0.18°$.

Mid-infrared images from the MSX and ISO satellites reveal a very bright, limb-brightenned bubble of infrared emission surrounding the Quintuplet and Arches clusters (Moneti et al. 2001). Inspection of the 24 μm images obtained by the Spitzer Space Telescope (program P20414; PI - F. Yusef-Zadeh) also shows the prominent elliptical bubble with a major axis bounded towards positive latitudes by the Arched Filaments around $[l, b] \approx [+0.11°,+0.10°]$ and toward negative latitudes by a rim at $[l, b] \approx [+0.12°,-0.18°]$ and extending from $l \approx 0.0$ to 0.18. The oval infrared shell is clearly seen in Figure 14. The location of the 24 μm ovoid is indicated by the large ellipse in Figures 9 through 14.

The chains facing Sgr A are in the projected interior of the infrared "bubble" surrounding the Arches and Quintuplet clusters. It is likely that this bubble traces the walls of a cavity that extends from the non-thermal filaments near $l \approx 0.18°$ to at least $l \approx .0.0°$ near the 50 km s^{-1} cloud and contains both the Arches and Quintuplet clusters and possibly the Sgr A complex. Figure 11 shows that this region is filled with diffuse 20 cm continuum emission. Figure 12 shows this region at 350 μm.

The dashed line in Figure 2 outlines the boundary of a large region relatively devoid of clouds as traced by 8 or 24 μm emission. This feature may trace an extension of the bubble associated with the Arches and Quintuplet clusters that opens-up above and below the Galactic plane. While this feature can be traced to the edge of the observed field above Sgr A, below the Galactic plane it becomes confused with the foreground bubble centered

on $[l, b] = [+0.41°, -0.50°]$. An extended bubble blowing-out of the Galactic plane may have been created by energy release from Sgr A, Arches, and the Quintuplet regions.

3.4. The Inner Galactic Plane: Bania's Clump 2

The Galactic center contains several remarkable cloud complexes which exhibit line-widths $\Delta V > 100$ km s^{-1} over a region typically about $0.5°$ in diameter (Bania et al. 1986; Stark & Bania 1986; Oka et al. 1998; Liszt 2006, 2008). Although Bania's Clump 1 at $[l, b] \approx [-355°, +0.4°]$ and Clump 2 $[l, b] \approx [+3.2°, +0.2°]$ were the first to be noted, similar but less distinct, large line-width complexes exist near $[+1.3°, +0.2°]$ and near $[+5.0°, +0.2°]$ (Oka et al. 1998, 2001a; Dame et al. 2001; Bally et al. 1987, 1988). Bania's Clump 2, located at a projected distance of about 450 pc from the Galactic center, is the most prominent of these features with a line width of $\Delta V \approx 200$ km s^{-1}. The feature extends from the mid-plane to about $b = +0.8°$ and consists of about 16 CS-emitting clumps each with masses of order 5×10^5 M$_\odot$ and H$_2$ densities in excess of 2×10^4 cm^{-3} (Stark & Bania 1986) surrounded by an envelope of CO emitting material. Such dense and massive clumps are usually associated with on-going massive star formation.

Figure 19 shows the BGPS 1.1 mm map of the region around $l = 3°$. Some BGPS data were obtained up to $b = \pm 1.5°$ that shows several additional features associated with Bania's Clump 2. These data are noisier than the BGPS data along the plane and are not shown here. The 1.1 mm clumps coincide with the CS and CO clouds in Bania's Clump 2. Figure 20 shows the Spitzer Space Telescope 8 μm image from GLIMPSE (Benjamin et al. 2005) with superimposed 1.1 mm contours. The most striking result is the absence of extended infrared sources or bubbles associated with most Clump 2 features. In contrast to Clump 2, 1.1 mm clumps located along the Galactic plane tend to contain infrared sources at 4.5, and 5.8 μm, extended 8 μm emission, and prominent bubbles, indicating massive star and star cluster formation. Inspection of the 24 μm MIPS scan-maps available from the Spitzer Science Center archives also shows a general absence of mid-IR sources in Bania's Clump 2. This result is consistent with the lack of 20 cm radio continuum emission (Yusef-Zadeh et al. 2004).

Comparison of the 1.1 mm and Spitzer images shows that there is a slight depression in the spatially-averaged 8 and 24 μm emission from the bulge of the Galaxy at the location of the 1.1 mm features in Clump 2. The Clump 2 dust features are weak infrared dark clouds (IRDCs) indicating that most of the dust in this region must be somewhat in the foreground of the bulge. This is consistent with the suspected location of the Clump 2 material in the near-side of the central bar.

Two clumps located in Bania's Clumps to appear to be foreground objects. The 1.1 mm clump located at $[l, b] = [-3.405, +0.877]$ is associated with IRAS 17470-2533 at the high-latitude end of Clump 2. Located several arcminutes southwest of the clump, there is an arc-minute diameter bubble of 8 μm emission which contains a small cluster. The BGPS clump is seen as an IRDC projected in front of the background star field and diffuse emission. Its high latitude and appearance as an IRDC is consistent with this clump and adjacent HII region being located in the foreground in the Galactic disk. The bright BGPS clump at $[l, b]$ $= [+3.34, +0.44]$ is associated with IRAS 17484-2550 and the clump CO003.34+00.44 in the Galactic center survey of Oka et al. (1998, 2001b). The radial velocity ranges from 0 to 40 km s^{-1}. A low-contrast IRDC is associated with this feature.

3.5. Foreground Features and the Galactic Disk

Several prominent 1.1 mm clumps are located at relatively high Galactic latitudes $|b| >$ 0.25°. Some of these clumps are associated with prominent HII regions or bubbles visible in the IRAC images. The Spitzer 8.0 μm images (Figure 10) reveal a prominent bubble centered on the 1.1 mm clump located at $[l, b] = [0.41°, -.50°]$ (Figure 9). In the 8.0 μm Spitzer image, the bubble appears as a nearly circular ring of emission with a radius of about $7'$ ($\sim$ 17 pc) with a dark region centered on the 1.1 mm clump. The 1.1 mm clump is located at the apex of a cometary cloud seen at 8 μm that projects from more negative latitude toward the center of the bubble (Figures 9 and 10). The bubble is rimmed by several 1.1 mm clumps, the brightest of which is located at $[l, b] = [0.28°, -0.48°]$. Several additional 1.1 mm clumps are located at larger projected radii from the center of the bubble along its rim. Figure 11 shows that the bubble interior is lit-up with faint 20 cm radio continuum emission. This region is reminiscent of the IC 1396 bubble in Cepheus with its intruding tongue of molecular gas.

Several other relatively low-latitude 1.1 mm clumps such as $[l, b] = [359.71, -0.37]$, $[l, b] = [359.91, -0.31]$, and $[l, b] = [359.97, -0.46]$ form a chain below the bulk of dust associated with the Galactic center. This chain of clouds and those associated with the Spitzer ring have been recently noted by Nagayama et al. (2009) who identified them in near-IR extinction maps as well as in CO data. These authors estimate distances using the cumulative numbers of stars and reddening to determine distances and column densities. The distance to this chain of clouds located about 0.2° to 0.4° below the Galactic plane ranges from 3.6 to 4.2 kpc. K-band extinctions range from 0.4 to 1.0 magnitudes. In Table 2, we assume a uniform distance of 3.9 kpc for mass estimation.

Another high-latitude region is associated with the compact cluster of 1.1 mm clumps

listed in Table 1 and in the Figures as $[l, b] = [359.96, +0.17]$. The Spitzer image (Figure 10) shows bright 8.0 μm emission at the high-longitude (northeast) side of the cluster of BGPS clumps. This region may be a foreground HII region complex exhibiting a "champagne flow" towards high Galactic longitudes from a molecular cloud containing several dense clumps.

The clumps at $[l, b] = [0.53, +0.18]$ and $[l, b] = [0.84, +0.18]$ are located well away from the dense-gas layer of the CMZ which suggests that they may be foreground clumps in the Galactic plane far from the Galactic center region. Thus, for these objects, as well as the cluster of clumps near $[l, b] = [359.96, +0.17]$, we assume a distance of 3.9 kpc.

4. Discussion

4.1. A Cavity Extending 30 pc from Sgr A?

Millimeter and sub-mm imaging of the CMZ reveals a network of dust filaments, shells, and dense clumps. The ~ 30 pc diameter infrared bubble between Sgr A and $l \approx 0.2°$ is associated with a 1.1 mm and 350 μm cavity that contains the Quintuplet and Arches clusters and Sgr A. Several chains of clumps in the bubble interior point towards Sgr A. The high combined luminosity of the Arches and Quintuplet clusters and of circum-nuclear cluster surrounding Sgr A* can plausibly produce the cavity. Below, the physical parameters of this feature are estimated.

The central few hundred parsecs of the Galaxy contain at least 4 different types of gas reservoir; cold (T < 10^2 K) and dense molecular clouds (n(H$_2$) > 10^4 cm^{-3}) that comprise the CMZ (Morris & Serabyn 1996; Oka et al. 1998), a warm inter-cloud medium (T $\approx 10^2$ to 10^3 K) traced by species such as H$_3^+$ in absorption (Oka et al. 1998, 2005; Goto et al. 2008) and diffuse ^{12}CO and CI in emission (Martin et al. 2004), a warm ionized component (T $\approx$ 10^4 K) traced by recombination and fine structure lines, radio scattering (Lazio & Cordes 1998), and free-free emission and absorption, and an ultra-hot component (T > 10^6 K) traced by X-rays (Wang et al. 2002).

The volume filling factor of the dense, gravitationally bound cold molecular phase is in the range 0.01 (Cotera et al. 2000) to 0.1(Morris & Serabyn 1996). The remaining volume is either filled with gravitationally unbound (to individual clouds or star clusters) warm neutral atomic and molecular, photo-ionized, or X-ray emitting gas (Martin et al. 2004; Oka et al. 2005; Goto et al. 2008). Abundant 3 to 4 μm H$_3^+$ absorption towards massive stars in the central 0.2° of the Galaxy indicates that warm, but mostly neutral gas unbound to any particular cloud may occupy a large fraction of the volume in the CMZ. However, the large angular-diameters of background extra-galactic radio sources produced by scattering

of their radio continuum emission by a foreground screen of electrons (Lazio & Cordes 1998) observed towards the CMZ indicates the presence of relatively dense HII regions towards most lines-of-sight through the CMZ. Yusef-Zadeh et al. (2007) show that 6.4 keV Fe Kα emission fills the projected area of the cavity delineated by the Spitzer 24 μm bubble and the 1.1 mm cometary clouds (see their Figure 13). However, the strongest 6.4 keV emission appears to be associated with the molecular clouds traced by the 1.1 mm continuum. These authors suggest that the X-ray emission is produced by the interaction of low-energy cosmic rays with dense clouds.

We consider a scenario in which UV radiation and winds emerging from the Arches, Quintuplet, and Sgr A* clusters and the central black hole are responsible for carving out the cavity. The massive Quintuplet and Arches clusters may have contributed to formation of the individual cells in which these clusters are embedded. Towards positive longitudes the outer-boundary of the cavity is near $l \approx 0.20°$ at a projected distance of about 30 pc from Sgr A* (Figure 9). As shown in Figure 12, the high longitude end of the cavity is marked by a chain of small dust clouds located around $l = 0.22°$ (northeast of the Quintuplet cluster marked with a "Q" and below the bright 1.1 mm cloud at [0.26°,+0.03°]). The cell associated with the Quintuplet cluster may extend to $l = 0.28°$, or about 40 pc from Sgr A. Below (to the right of) Sgr A, the intense emission from the 20 and 50 km s^{-1} clouds masks the cavity if it extends this far. The 20 and 50 km s^{-1} clouds are physically close to Sgr A; they may block the penetration of UV irradiation and winds. The Spitzer 24 μm image shows that the low-longitude end of the cavity is near $l = 0°$.

An order-of-magnitude estimate of the parameters of an ionized cavity can be obtained from its size and the 20 cm radio continuum flux, which imply that the average electron density in the cavity can not be much above 100 cm^{-3}. Assuming that the cavity interior is ionized and has a uniform hydrogen density, the Lyman continuum luminosity (in units of the number of ionizing photons emitted per second) required to ionize the cavity is $L(LyC) = 3 \times 10^{50} n_{100}^2 r_{10}^3$ where n_{100} is the average ionized hydrogen density in units of 100 cm^{-3} and r_{10} is the mean radius of the cavity in units of 10 pc. The above parameters imply an ionized mass of about $M_{HII} \approx 1.4 \times 10^4 n_{100} r_{10}^3$ Solar masses around the Arches, Quintuplet, and Sgr A.

The Lyman continuum luminosity of the Sgr A region has been estimated from the flux of free-free radio continuum to be around $L(LyC) \sim few \times 10^{51}$ ionizing photons per second. The entire CMZ has a Lyman continuum luminosity of around $1 - 3 \times 10^{52}$ ionizing photons per second (Morris & Serabyn 1996). This radiation field is produced mostly by young massive stars with a possible contribution from the central black hole in the immediate vicinity of Sgr A. Dust within the cavity and the CMZ may absorb a substantial fraction of

the Lyman continuum radiation. However, even if nearly 90% is absorbed, the UV radiation field is sufficient to maintain the central cavity in an ionized state for a mean density of order $10^2 - 10^3$ cm^{-3}.

The orbital time scale in the center of the Galaxy sets a constraint on the age of the cavity and its cometary clouds. Using a typical orbit velocity $V_o = 120$ km s^{-1}, a test particle in a circular orbit would have an orbital period of $t_o = 2\pi r/V_o \sim 0.5 \, r_{10} V_{120}^{-1}$ Myr where V_{120} is the orbit velocity in units of 120 km s^{-1} and r_{10} is the distance from the Galactic center in units of 10 pc. Portions of clouds at different radii that are gravitationally unbound from each other would be sheared on a time-scale comparable to the orbit time. The presence of recognizable cometary clouds implies that they have been ionized on a time-scale shorter than the orbit time. On the other hand, dense clouds are expected to orbit on largely radial trajectories. Thus, the observed cometary features may be objects that have only recently fallen into the interior of cavity with a speed comparable to the orbit speed. In this case, the elongation of these features away from Sgr A may be a result of the survival of dense gas and dust in the region shielded by the dense head facing Sgr A. Alternatively, this cavity may be only recently ionized by the Arches and Quintuplet clusters. If these clusters have high space velocities, they may have completed several orbits around the nucleus during their lifetimes (Stolte et al. 2008) and the cometary clouds in their vicinity may be a consequence of this motion.

4.2. Fueling Star Formation in Sgr A

The formation mechanism of massive stars within the central parsec of the Galaxy has been a long-standing mystery. Wardle & Yusef-Zadeh (2008) present a model in which a giant molecular cloud passes through the center. Gravitational focusing of trajectories by the central black hole and the central stellar cluster of older stars causes gas to collide and dissipate angular momentum and kinetic energy in the wake. This results in the trapping of some gas in eccentric, circum-nuclear orbits, forming a disk of compressed material. Gravitational instabilities in the disk can result in the formation of massive stars.

It has been long suspected that the two most prominent molecular clouds near Sgr A, the 20 and 50 km s^{-1} clouds, are located within the central 30 pc (Morris & Serabyn 1996; Coil & Ho 1999; Wright et al. 2001; McGary et al. 2001; Christopher et al. 2005; Lee et al. 2008). High-dipole moment molecules such as HCN and CS show that they are among the densest and warmest clouds in the CMZ (Miyazaki & Tsuboi 2000). Together, these two clouds give the CMZ its apparently small (few arcminute) scale-height near Sgr A.

The 50 km s^{-1} cloud is located about 10 pc in projection from the CND towards higher longitudes. Several 350 μm filaments connect the 50 km s^{-1} cloud to the CND (Figure 12); these features correspond to ammonia streamers seen by McGary et al. (2001). Lee et al. (2008) present a 3D model based on near-infrared observations of H$_2$ and argue that the 2 pc radius CND was recently fueled by the passage of the 50 km s^{-1} cloud within a few pc of the nucleus. Assuming that the 50 km s^{-1} cloud is on an x2 orbit, the projected separation of about 10 pc from Sgr A* implies that for a proper motion of 100 km s^{-1}, it passed by the nucleus about 10^5 years ago. The passage of the 50 km s^{-1} cloud may have formed the CND, leading to the current episode of massive star formation activity within its clumps.

The 20 km s^{-1} cloud is the most prominent object at 350 μm in the inner square degree of the Galactic center (Figures 12 and 14); it is located about 7 to 20 pc from the nucleus in projection. It is elongated with a length-to-width ratio of about 5 to 10:1 with a major axis that points about to 2$'$ below the CND (Figure 12). Table 2 shows that for an assumed grain temperature of 20 K, the 20 km s^{-1} cloud is the second most massive and densest cloud in the CMZ (Sgr B2 is the most massive and dense). A bright filament of 350 μm and 1.1 mm dust emission connects the 20 km s^{-1} cloud to the CND; this feature is likely to be the same as the one detected in ammonia by Coil & Ho (1999). This structure provides support for the model in which CND continues to be actively fueled, currently by flow from the 20 km s^{-1} cloud (Coil & Ho 1999).

If the center of the 20 km s^{-1} cloud is currently located about 20 pc from the nucleus, and on a near collision course with the nuclear cluster, it may provide fuel for further star formation in the nucleus in the near future. Assuming that this cloud is on an x2 orbit (Binney et al. 1991; Marshall et al. 2008; Rodriguez-Fernandez & Combes 2008) whose velocity is mostly orthogonal to our line-of-sight, and has speed of about 100 km s^{-1}, it will come closest to the nuclear region in a few hundred thousand years.

The IRS 16 cluster of massive stars surrounding Sgr A* could not have formed from any currently visible cloud. The IRS 16 cluster has an age of at least several Myr; Tamblyn & Rieke (1993) give an age of 7 to 8 Myr. The formation of a previous circum-nuclear ring would have required the passage of a cloud about 5 to 10 Myr ago. Any such cloud would have moved too far from the nucleus to have a clear connection to it and may have been disrupted by a combination of tidal forces, UV radiation and winds.

4.3. Little Star Formation in the Large Velocity Dispersion Complex, Bania's Clump 2

Figure 19 shows the 1.1 mm image of the region containing Bania's Clump 2. Figure 20 shows this image superimposed on the Spitzer Space Telescope IRAC image. These images show that despite the presence of dozens of clumps emitting brightly at 1.1 mm, Clump 2 lacks significant mid-infrared emission from either extended or point sources. It is not forming stars at a rate comparable to similar clumps elsewhere in the Galaxy. In the Galactic plane, HII regions and nebulae excited by young, massive stars are frequently seen at 3.6 to 5.8 μm. The 8 μm Spitzer images trace O, B, and A stars by the presence of bubbles rimmed by bright emission from UV-excited PAH molecules and nano-particles. Few of these signatures of massive stars are observed towards Bania's Clump 2. The longer wavelength Spitzer images (e.g. 24 μm) trace highly embedded young stars and clusters. Inspection of the 24 μm Spitzer images shows that Bania's Clump 2 also lacks a substantial population of embedded sources visible at 24 μm. Perhaps the clumps are embedded in a medium having an unusually high pressure or large non-thermal motions which suppress gravitational instabilities on the mass-scale of stars or even clusters. Many of the Clump 2 features are seen in silhouette against background star light and diffuse emission from the ISM in the 3.6 to 8 μm Spitzer images, indicating that they are in front of much of the central bulge.

The absence of emission in the Spitzer images is not the result of high extinction. Regions having similar amounts of 1.1 mm emission closer to the mid-plane of the Galaxy show a factor of 2 to 4 times more emission between 6 and 24 μm. Furthermore, the brightest 1.1 mm emission maxima towards Bania's Clumps 2 imply localized extinctions of $A_V <10$ magnitudes averaged over a 40$''$ aperture. However, the low-spatial frequency emission resolved-out by BPGS may amount to as much as $A_V = 30$ magnitudes based on the line-of-sight column density of CO. But, this would be insufficient to completely hide all Spitzer mid-IR emission.

The exceptionally large line-widths and velocity extent of this complex may be caused by three processes: First, the abrupt change in the orientation of the orbital velocity where a spur or inner dust lane encounters the ridge of dense gas at the leading edge of the Galactic bar. Second, at the ends of the so-called "x1" orbits in a tri-axial potential where they become self-intersecting (Contopoulos & Papayannopoulos 1980; Binney et al. 1991; Marshall et al. 2008; Rodriguez-Fernandez & Combes 2008). In either mechanism cloud-cloud and cloud-ISM collisions result in high ram-pressures, shocks, and turbulence that can produce large line-widths and non-thermal motions. Third, broad-line features such as Bania's Clump 2 may consist of unrelated clouds along an x1 orbit which has a leg aligned with our line-of-

sight. In this scenario, Bania's Clump 2 traces gas in a dust lane at the leading edge of the bar which is elongated along our line-of-sight.

Figure 21 shows a cartoon of the possible configuration of the central regions of the Milky Way as seen from the north Galactic pole. The x1 orbits are elongated along the major axis of the Galactic bar in a frame of reference rotating with the bar. As a family of orbits with decreasing semi-major axes (corresponding to lower angular momenta about the nucleus) are considered, the ends first become more "pointed", then they become self-intersecting. Clouds whose orbits decay eventually enter the regions of self-intersection where they may encounter other clouds or the lower density ISM on the same trajectory with supersonic velocities. The resulting shock waves and consequent dissipation of orbital energy causes the clouds to rapidly migrate onto the smaller "x2" orbits whose major axes are *orthogonal* to the bar. Most of the observed dense gas in the CMZ is thought to occupy the near-side of the X2 orbits at positive longitudes where they are seen as IRDCs.

Models of gas flows in a tri-axial potential can reproduce the major features observed in the longitude-velocity diagrams of molecular tracers of the inner Galaxy (Bissantz et al. 2003; Rodriguez-Fernandez et al. 2006; Rodriguez-Fernandez & Combes 2008; Rodriguez-Fernandez 2009; Pohl et al. 2008; Liszt 2009). It is suspected that the major axis of the central bar is currently oriented within 15° to 45° of our line-of-sight. The conventional interpretation of the Galactic center molecular line emission places the high-velocity rhombus evident in l-V diagrams in the "180 pc molecular ring" (sometimes called the "Expanding Molecular Ring" or EMR - see Figure 4 in Morris and Serabyn 1996). This feature is tilted with respect to the Galactic plane so that the positive latitude part is seen at positive velocities. In Figure 4, this feature is labeled as the "Leading Edge of the Bar" since in most models, the gas that is transiting from x1 to x2 orbits is found in such a dust lane (see Figure 5 in Morris and Serabyn 1996).

Bania's Clump 2 is located at higher longitudes than the 180-pc molecular ring. Thus, it is either located where the x1 orbits become self-intersecting, or where a spur encounters the dust lane at the leading-edge of the bar, or traces gas in the dust lane which is oriented nearly parallel to our line-of-sight. Rodriguez-Fernandez et al. (2006) shows the likely location of Bania's Clump 2 in a hypothetical face-on view of the Galaxy (see their Figure 2). The superposition along the line-of sight of clouds moving near the apex of the innermost, self-intersecting x1 orbits can exhibit a large range of radial velocities within a very restricted spatial region. This phenomenon is caused by the near co-location of clouds moving towards and away from the Galactic center. Some of these clouds will be colliding, resulting in compression, heating, and turbulence generation. While low-velocity cloud-cloud collisions can trigger star formation, high-velocity collisions are likely to be disruptive; sufficiently fast

collisions dissociate molecules and raise post-shock temperatures.

The presence of 1.1 mm clumps and associated gas seen in high-dipole moment molecules such as CS and HCN suggests that the smallest mass that can become gravitationally unstable is comparable to the observed clump mass of 10^3 to 10^4 M$_\odot$. The low-rate of star formation in these clumps implies that fragmentation is suppressed in this environment, possibly by shear or large-fluxes of energy and momentum from large-scales to small.

If cloud collisions and supersonic internal motions suppress star formation, the dissipation of even a small fraction of this energy must emerge as radiation, resulting in the excitation of fine structure cooling lines such as the 63 μm [OI], 157 μm [CII], and 205 μm [NII], or high-J lines of CO and OH. A substantial portion of the internal energy may also go into heating grains which would emerge as sub-mm continuum radiation. The Herschel Space Observatory may be able detect the resulting fluxes.

While such shocks may promote star formation in other environments such as in Sgr B2, they have failed to do so here. Perhaps the mm sources in Bania's Clump 2 are in an earlier, pre-stellar stage of evolution. Clumps could evolve to denser configurations capable of star formation in a few crossing times. Using a typical Galactic center cloud line-width of $\Delta V = 20$ km s^{-1} for each clump, a clump with a radius of $r = 1'$ (~ 2.5 pc) will evolve on a time-scale $t \sim 2R/\Delta V f \sim 2.5 \times 10^5 f^{-1}$ years where f $(= 0.1$ to $1)$ is the area filling factor of gas in the clump. Thus, it is possible that we are seeing the Clump 2 objects in an early state of evolution and that they will become active star formers in the next few million years.

The Clump 2 complex has a diameter of about 0.5 °(70 pc), implying R$_2 \sim 2.3 \times 10^{20}$ cm (25 pc), and a velocity extent of about $2V_2 = 200$ km s^{-1}. The time-scale on which the entire Clump 2 region should evolve is about $t_2 \sim 2R_2/\Delta V_2 f_2 \sim 3.6 \times 10^5 f^{-1}$ years. Figure 19 implies an area filling factor of about $f_2 \sim 0.1$ for the 1.1 mm clumps, so the evolutionary time-scale for the entire complex is a few Myr, comparable to evolutionary time-scales of individual clumps. Both of these time-scales are short compared to the ~ 15 Myr orbital time-scale at the projected speration between Sgr A* and Clump 2.

5. Conclusions

The first wide-field $\lambda = 1.1$ mm continuum map of the inner six degrees of the Galaxy is presented. This emission traces dozens of bright star forming clumps and an extended, nearly continuous filamentary network. Filaments tend to outline a lattice of voids. Some contain bright, diffuse nebulosity in infrared images that may indicate the presence of HII

regions. A few may contain supernova remnants. However, many cavities do not contain obvious energy sources. They may trace fossil cavities carved in the Galactic center ISM by the action of massive stars that have died in the recent past. The large velocity dispersion of gas in the Galactic center region combined with the shear of differential rotation would tend to erase unsupported cavities on a relatively short time-scale. Thus, the cavities require energy injection within the last few Myrs. The four main results of this study are:

First, the 1.1 mm Bolocam Galactic Plane Survey (BGPS) reveals over a thousand individual clumps within a few degrees of the Galactic center that are associated with the Central Molecular Zone (CMZ). Their small scale height compared to the rest of the Galactic plane and association with the dense molecular gas in the CMZ indicates that over 80% of these clumps are likely to be within the central few hundred parsecs of the Galaxy. The 20 and 50 km s^{-1} clouds near Sgr A, and the Sgr B2 complex, host the brightest 1.1 mm sources in the field of study. Comparison of the 1.1 mm emission with 350 μm maps of the regions around Sgr A and Sgr B2 is used to constrain the dust emissivity, grain temperatures, and optical depths. These measurements indicate peak 1.1 mm optical depths of around 0.1, and grain temperatures around 20 to 70 K for an emissivity power-law index of 2.0. Sgr B2 appears to have an atypically low emissivity index for reasonable dust temperatures, indicating that substantial grain growth has occurred. Both the 350 μm and 1.1 mm emission provide evidence for about a half dozen elongated, cometary dust clouds with dense heads pointing towards the Sgr A complex. Some of these features delineate the walls of a multi-celled cavity having a mean radius of at least 30 pc. The most prominent cometary dust clouds delineate cells located near the massive Arches and Quintuplet clusters. These dust features point towards Sgr A, and indicate that UV radiation from the central cluster of massive stars has sculpted the Galactic center environment within the last 1 Myr. The massive 20 and 50 km s^{-1} clouds appear to be located in the interior of this cavity and may shield the nuclear ISM at low longitudes and latitudes from ionization.

Second, the collection of clouds located between $l = 3°$ and $3.5°$ and $V_{LSR} = 0$ to 200 km s^{-1} known as "Bania's Clump 2" are highly deficient in active star formation given their 1.1 mm dust continuum fluxes. It is possible that the clumps in Clump 2 are in a pre- star forming state. This observation provides evidence for models in which Clump 2 consists of gas and dust that has recently been shocked and rendered highly turbulent. This feature may either trace gas that has recently fallen in from the innermost x1 orbit (elongated along the bar) onto the outermost x2 orbit (elongated orthogonal to the bar), or gas that is entering the shock on the leading edge of the bar from a spur, or a dust lane at the leading-edge of the bar that is elongated along our line-of-sight.

Third, under the assumption of a constant dust temperature in the CMZ, the mass

spectrum of clumps M > 70 M$_\odot$ in the Galactic center is characterized by a steep power-law $dN/dM = kM^{-2.14(-0.4,+0.1)}$. This index is significantly steeper than found from CS observations of the Galactic center and similar to the index found for star forming cores in the Solar vicinity. While such a steep index may be a real feature of the Galactic clump population, it may in part be an observational artifact produced by the attenuation of low spatial-frequency flux, source confusion, and the watershed algorithm used to construct Bolocat which tends to subdivide large objects into clusters of smaller ones.

Fourth, comparison of the 350 and 1100 μm images places new constrains on dust properties. Values of β between 1.5 and 2.0 give the most reasonable dust temperatures with values ranging from 15 K to as high as 80K. However, Sgr B2 is anomalous. The low flux ratios here require lower values of β, providing evidence for substantial grain growth.

6.   Appendix I: Comments on Individual Regions

In this section, individual regions Listed in Table 2 are discussed in order of increasing Galactic longitude. Fluxes and mass estimates for the marked features (based on visual inspection of the images rather than Bolocat) are given in Table 2.

The Great Annihilator (1E1749.7-2942); $[l, b] = 359.116, -0.106$): Long suspected to be a major source of 511 keV emission from decaying positronium, this hard X-ray and γ-ray source was initially suspected to be stellar-mass black hole accreting from a molecular cloud (Bally & Leventhal 1991; Mirabel et al. 1991). However, recent observations indicate that this object may be a low-mass X-ray binary (Main et al. 1999). The molecular cloud located adjacent to 1E1749.7-2942 was recently observed at millimeter wavelengths with the CARMA interferometer by Hodges-Kluck et al. (2009) who provides some mass estimates. The molecular cloud is detected in our 1.1 mm image (Figure 22). Thus, we can compare the dust-based mass estimate with the gas-based estimate. Interestingly, while the clump near 1E1749.7-2942 is clearly seen, the brightest HCN and HCO$^+$ clump in the maps of Hodges-Kluck et al. (2009) is not evident in the 1.1 mm dust continuum. The 1.1 mm flux at the location of their HCO$^+$ and HCN peak 2b is only about 30 mJy, comparable to the noise in our maps.

The masses estimated for the cloud adjacent to the Great Annihilator from the 1.1 mm emission in 40$''$ and 300$''$ apertures are 2.7×10^2 and 7.2×10^3 M$_\odot$ (for fluxes scales-up by a factor of 1.5). The mass in the smaller aperture was measured at the location of the HCO$^+$ peak found by Hodges-Kluck et al. (2009). On the other hand, the mass in the larger aperture was determined in an aperture centered on the 1.1 mm peak at $[l, b] = 359.135, -0.100$. Hodges-Kluck et al. (2009) use the Virial theorem to estimate the mass from the clump-size and line-width for their clump 1 (at the location shown by the small circle immediately next the the Great Annihilator in Figure 22). They find M $= 3.9 \times 10^3$ M$_\odot$, in between the two BGPS estimates in 40$''$ and 300$''$ apertures.

Sgr C ($[l, b] = 359.47, -0.11$): There are relatively few major star forming complexes at negative Galactic longitudes. The exception is the Sgr C complex of HII regions. The BGPS images reveal a prominent comet shaped cloud clump complex facing west in the Sgr C region.

$[l, b] = 359.47, -0.03$: This feature is a 1.1 mm clump located at the low-longitude end of a chain of clumps that can be trace back to just above Sgr A. This chain is part of the so-called "Expanding Molecular Ring" that may mark gas and dust at the leading edge of the Galactic center bar. In CO spatial-velocity diagrams, this feature is part of the positive latitude, positive velocity feature that defines the "rhombus" thought to mark the innermost

x1 orbit (marked in Figure 4). A 20 cm non-thermal filament crosses the Galactic plane on the low-longitude side of the marked clump in Figure 11.

$[l, b] = 359.62, -0.24$: Located 15′ east of Sgr C, there is a second, east-facing cometary cloud in the 1.1 mm continuum image. The dense head of this cometary feature abuts the HII region G359.62-0.25 which consists of a series of 20 cm filaments east of the 1.1 mm clump. Extended emission east of the clump is evident in the GLIMPSE 8 μm image (Figure 10). The 1.1 mm clump is the brightest portion of a roughly east-west ridge that extends west towards Sgr C. Both the Sgr C and G359.62-0.24 cometary clouds are clearly seen in silhouette against background 8 μm emission.

$[l, b] = 359.71, -0.37$: A compact 1.1 mm knot associated with a cometary feature in the GLIMPSE images. This is one of the clumps associated with the band of foreground clouds located at about 3.9 kpc from the Sun (Nagayama et al. 2009).

$[l, b] = 359.91, -0.31$: This is another of the clumps associated with the band of foreground clouds located at about 3.9 kpc from the Sun (Nagayama et al. 2009). It is a cometary cloud facing the Galactic plane that is visible in silhouette against the 8 μm background in the Spitzer GLIMPSE images.

The 20 km s^{-1} cloud. ($[l, b] = 359.88, -0.08$): The central twenty parsecs of the Galaxy contains the Sgr A radio complex and the 20 and 50 km s^{-1} clouds; both clouds are seen in silhouette in the Spitzer 8 images (Figure 10). The 50 km s^{-1} cloud located east-northeast of Sgr A* contains bright MSX point sources while the 20 km s^{-1} cloud lacks bright MSX counterparts. Thus, the former is more evolved and is actively forming stars while the latter is more similar to IRDCs and likely to be either in a pre-star forming stage of evolution, or its star formation may be inhibited by its proximity to the Galactic nucleus.

The 20 km s^{-1} cloud is the third brightest source of 1.1 mm emission in the Central Molecular Zone (next only to Sgr B2 and and Sgr A*) and has a mass of at least 1.6×10^5 M$_\odot$. The cloud is elongated along a direction pointing towards Sgr A*. The 350 μm image (Figure 12) shows complex structure consisting of several bright arcs of dust protruding above and below the cloud. Although there is abundant extended 20 cm continuum emission in the general vicinity, no radio features can be directly associated with the cavities outlined by these arcs. Filaments and clumps of dust connect this cloud to the Circum-Nuclear Disk (CND) surrounding Sgr A* and to the 50 km s^{-1} cloud discussed below. As discussed in Section 4.2 this cloud may be plunging towards the central parsecs of the Galaxy on an x2 orbit. If it is on a radial trajectory towards Sgr A*, it is the most likely cloud to inject new gas into the central few parsecs of the Galaxy.

The G359.94,+0.17 Complex: Located 0.2° directly above (in Galactic latitude) the

Galactic nucleus, this complex is associated with several compact 8 μm bubbles. It contains IRAS 17417-2851, a compact cluster of at least four prominent 1.1 mm clumps adjacent to an HII region complex that wraps around the clumps with PDRs and ionization fronts on the north, east and south sides. The non-thermal filament, N5 in Figure 11 (Yusef-Zadeh et al. 2004) is located along the line-of-sight to this clump. However, because of its high-latitude location and visibility in the Spitzer IRAC data as both an IRDC and as a bright region of emission at 8 μm, we assume that it is a foreground complex at an approximate distance of about 3.9 kpc (Table 2).

The 50 km s^{-1} cloud. ($[l,b]$ = 359.98,–0.08): Located only a few arc-minutes east of Sgr A*, the passage of this cloud near the Galactic center may have fueled the injection of gas into the circum-nuclear ring about 1 to 2×10^5 years ago. The cloud contains several compact radio sources (Goss et al. 1985; Yusef-Zadeh et al. 2004, 2008) and evidence for star formation. Tendrils of dust continuum emission appear to link this cloud to both the CND and to the 20 km s^{-1} cloud discussed above.

$[l,b]$ = 359.97,–0.46: An isolated cometary cloud associated with an 8 μm bubble, presumably an HII region. This clump appears to be part of band of foreground clouds located at about 3.9 kpc from the Sun (Nagayama et al. 2009).

$[l,b]$ = 0.05,–0.21: A 1.1 mm clump located directly below Sgr A* and the 50 km s^{-1} cloud with a prominent Spitzer nebulosity on its low-longitude side.

The Quintuplet and Arches Clusters ($[l,b]$ = 0.163,–0.060 and $[l,b]$ = 0.121,+0.018): One of the most striking features of the 20 cm image are series of concentric shells centered at l,b = [0.15,–0.06] near the location of the "Quintuplet" cluster of massive stars (Figer et al. 1999). The innermost ring may trace the ionization front and PDR associated with this cluster; the northeast part of this ring is known as the "Sickle" due to its radio morphology (Lang et al. 2005). The outer, northwest portion of these concentric rings comprise the "Arched" filaments thought to be illuminated by the massive Arches cluster (Figer et al. 2002; Stolte et al. 2005).

While there is no 1.1 mm clump at the location of the Quintuplet cluster, an extensive network of clumps is located adjacent to and to the northeast. The Quintuplet appears to be in a cavity which is consistent with its relatively evolved status. The 4 to 5 Myr old Quintuplet cluster contains one of the most luminous stars yet discovered: the Pistol Star. The VLA 20 cm continuum map shows a prominent ionization front north and east of this cluster that is associated with a ridge of 1.1 mm dust continuum emission along the Galactic plane.

The Arches Cluster is another of the most massive young star clusters in the Galaxy

(Figer et al. 2002; Stolte et al. 2005) and is associated with a diffuse 1.1 mm source. The thermal radio continuum filaments known as the 'Arches' trace ionization fronts and photon-dominated regions (PDRs) illuminated by this cluster. Several clumps of 1.1 mm emission are embedded within the ridges of radio continuum emission. Fainter filaments of 1.1 mm continuum follow the Arches about $10''$ to $30''$ due east of the radio continuum ridges. As shown by Serabyn et al. (1999), the radio emission traces the western edges of a chain of molecular clouds seen in CS. The 1.1 mm emission is located between the radio filaments and the CS clouds, indicating a layer of warm dust on the side of these clouds facing the Arches cluster. This layer is most likely associated with a PDR. (Yusef-Zadeh et al. 2003). Some of the 1.1 mm emission may be free-free emission from the plasma. Wang et al. (2006) proposed that the Arches cluster is colliding with the molecular clouds in this region.

$[l, b] = 0.26, +0.03$: The "lima bean"' shaped molecular cloud extending from $[l, b] = 0.23, +0.01$ to $0.26, +0.03$ is remarkable for being a bright 1.1 mm source not associated with radio continuum sources or any other indicators of on-going star formation such as bright sources in MSX or Spitzer images. In the 2MASS, Spitzer, and MSX images, GCM 0.25+0.01 is seen as the most prominent absorption feature in the CMZ (Figure 10). The cloud qualifies as an infrared-dark-cloud (IRDC) which does not yet contain evidence of star formation. In the SHARC II 350 μm images GCM 0.25+0.01 is resolved into a dozen individual clumps which could be precursors to star-forming clumps. Lis & Menten (1998) find broad molecular line profiles typical of Galactic center Giant Molecular Clouds (GMCs) and a line center velocity of 20 to 40 km s^{-1} similar to the GMCs known to be interacting with the non-thermal filaments that cross the Galactic plane at l = 0.18 near the Pistol and Quintuplet Clusters. GCM 0.25+0.01 may be the best example of a high column density GMC in a pre-star forming state in the inner molecular zone of the Galaxy.

$[l, b] = 0.28, -0.48$: This is the brightest clump in a cluster of clumps associated with the band of foreground clouds located at about 3.9 kpc from the Sun (Nagayama et al. 2009). This clump is located on the rim of the large Spitzer 8 μm bubble centered on the clump at $[l, b] = 0.41, -0.50$. $[l, b] = 0.28, -0.48$ is associated with its own bright Spitzer nebulosity which may indicate the presence of a compact HII region whose birth may have been triggered by the expansion of the Spitzer bubble.

$[l, b] = 0.32, -0.20$: A clump of 1.1 mm emission associated with a bright but compact cluster of extended Spitzer nebulosity. The clump lies at the low-longitude end of fan-shaped group of at least three filaments that converge on this object and which can be traced for at least 0.1° towards higher longitudes in both 1.1 mm emission and 8 μm extinction.

$[l, b] = 0.41, -0.50$: The easternmost 1.1 mm clump associated with the band of foreground clouds located at about 3.9 kpc from the Sun (Nagayama et al. 2009). This particular

clump is located at the high-latitude tip of a large pillar of dust and is centered on the 0.15°
(10 pc) radius ring of 8 μm Spitzer emission.

$[l, b] = 0.41, +0.05$: The low-longitude end of the chain of clouds that extend towards
and includes Sgr B2.

$[l, b] = 0.48, -0.00$: A clump in this chain located directly above the Sgr B1 complex of
HII regions..

Sgr B1 ($[l, b] = 0.506, -0.055$ - not marked on the images): Sgr B1 is a giant HII region
to the southwest of Sgr B2 and associated with extensive recent star formation traced by
radio continuum emission, masers, and IR sources. In the BGPS map, it appears as a large
cavity, marked only by a few faint filaments and bright clumps located to the northwest.
Thus, this region must be more evolved than Sgr B2 because gas and dust has been expelled.

$[l, b] = 0.53, +0.18$: The brightest member of a cluster of 1.1 mm clumps located above
the Galactic plane and Sgr B1. At least three extended 8 μm Spitzer emission nebulae are
associated with this complex.

Sgr B2 ($[l, b] = 0.687, -0.030$): The Sgr B2 complex consists of a 5′ long north-to-south
chain of bright cloud clumps, surrounded by a 'halo' of fainter ones, filaments, and shells
extending over nearly 20′ in R.A. and 10′ in Declination. Sgr B2 clump is the hottest and
currently most active star forming region in a roughly 25 by 50 parsec complex of emission.
Sgr B2 is associated with molecular gas between $V_{LSR} = 30$ to 80 km s^{-1} as seen in tracers
such as CS, HCN, and HCO$^+$ (Bally et al. 1987, 1988; Jackson et al. 1996). Figure 15 shows
the Sgr B2 region at 0.35 mm; Figure 17 shows the BGPS 1.1 mm contours superimposed
on the Spitzer 8 μm image; Figure 18 shows the BGPS 1.1 mm contours superimposed on
the Spitzer 24 μm image.

The brightest emission at 1.1 mm originates from the northern component of the Sgr
B2 complex (Sgr B2N) which has $S_{1.1} \sim 100$ Jy / beam and $S_{0.35} \sim 1,303$ Jy / beam. Sgr
B2M is a bit fainter at 1.1 mm with $S_{1.1} \sim 80$ Jy / beam. However, it is the dominant source
at 350 μm with $S_{0.35} \sim 1,375$ Jy / beam. (Note that the 1.1 mm beam has a diameter of
33″ while the 0.35 mm beam has a diameter of about 9″).

Figures 17 and 18 show that the large cavities located at low longitudes and latitudes
with respect to Sgr B2 are filled with bright IR emission. Furthermore, there is a close
correlation between the mm and sub-mm emission and dark clouds seen in silhouette against
background stars and diffuse infrared light.

Sgr B2 exhibits a rich millimeter-wave spectrum consisting of thousands of individual
spectral lines tracing transitions of over 100 molecular species. Combined with the 10 to

50 km s^{-1} Doppler widths of individual lines, this results in a nearly continuous forest of spectral features. In Sgr B2, the combined flux between 218 to 236 GHz from mostly heavy organic molecules provides a frequency variable background spectrum with peak temperatures ranging from 0.1 to over 10 K (Nummelin et al. 1998) that results in a pass-band averaged flux in this spectral range of about 1 K. Nummelin et al. (1998) argue that about 22% of the total flux from Sgr B2N, and 14% of the flux from the clump known as M is produced by spectral lines. Thus, in the densest clumps, up to tens of percent of the flux in the 1.1 mm BGPS pass-band is produced by spectral lines rather than dust. Away from these few bright regions, the contribution of spectral lines is likely to be smaller than 10% and less than the flux calibration error.

The average 1.1 mm flux of the Sgr B2 complex in a 150″ radius circle centered on Sgr B2N is 10.7 Jy. Assuming a dust temperature of 20 K, the mass enclosed in this region is about 8.3×10^5 M$_\odot$ This region is surrounded by a 0.2° by 0.25° diameter envelope of filamentary emission with an average 1.1 mm flux of about 0.9 Jy that implies an additional mass of at least 1.3×10^6 M$_\odot$. Thus, the total mass of the Sgr B2 complex is at least 1.0×10^6 M$_\odot$. This estimate is a severe lower bound because the spatial frequency transfer function of the BGPS observations and pipeline attenuates emission that is smooth on scales larger than about 3′ and completely filters out emission uniform on scales larger than 7.5′.

The extended Sgr B2 complex is the densest and most massive giant molecular cloud complex in the Galaxy Lis et al. (1991). About a dozen cavities are apparent in the 1.1 mm image. The large 0.15° by 0.08° cavity at located at low Galactic longitudes (centered roughly near $l = 0.50°$, $b = –0.06°$ (Figures 10 and 18) contains bright extended 8 and 24 μm emission in the Spitzer IRAC images that consists of diffuse emission, filaments, and compact sources. This region apparently contains mature HII regions and massive stars formed in a previous episode of star formation. A similar but smaller cavity, centered at $l, b = 0.680°$, –0.600° is also filled with 8 μm emission. These cavities contain an earlier generations of massive stars and mature HII regions.

$[l, b] = 0.84, +0.18$: An isolated clump associated with extended Spitzer emission.

Sgr D ($[l, b] = 1.12, –0.11$): The brightest 1.1 mm clump within a 0.5° region. It is associated with bright Spitzer emission, and two bubbles of 20 cm continuum located north and south of the clump (Figures 9 through 11).

$[l, b] = 1.33, +0.16$: A typical 1.1 mm clump in this portion of the survey. However, this one is associated with a blister HII region that extends to the south of the mm clump.

$[l, b] = 1.60, +0.02$: One of the brightest clumps in the $l = 1.3°$ complex of molecular clouds. The surrounding complex consists of several prominent CO-emitting filaments that

extend vertically out of the Galactic plane for at least 0.5° ($\sim$ 75 pc). This one degree diameter complex has the largest scale-height in the Central Molecular Zone. The radial velocities of CO emitting clouds extend over at least 120 km s^{-1}. This region may be similar in nature to Bania's Clump 2.

IRAS 17481-2738 ([l, b] = 1.74,–1.41): Located at the low-latitude end of the $l = 1.5°$ complex of molecular clouds, this is the second brightest clump in the region.

IRAS 17469-2649 ([l, b] = 2.30,+0.26): A typical example of one of the faint, diffuse clumps in this portion of the Galactic plane. It was singled out because it is associated with bright and extended Spitzer emission as well as a 20 cm radio continuum complex.

[l, b] = 2.62,+0.13: A prominent 1.1 mm clump associated with IRDCs, a complex of Spitzer nebulosities, and a bright, compact cometary 20 cm continuum feature facing east.

[l, b] = 2.89,+0.03: The low-latitude end of a complex of 1.1 mm clumps which contains a compact Spitzer source and filament of bright emission. A small and bright 20 cm radio source may trace a compact HII region. A low-surface brightness and extended bubble of 20 cm continuum emission extends about 0.1° towards low-longitudes. This is one of the few 1.1 mm clumps in the Bania's Clump 2 region that exhibits signs of recent massive star formation. The mm clump is seen as a dim IRDC. It may be located in the foreground portion of the Galactic plane.

IRAS 17496-2624 ([l, b] = 2.96,–0.06): This 1.1 mm clump is associated with the brightest 20 cm radio continuum source in the Bania's Clump 2 region. Spitzer shows a compact limb-brightened bubble opening towards high latitudes. This feature may trace a compact HII region less than 1′ in diameter.

[l, b] = 3.09,+0.16: One of the brightest 1.1 mm clumps in Bania's Clump 2. It is not associated with either a 20 cm or a Spitzer nebula. Located at the high-longitude end of a complex of clumps that may be faintly seen in silhouette at 8 μm.

[l, b] = 3.14,+0.41: A relatively bright 1.1 mm clump in Bania's Clump 2. It is not associated with either a 20 cm or a Spitzer nebula.

[l, b] = 3.31,–0.40: A bright 1.1 mm clump associated with a compact IRDC and with no bright Spitzer sources.

[l, b] = 3.34,+0.42: The largest and brightest 1.1 mm clump in Bania's Clump 2. It does not contain any Spitzer sources. However, it is seen faintly in silhouette at 8 μm and may be associated with very dim, extended 20 cm continuum (0.04 Jy/beam).

[l, b] = 3.35,–0.08: A very bright 1.1 mm and Spitzer source which is associated with a

bright cometary 20 cm continuum source located at the high-longitude end of a large HII region complex.

$[l, b] = 3.44, -0.35$: The brightest 1.1 clump in this part of the survey which is associated with a compact and prominent IRDC. A dim 8 μm stellar object is located near the center of the cloud.

IRAS 17470-2533 ($[l, b] = 3.41, +0.88$): The highest latitude object near Bania's Clump 2, this 1.1 mm clump is surrounded by two tails, one extending towards the Galactic plane, and another towards higher longitudes. The clump contains a bright Spitzer and IRAS source and extended emission . It may be a foreground complex.

IRAS 17504-2519 ($[l, b] = 4.00, +0.34$): An isolated 1.1 mm clump seen as an IRDC that contains a bright and compact 8 μm Spitzer source, likely to be a compact HII region.

$[l, b] = 3.39, +0.08$: A collection of 1.1 mm clumps associated with a complex of Spitzer emission nebulae.

$[l, b] = 4.43, +0.13$: The brightest 1.1 mm clump associated with the above complex. The Spitzer 8 μm emission shows that this clump is a IRDC superimposed on the extended bright emission. The IRDC consists of a compact arc of absorption no more than 8$''$ wide, indicating that the feature is much thinner in one dimension than the Bolocam beam.

7. Appendix II: Bolocat Clump Masses listed in Table 3

The electronic version of this paper contains a table of masses, column densities, and densities computed using the methods outlined in Section 2.1. These masses are based on the Bolocam V1.0 fluxes scaled-up by the empirically determined factor of 1.5. The various entries in Table 3 are described here.

Column 1: The clump number in Bolocat V1.0 released in June via the IPAC website at

http://irsa.ipac.caltech.edu/data/BOLOCAM_GPS/ .

Column 2: Galactic longitude in degrees.

Column 3: Galactic latitude in degrees.

Column 4: J(2000) Right Ascension in degrees.

Column 5: J(2000) Declination in degrees.

Column 6: Mass estimate for each clump measured in a $40''$ aperture assuming T = 20 K as discussed in Section 2.1.

Column 7: H_2 column density estimate for each clump measured in a $40''$ aperture assuming T = 20 K as discussed in Section 2.1.

Column 8: H_2 volume number density estimate for each clump measured in a $40''$ aperture assuming T = 20 K as discussed in Section 2.1.

Column 9: The mass derived from the Bolocat flux in the effective beam-deconvolved area of each clump tabulated in column 19 of the Bolocat catalog available from the IPAC website.

Column 10: The Bolocat effective clump radius tabulated in column 12 of the Bolocat catalog available from the IPAC website.

Column 11: H_2 column density estimate for each clump measured in the beam-deconvolved effective area and based on the mass in column 10 assuming T = 20 K as discussed in Section 2.1.

Column 12: H_2 volume number density estimate for each clump measured in the beam-deconvolved effective area and based on the mass in column 10 assuming T = 20 K as discussed in Section 2.1.

Column 13: Mass estimate for each clump measured in a $120''$ aperture assuming T = 20 K as discussed in Section 2.1.

Column 14: Mass estimate for each clump measured in a $40''$ aperture assuming a tempera-

ture gradient that declines as a power-law with distance from Sgr A*. The power-law has a slope $\gamma_g = 0.2$ and is normalized to have T = 50 K at a distance of 10 pc from Sgr A*. This power-law implies T = 27.5 K at $d = 200$ pc from Sgr A*, 15.5 K at d = 3 kpc, and 12.5 K at $d = 8.5$ kpc. See discussion in Section 3.1.

REFERENCES

Aguirre, J. E. et al. 2010, ApJ, submitted

André, P., Belloche, A., Motte, F., & Peretto, N. 2007, A&A, 472, 519

Arendt, R. G. et al. 2008, ApJ, 682, 384

Bally, J. & Leventhal, M. 1991, Nature, 353, 234

Bally, J., Stark, A. A., Wilson, R. W., & Henkel, C. 1987, ApJS, 65, 13

—. 1988, ApJ, 324, 223

Bally, J. & Zinnecker, H. 2005, AJ, 129, 2281

Bania, T. M., Stark, A. A., & Heiligman, G. M. 1986, ApJ, 307, 350

Battinelli, P., Brandimarti, A., & Capuzzo-Dolcetta, R. 1994, A&AS, 104, 379

Benjamin, R. A. et al. 2005, ApJ, 630, L149

Bik, A., Lamers, H. J. G. L. M., Bastian, N., Panagia, N., & Romaniello, M. 2003, A&A, 397, 473

Binney, J., Gerhard, O. E., Stark, A. A., Bally, J., & Uchida, K. I. 1991, MNRAS, 252, 210

Bissantz, N., Englmaier, P., & Gerhard, O. 2003, MNRAS, 340, 949

Christopher, M. H., Scoville, N. Z., Stolovy, S. R., & Yun, M. S. 2005, ApJ, 622, 346

Coil, A. L. & Ho, P. T. P. 1999, ApJ, 513, 752

Contopoulos, G. & Papayannopoulos, T. 1980, A&A, 92, 33

Cotera, A. S., Simpson, J. P., Erickson, E. F., Colgan, S. W. J., Burton, M. G., & Allen, D. A. 2000, ApJS, 129, 123

Dahmen, G., Huttemeister, S., Wilson, T. L., & Mauersberger, R. 1998, A&A, 331, 959

Dame, T. M., Hartmann, D., & Thaddeus, P. 2001, ApJ, 547, 792

de Grijs, R. & Anders, P. 2006, MNRAS, 366, 295

de Pree, C. G., Goss, W. M., & Gaume, R. A. 1998, ApJ, 500, 847

De Pree, C. G., Wilner, D. J., Deblasio, J., Mercer, A. J., & Davis, L. E. 2005, ApJ, 624, L101

Dowell, C. D. et al. 2003, in Presented at the Society of Photo-Optical Instrumentation Engineers (SPIE) Conference, Vol. 4855, Society of Photo-Optical Instrumentation Engineers (SPIE) Conference Series, ed. T. G. Phillips & J. Zmuidzinas, 73–87

Dunham, M. K. et al. 2009, ApJ, in preparation

Enoch, M. L., Evans, II, N. J., Sargent, A. I., Glenn, J., Rosolowsky, E., & Myers, P. 2008, ApJ, 684, 1240

Enoch, M. L. et al. 2006, ApJ, 638, 293

Ferrière, K., Gillard, W., & Jean, P. 2007, A&A, 467, 611

Figer, D. F., McLean, I. S., & Morris, M. 1999, ApJ, 514, 202

Figer, D. F. et al. 2002, ApJ, 581, 258

Gaume, R. A., Claussen, M. J., de Pree, C. G., Goss, W. M., & Mehringer, D. M. 1995, ApJ, 449, 663

Genzel, R. et al. 2003, ApJ, 594, 812

Ghez, A. M. et al. 2008, ApJ, 689, 1044

Gies, D. R. 1987, ApJS, 64, 545

Gies, D. R. & Bolton, C. T. 1986, ApJS, 61, 419

Glenn, J. et al. 2003, in Proc. SPIE, Vol. 4855, Millimeter and Submillimeter Detectors for Astronomy, 30

Goss, W. M., Schwarz, U. J., van Gorkom, J. H., & Ekers, R. D. 1985, MNRAS, 215, 69P

Goto, M. et al. 2008, ApJ, 688, 306

Gualandris, A., Portegies Zwart, S., & Eggleton, P. P. 2004, MNRAS, 350, 615

Hildebrand, R. H. 1983, QJRAS, 24, 267

Hodges-Kluck, E. J., Pound, M. W., Harris, A. I., Lamb, J. W., & Hodges, M. W. 2009, ArXiv e-prints

Jackson, J. M., Heyer, M. H., Paglione, T. A. D., & Bolatto, A. D. 1996, ApJ, 456, L91+

Jones, P. A. et al. 2008, MNRAS, 386, 117

Kauffmann, J., Bertoldi, F., Bourke, T. L., Evans, II, N. J., & Lee, C. W. 2008, A&A, 487, 993

Kormendy, J. & Cornell, M. E. 2004, in Astrophysics and Space Science Library, Vol. 319, Penetrating Bars Through Masks of Cosmic Dust, ed. D. L. Block, I. Puerari, K. C. Freeman, R. Groess, & E. K. Block, 261–+

Kormendy, J. & Kennicutt, Jr., R. C. 2004, ARA&A, 42, 603

Kovács, A. 2008, in Presented at the Society of Photo-Optical Instrumentation Engineers (SPIE) Conference, Vol. 7020, Society of Photo-Optical Instrumentation Engineers (SPIE) Conference Series

Lang, C. C., Johnson, K. E., Goss, W. M., & Rodríguez, L. F. 2005, AJ, 130, 2185

Laurent, G. T. et al. 2005, ApJ, 623, 742

Lazio, T. J. W. & Cordes, J. M. 1998, ApJ, 505, 715

Lee, S. et al. 2008, ApJ, 674, 247

Lis, D. C. & Carlstrom, J. E. 1994, ApJ, 424, 189

Lis, D. C., Carlstrom, J. E., & Keene, J. 1991, ApJ, 380, 429

Lis, D. C. & Goldsmith, P. F. 1991, ApJ, 369, 157

Lis, D. C. & Menten, K. M. 1998, ApJ, 507, 794

Lis, D. C., Menten, K. M., Serabyn, E., & Zylka, R. 1994, ApJ, 423, L39

Lis, D. C., Serabyn, E., Zylka, R., & Li, Y. 2001, ApJ, 550, 761

Liszt, H. S. 2006, A&A, 447, 533

—. 2008, A&A, 486, 467

—. 2009, ArXiv e-prints

Main, D. S., Smith, D. M., Heindl, W. A., Swank, J., Leventhal, M., Mirabel, I. F., & Rodríguez, L. F. 1999, ApJ, 525, 901

Marshall, D. J., Fux, R., Robin, A. C., & Reylé, C. 2008, A&A, 477, L21

Martin, C. L., Walsh, W. M., Xiao, K., Lane, A. P., Walker, C. K., & Stark, A. A. 2004, ApJS, 150, 239

Matthews, H. et al. 2009, AJ, 138, 1380

McGary, R. S., Coil, A. L., & Ho, P. T. P. 2001, ApJ, 559, 326

McKee, C. F. & Williams, J. P. 1997, ApJ, 476, 144

Mirabel, I. F., Paul, J., Cordier, B., Morris, M., & Wink, J. 1991, A&A, 251, L43

Miyazaki, A. & Tsuboi, M. 2000, ApJ, 536, 357

Moneti, A., Stolovy, S., Blommaert, J. A. D. L., Figer, D. F., & Najarro, F. 2001, A&A, 366, 106

Morris, M. & Serabyn, E. 1996, ARA&A, 34, 645

Motte, F., Andre, P., & Neri, R. 1998, A&A, 336, 150

Motte, F., André, P., Ward-Thompson, D., & Bontemps, S. 2001, A&A, 372, L41

Motte, F., Bontemps, S., Schilke, P., Schneider, N., Menten, K. M., & Broguière, D. 2007, A&A, 476, 1243

Motte, F., Schilke, P., & Lis, D. C. 2003, ApJ, 582, 277

Nagayama, T., Omodaka, T., Handa, T., Iahak, H. B. H., Sawada, T., Miyaji, T., & Koyama, Y. 2007, PASJ, 59, 869

Nagayama, T. et al. 2009, PASJ, 61, 283

Nummelin, A., Bergman, P., Hjalmarson, A., Friberg, P., Irvine, W. M., Millar, T. J., Ohishi, M., & Saito, S. 1998, ApJS, 117, 427

Oka, T., Geballe, T. R., Goto, M., Usuda, T., & McCall, B. J. 2005, ApJ, 632, 882

Oka, T., Hasegawa, T., Sato, F., Tsuboi, M., & Miyazaki, A. 1998, ApJS, 118, 455

—. 2001a, PASJ, 53, 779

Oka, T., Hasegawa, T., Sato, F., Tsuboi, M., Miyazaki, A., & Sugimoto, M. 2001b, ApJ, 562, 348

Ossenkopf, V. & Henning, T. 1994, A&A, 291, 943

Pierce-Price, D. et al. 2000, ApJ, 545, L121

Pohl, M., Englmaier, P., & Bissantz, N. 2008, ApJ, 677, 283

Reach, W. T. et al. 1995, ApJ, 451, 188

Rodriguez-Fernandez, N. J. 2009, ArXiv e-prints

Rodriguez-Fernandez, N. J. & Combes, F. 2008, A&A, 489, 115

Rodriguez-Fernandez, N. J., Combes, F., Martin-Pintado, J., Wilson, T. L., & Apponi, A. 2006, A&A, 455, 963

Rodríguez-Fernández, N. J., Martín-Pintado, J., Fuente, A., & Wilson, T. L. 2004, A&A, 427, 217

Rosolowsky, E. 2005, PASP, 117, 1403

Rosolowsky, E. et al. 2009, ArXiv e-prints

Schuller, F. et al. 2009, A&A, 504, 415

Scoville, N. Z. & Kwan, J. 1976, ApJ, 206, 718

Serabyn, E., Carlstrom, J., Lay, O., Lis, D. C., Hunter, T. R., & Lacy, J. H. 1997, ApJ, 490, L77+

Serabyn, E., Shupe, D., & Figer, D. F. 1999, in ASP Conf. Ser. 186: The Central Parsecs of the Galaxy, ed. H. Falcke, A. Cotera, W. J. Duschl, F. Melia, & M. J. Rieke, 320–+

Sodroski, T. J. et al. 1994, ApJ, 428, 638

Stahler, S. W., Palla, F., & Ho, P. T. P. 2000, Protostars and Planets IV, 327

Stark, A. A. & Bania, T. M. 1986, ApJ, 306, L17

Stolte, A., Brandner, W., Grebel, E. K., Lenzen, R., & Lagrange, A.-M. 2005, ApJ, 628, L113

Stolte, A., Ghez, A. M., Morris, M., Lu, J. R., Brandner, W., & Matthews, K. 2008, ApJ, 675, 1278

Tamblyn, P. & Rieke, G. H. 1993, ApJ, 414, 573

Tsuboi, M., Handa, T., & Ukita, N. 1999, ApJS, 120, 1

Wang, Q. D., Dong, H., & Lang, C. 2006, MNRAS, 371, 38

Wang, Q. D., Gotthelf, E. V., & Lang, C. C. 2002, Nature, 415, 148

Wardle, M. & Yusef-Zadeh, F. 2008, ApJ, 683, L37

Wright, M. C. H., Coil, A. L., McGary, R. S., Ho, P. T. P., & Harris, A. I. 2001, ApJ, 551, 254

Yusef-Zadeh, F., Braatz, J., Wardle, M., & Roberts, D. 2008, ApJ, 683, L147

Yusef-Zadeh, F. et al. 2009, ApJ, 702, 178

Yusef-Zadeh, F., Hewitt, J. W., & Cotton, W. 2004, ApJS, 155, 421

Yusef-Zadeh, F., Muno, M., Wardle, M., & Lis, D. C. 2007, ApJ, 656, 847

Yusef-Zadeh, F., Nord, M., Wardle, M., Law, C., Lang, C., & Lazio, T. J. W. 2003, ApJ, 590, L103

Zhang, Q. & Fall, S. M. 1999, ApJ, 527, L81

Table 1.   Observing Epochs for the Galactic center data

Begin	End	Instrument
2 Jul 2005	9 Jul 2005	Bolocam
2 Jun 2006	29 Jun 2006	Bolocam + SHARC-II
7 Jul 2007	14 Jul 2007	Bolocam + SHARC-II
13 Apr 2008	14 Apr 2008	SHARC-II

Table 2.   1.1 mm Peak Fluxes and Masses of Selected Regions

l deg	b deg	S_{40}^1 Jy	S_{300}^1 Jy	M_{40}^2 $10^2 M_\odot$	M_{300}^2 $10^2 M_\odot$	N_{40}^3 $10^{21} cm^{-2}$	N_{300}^3 $10^{21} cm^{-2}$	n_{40}^4 $10^2 cm^{-3}$	n_{300}^4 cm^{-3}	Comments
359.13	−0.10	0.45	0.14	4	68	9	3	27	111	Great Annihilator
359.44	−0.10	6.9	1.3	66	561	138	23	413	1017	Sgr C
359.46	−0.03	1.4	1.3	13	561	27	23	81	1017	In Exp. Mol. Ring
359.62	−0.24	8.1	0.60	77	300	162	12	485	495	E. facing comet
359.71	−0.37	2.1	0.36	4	38	42	8	273	647	D=3.9 kpc
359.86	−0.08	9.6	3.36	90	1680	192	66	475	2769	20 km s^{-1} cloud
359.91	−0.31	1.5	0.32	3	33	30	6	195	566	D=3.9 kpc
359.94	−0.04	11.7	2.90	–	1425	234	57	701	2348	Sgr A*, 50 km s^{-1} cloud
359.96	+0.17	3.3	0.77	7	81	65	15	431	1374	IRAS 17417-2851, D=3.9 kpc
359.97	−0.46	3.3	0.41	7	42	66	8	431	728	D=3.9 kpc
0.05	−0.21	1.8	0.41	17	195	36	8	108	335	
0.12	+0.02	1.4	0.78	13	390	27	15	81	642	Near Arches cluster
0.16	−0.06	0.3	0.83	3	413	6	17	18	680	Near Quintuplet cluster
0.26	−0.03	5.7	1.50	54	750	114	30	341	1235	Lima bean
0.28	−0.48	2.3	0.80	5	84	40	17	396	1428	for D=3.9 kpc
0.32	−0.20	3.9	0.59	38	293	78	12	233	482	IRAS 17439-2845
0.41	−0.05	4.2	1.2	39	600	84	24	251	989	
0.41	−0.50	1.8	0.33	4	35	36	6	236	593	for D=3.9 kpc
0.48	−0.00	7.7	2.0	72	975	153	39	458	1607	Notes:
0.53	+0.18	2.4	0.50	23	240	48	11	144	408	
0.68	−0.03	140	16.1	1320	8010	2796	323	8351	13224	Sgr B2
0.84	+0.18	2.0	0.32	18	158	39	6	117	260	
1.12	-0.11	5.1	0.92	48	458	68	12	204	503	Sgr D
1.33	+0.16	0.6	0.36	6	180	12	8	36	297	IRAS 17450-2742
1.60	+0.02	2.1	0.48	20	240	42	9	126	396	
1.74	−0.41	2.3	0.47	21	233	45	9	135	383	IRAS 17481=2738
2.30	+0.26	0.5	0.05	4	23	9	2	27	38	IRAS 17469-2649
2.62	+0.13	1.5	0.12	14	60	30	3	90	99	
2.89	+0.03	0.9	0.30	9	150	18	6	54	248	
2.96	−0.06	0.6	0.14	6	68	12	3	36	111	IRAS 17496-2624
3.09	+0.16	0.9	0.15	9	75	18	3	54	123	
3.14	+0.41	0.9	0.15	9	75	18	3	54	123	
3.31	−0.40	1.5	0.17	14	83	30	3	90	137	
3.34	+0.42	1.2	0.30	11	150	24	6	72	248	
3.35	−0.08	2.3	0.12	14	60	45	3	135	99	
3.41	+0.88	0.8	0.06	7	30	15	2	45	50	IRAS 17470-2533
3.44	−0.35	4.8	0.26	45	128	96	5	288	210	
4.00	+0.34	0.9	0.06	9	30	18	3	54	50	IRAS 17504-2519
4.39	+0.08	0.8	0.15	7	75	15	3	45	123	
4.43	+0.13	2.1	0.23	20	113	42	5	126	186	

[1] **Flux densities:** S_{40} is the flux (in Jy per beam) measured in a 33″ diameter effective CSO beam (equivalent to a 40″ diameter top-hat beam with a radius of 19.82″). S_{300} is the average flux measured (in Jy per beam) in a solid angle corresponding to a 300″ diameter "top-hat" beam. [2] **Masses:** M_{40} and M_{300} are the masses estimated for an assumed dust temperature of 20 K and a distance of D = 8.5 kpc (unless otherwise noted) in 40″ and 280″ apertures. The tabulated values are in Solar masses ($M_\odot$) divided by 10^2. [3]: **Column densities:** N_{40} and N_{300} are the equivalent average column densities estimated in the 40″ and 300″ apertures, assuming that the emission is uniformly spread over the aperture. These are lower bounds on the actual column densities as discussed in the text. The units are in cm^{-2} divided by 1.0×10^{21} which is about $A_V \approx 1$ magnitude. [4] **H$_2$ volume densities:** n_{40} and n_{300} are the equivalent average volume densities of H$_2$ estimated in the 40″ and 300″ apertures under the assumption that the clumps are spherical with a radius equal to the projected radius of the measurement aperture in which the emitting material is spread uniformly. These are a lower bounds on the actual densities as discussed on the text. The units for n_{40} are in cm^{-3} divided by 10^2. The units for n_{300} are in cm^{-3}.

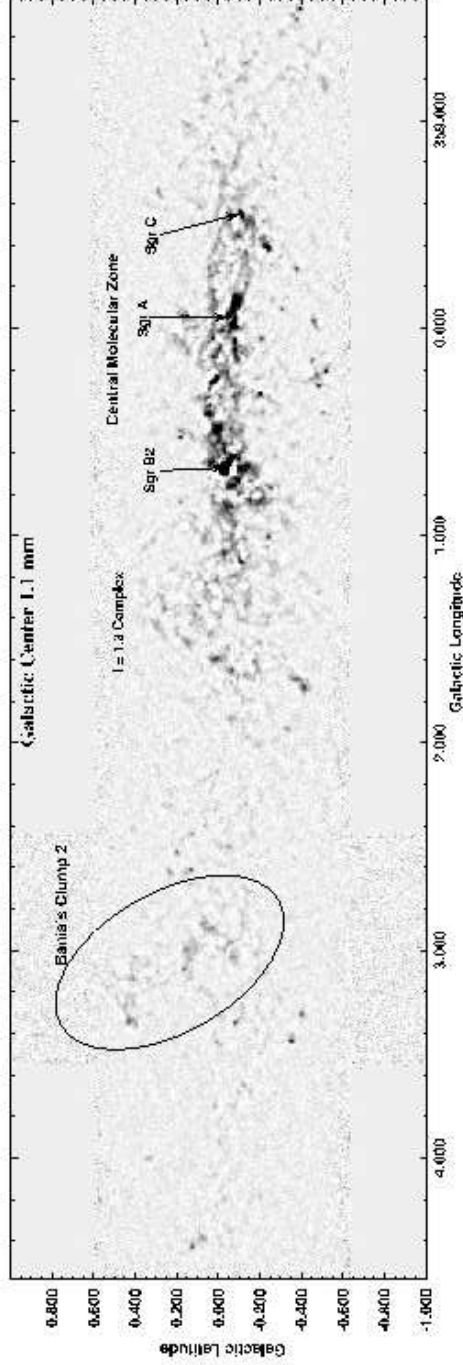Fig. 1.— A 1.1 mm BGPS continuum image showing the central parts of the Galactic Plane from $l = 358.5°$ to $4.5°$. This image has been processed with 13 PCA components and 50 iterations of the iterative mapper. While this level of processing restores much of the faint structure, it removes flux from bright sources ($>$ about 5 Jy) and creates significant negative bowls around them. The display presented here uses a logarithmic scale from -0.5 to 100 Jy/beam.
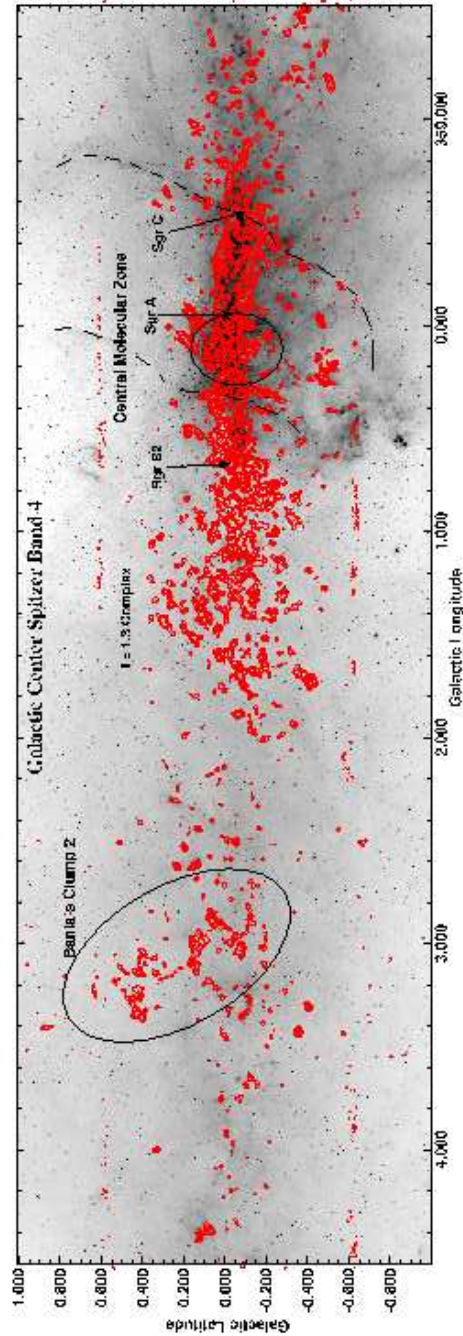
Fig. 2.— BGPS 1.1 mm contours superimposed on the Spitzer Space Telescope 8 μm image shown on a logarithmic intensity scale and at the same spatial scale as Figure 1. Various regions discussed in the text are marked. Bania's Clump 2 is shown on the left and the $l = 1.3°$ complex is located in the middle. The oval to the left of Sgr A shows the approximate outline of the infrared cavity that contains the Arches and Quintuplet clusters and is rimmed by mid-IR and radio continuum emission. The dashed line-segments illustrate the apparent walls of a larger cavity bounded by Spitzer 8 and 24 μm emission. The interior of this region is filled with 20 cm radio continuum. See text for discussion. The 1.1 mm contour levels are at 0.10, 0.20, 0.37, 0.73, 1.4, 2.7, 5.3, 10.3, and 20 Jy/beam.
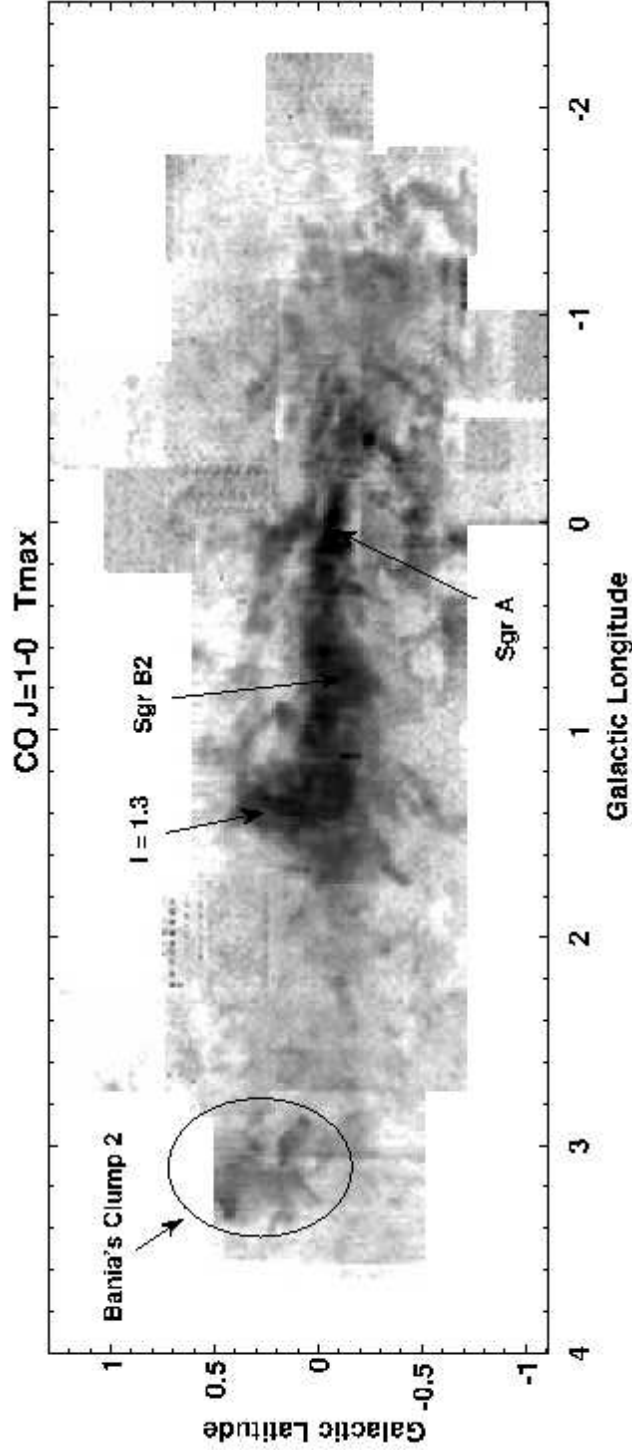
Fig. 3.— The Central Molecular Zone in the the Galactic center as traced by the peak antenna temperature, T_A^* of the J =1–0 ^{12}CO transition. The location of Bania's Clump 2 is indicated along with some of the other prominent Galactic center features. Taken from the AT&T Bell Laboratories data presented by Bally et al. (1987, 1988).
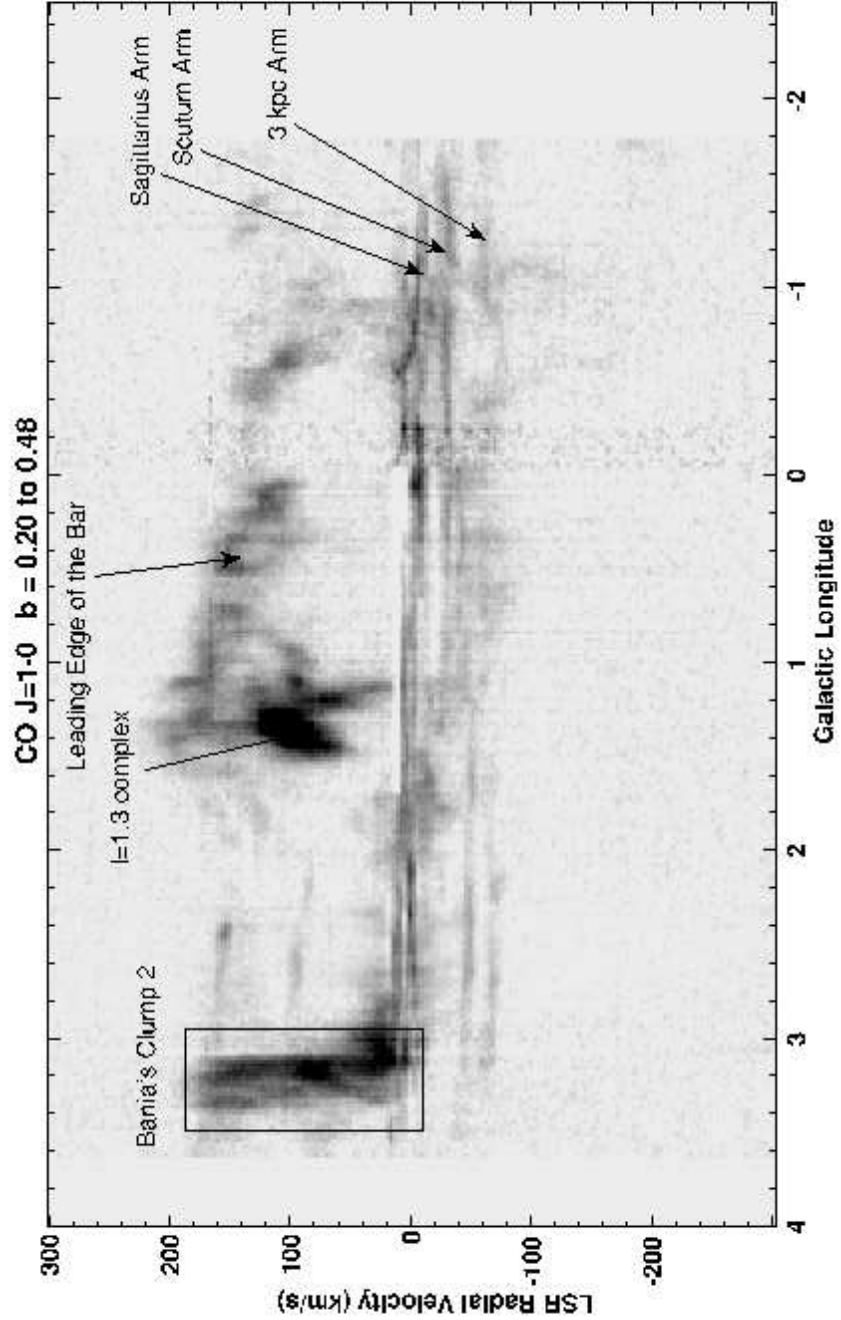
Fig. 4.— A longitude-velocity diagram showing the Central Molecular Zone in the Galactic center as traced by the peak antenna temperature, T_A^* of the J =1–0 ^{12}CO transition averaged over the Galactic latitudes from $b = 0.20°$ to $0.48°$. The location of Bania's Clump 2 is indicated along with some of the other prominent Galactic center features. Taken from the AT&T Bell Laboratories data presented by Bally et al. (1987, 1988).
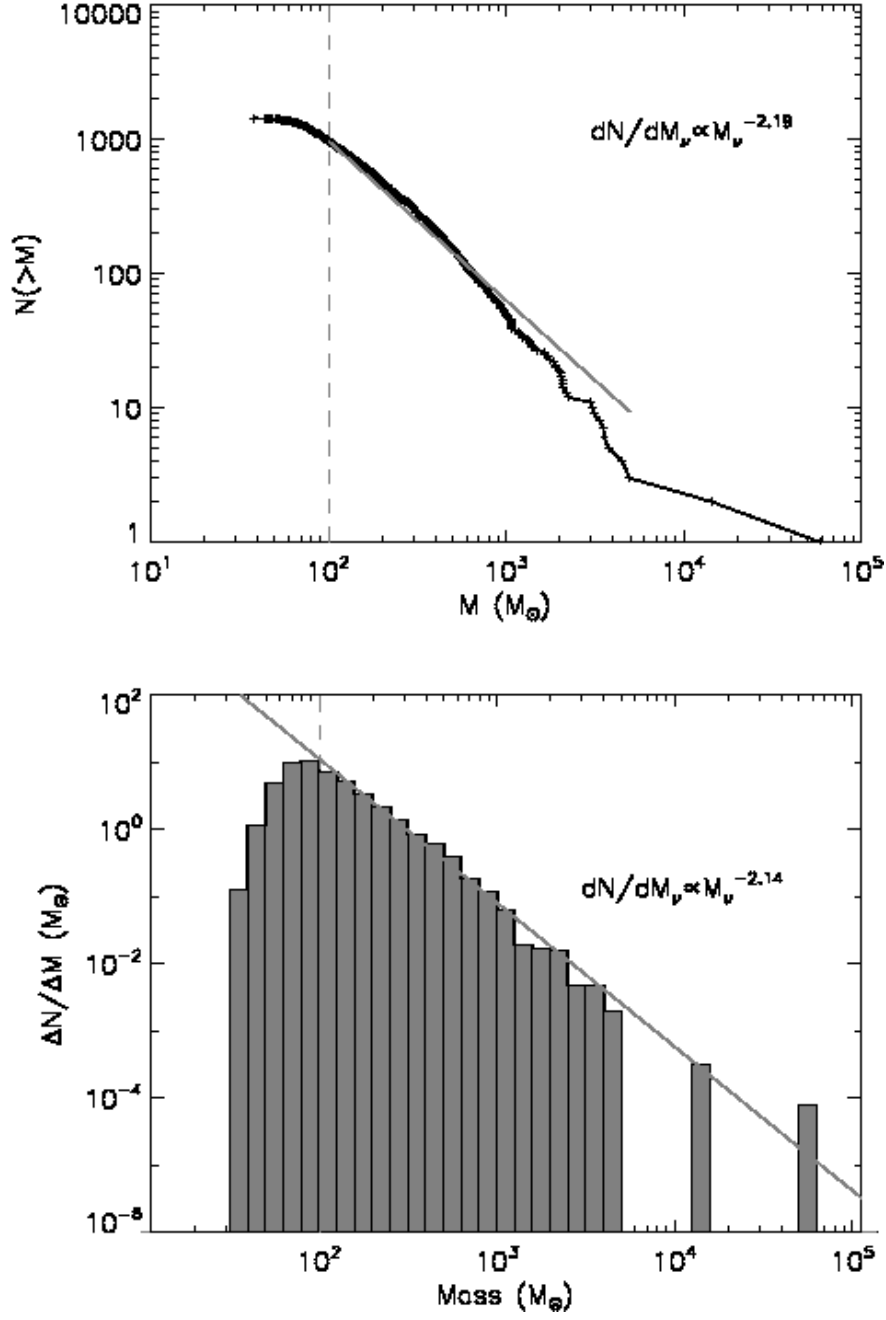
Fig. 5.— The mass spectrum of Bolocat clumps derived from the fluxes measured in a 40″ diameter aperture under the assumption that all Bolocat clumps are located at D = 8.5 kpc and have a temperature of T = 20 K. The top panel shows the cumulative distribution along with a line representing a differential mass distribution with the indicated slope. The bottom panel shows the differential mass distribution with counts in bins whose width increased logarithmically along with a best fit slope to the differential mass distribution for constant width mass-bins.
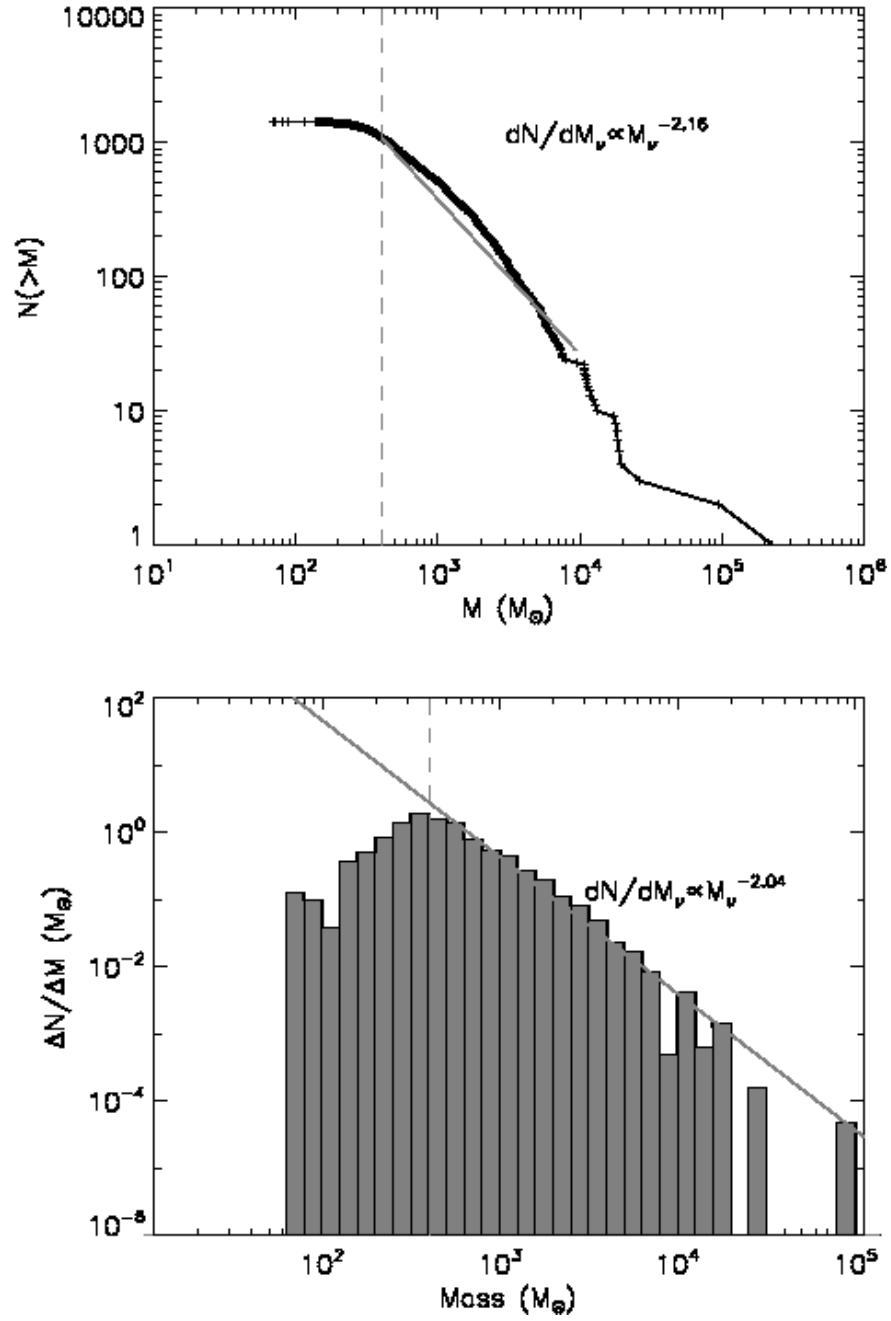
Fig. 6.— Same as Figure 5 but using fluxes measured in a 120″ diameter aperture.
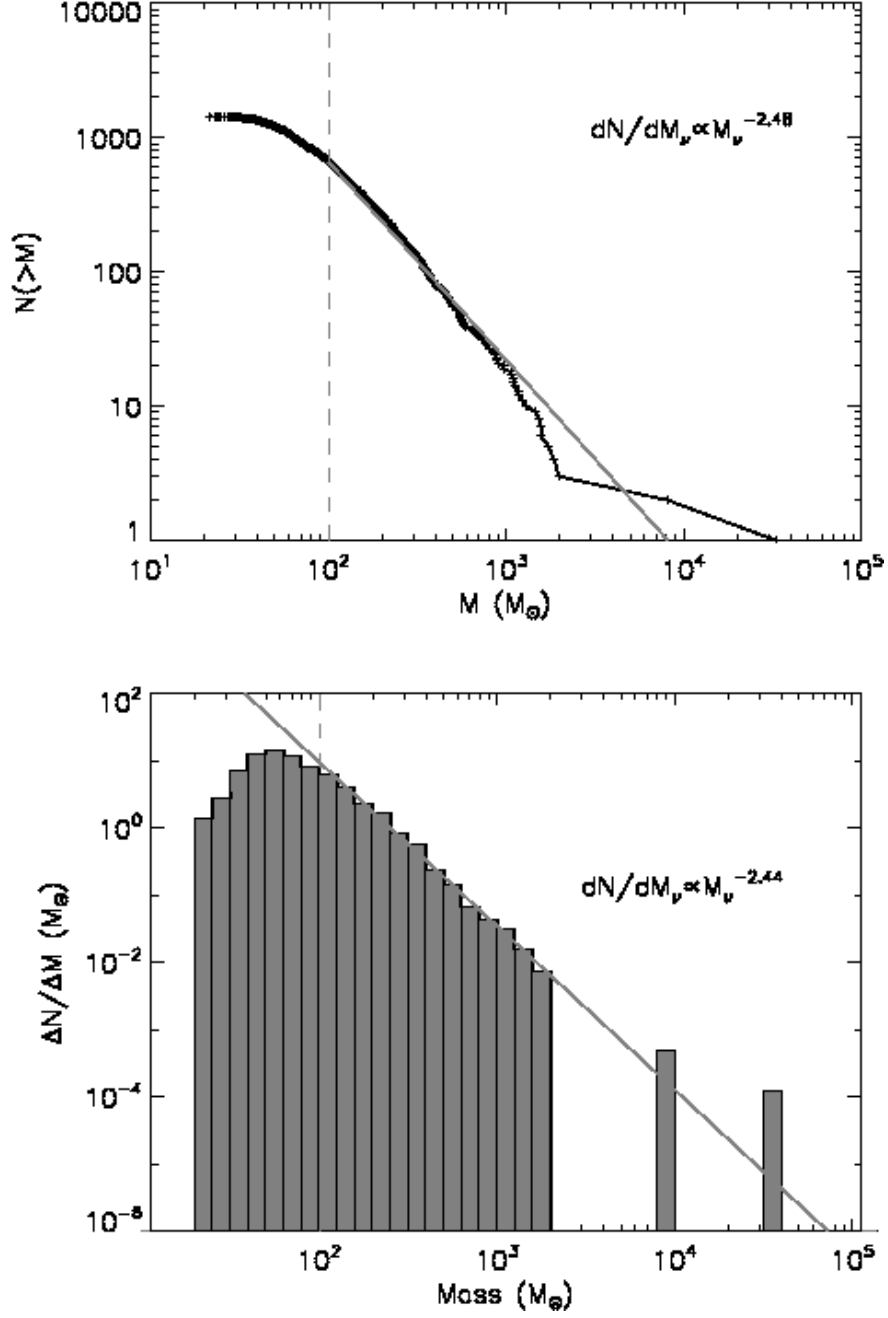
Fig. 7.— Same as Figure 5 using fluxes measured in a $40''$ diameter aperture but assuming that the dust temperature declines with increasing distance, d, from Sgr A as a power-law with $T = T_0 d^{-0.2}$. See text for details.
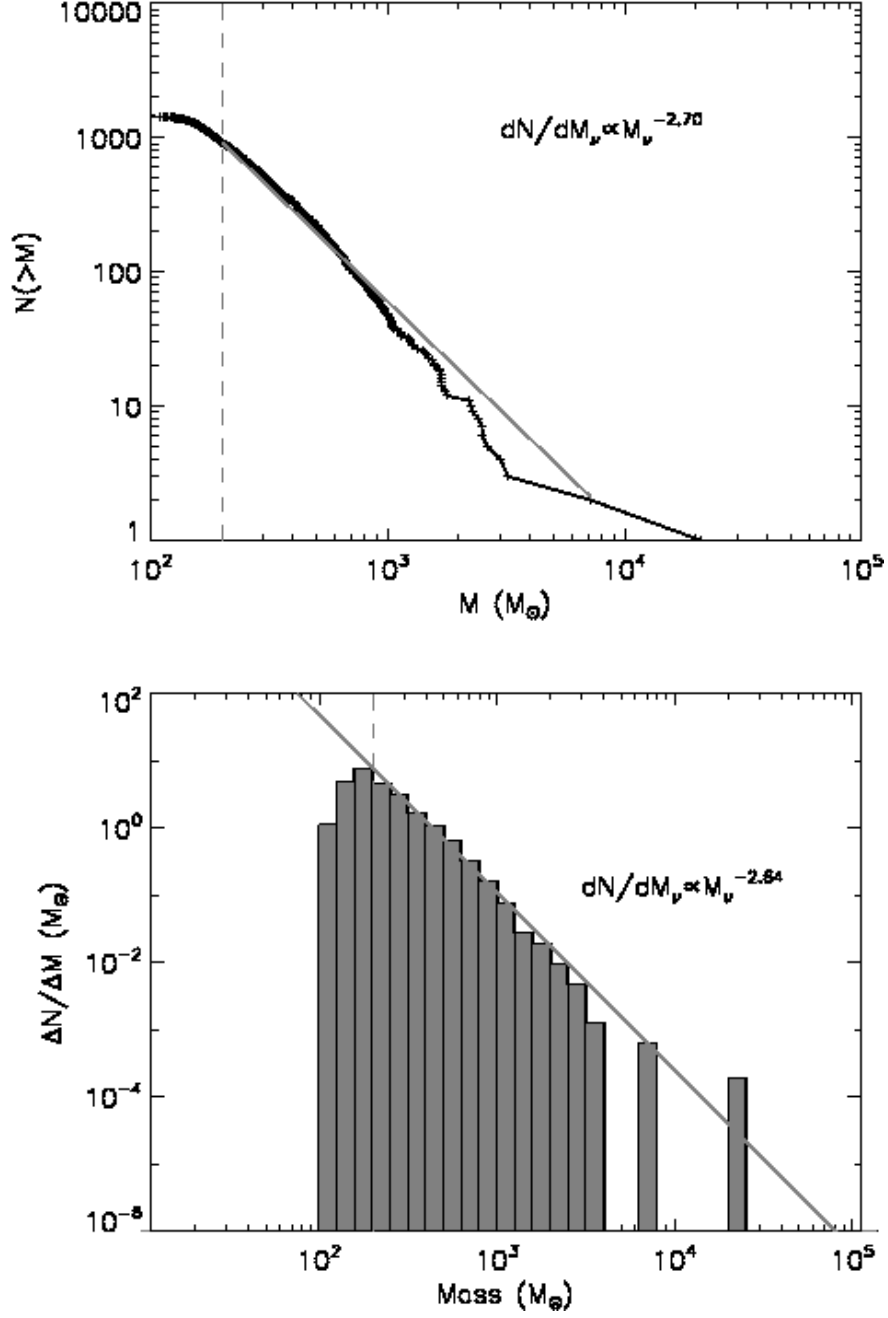
Fig. 8.— Same as Figure 5 using fluxes measured in a $40''$ diameter aperture but assuming that the dust temperature increases with increasing 1.1 mm flux, F, as a power-law with $T = T_0 F^{0.2}$. See text for details.
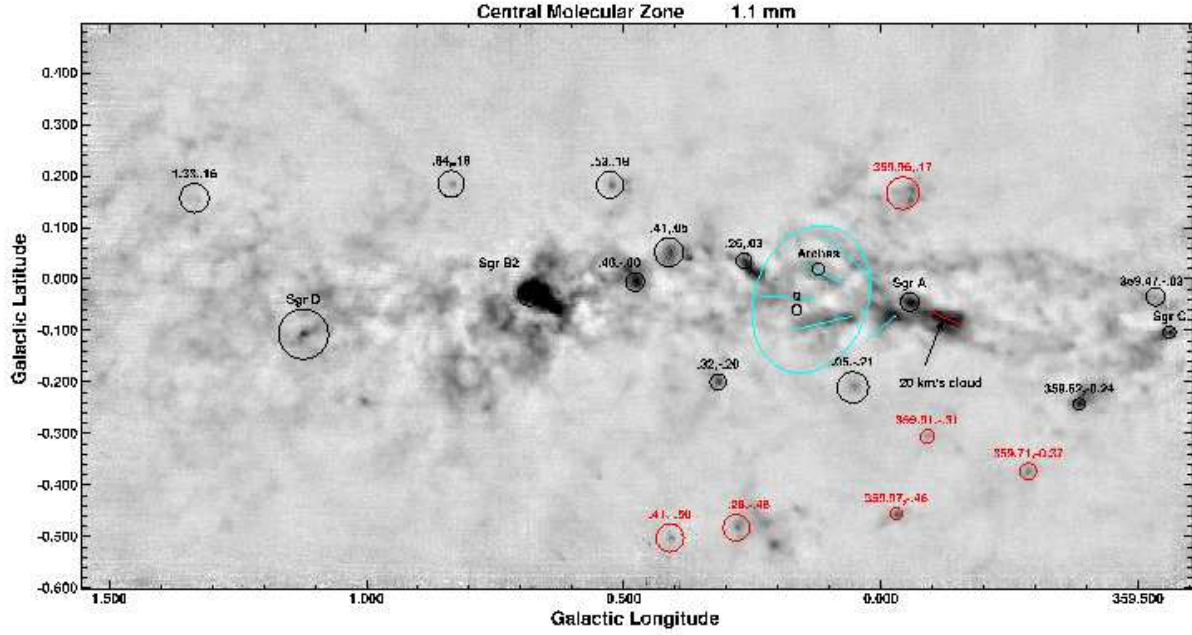
Fig. 9.— The 1.1 mm image of the Central Molecular Zone. The red lines show the orientations and locations of cometary clouds and chains of clumps that face Sgr A. These features are located in the interior of the cavity surrounding Sgr A that is discussed in the text and form the walls of its multiple chambers. The features marked in red are likely to be foreground clouds at an assumed distance of 3.9 kpc as indicated in Table 1.
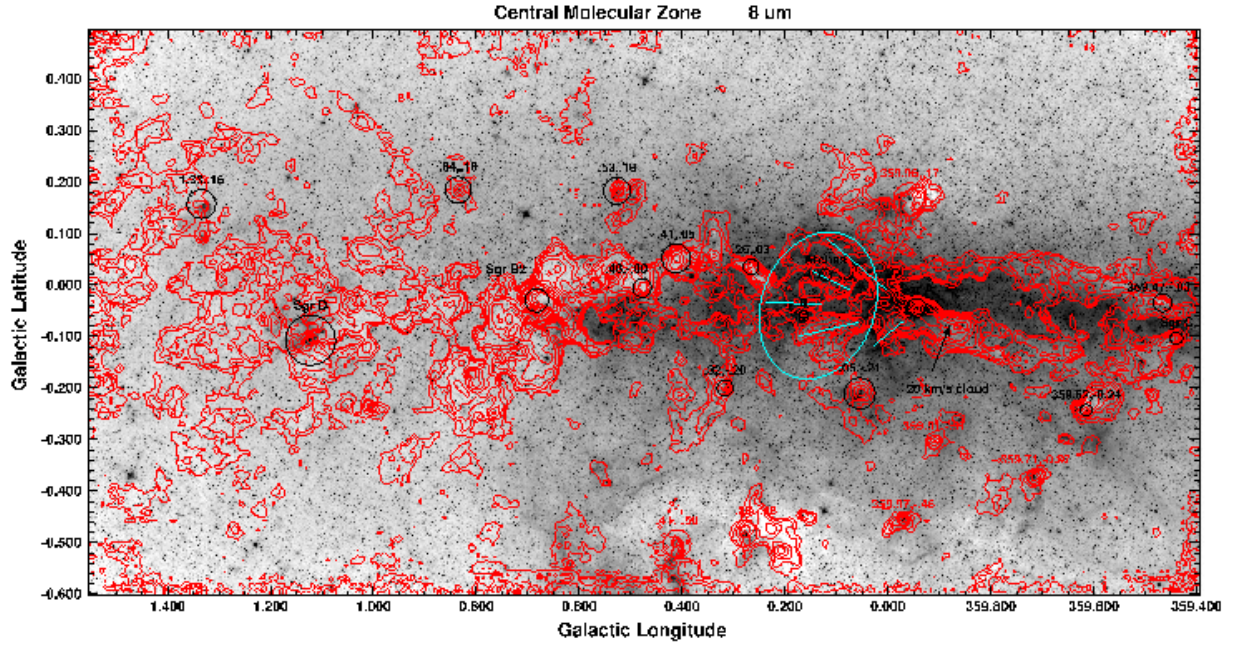
Fig. 10.— Contours of 1.1 mm dust continuum emission from the CMZ superimposed on the Spitzer IRAC 8 μm image (Arendt et al. 2008) show with a logarithmic greyscale presented at the same spatial scale as Figure 9. The 1.1 mm contour levels are 0.3, 0.45, 0.75, 1.2, 2.0, 3.0, 5.0, 7.5, 12.0, 20, and 30 Jy/beam.
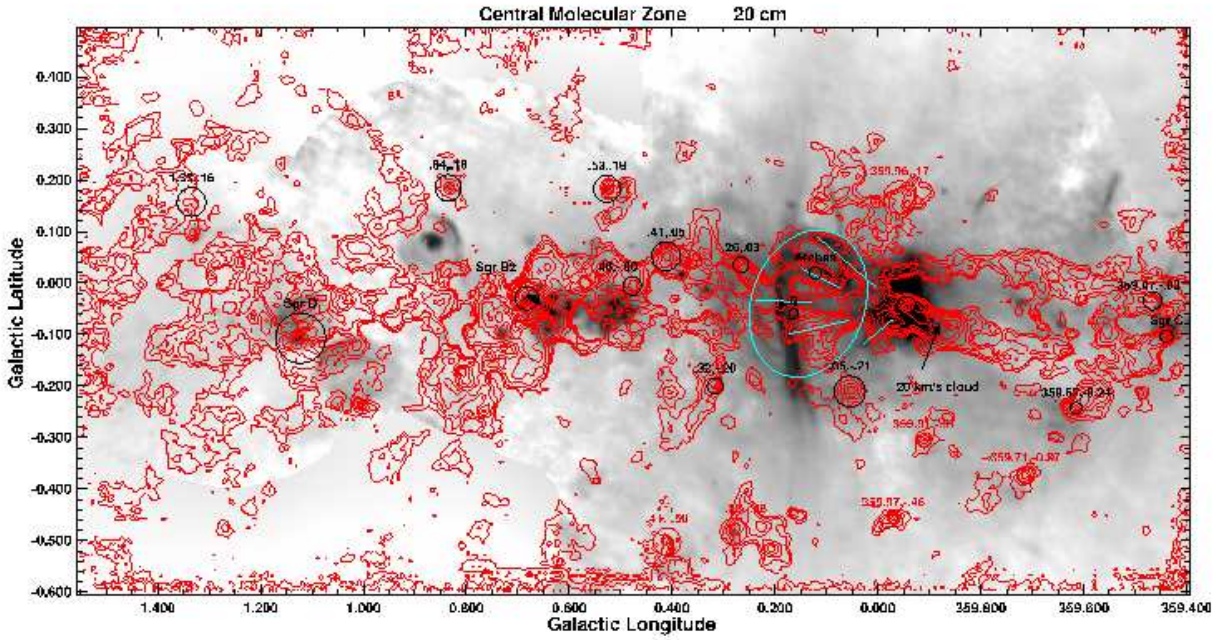
Fig. 11.— Contours of 1.1 mm dust continuum emission from the CMZ superimposed on the 20 cm radio continuum image from Yusef-Zadeh et al. (2004) shown on a logarithmic greyscale and presented at the same spatial scale as Figure 9. The 1.1 mm contour levels are 0.3, 0.45, 0.75, 1.2, 2.0, 3.0, 5.0, 7.5, 12.0, 20, and 30 Jy/beam.
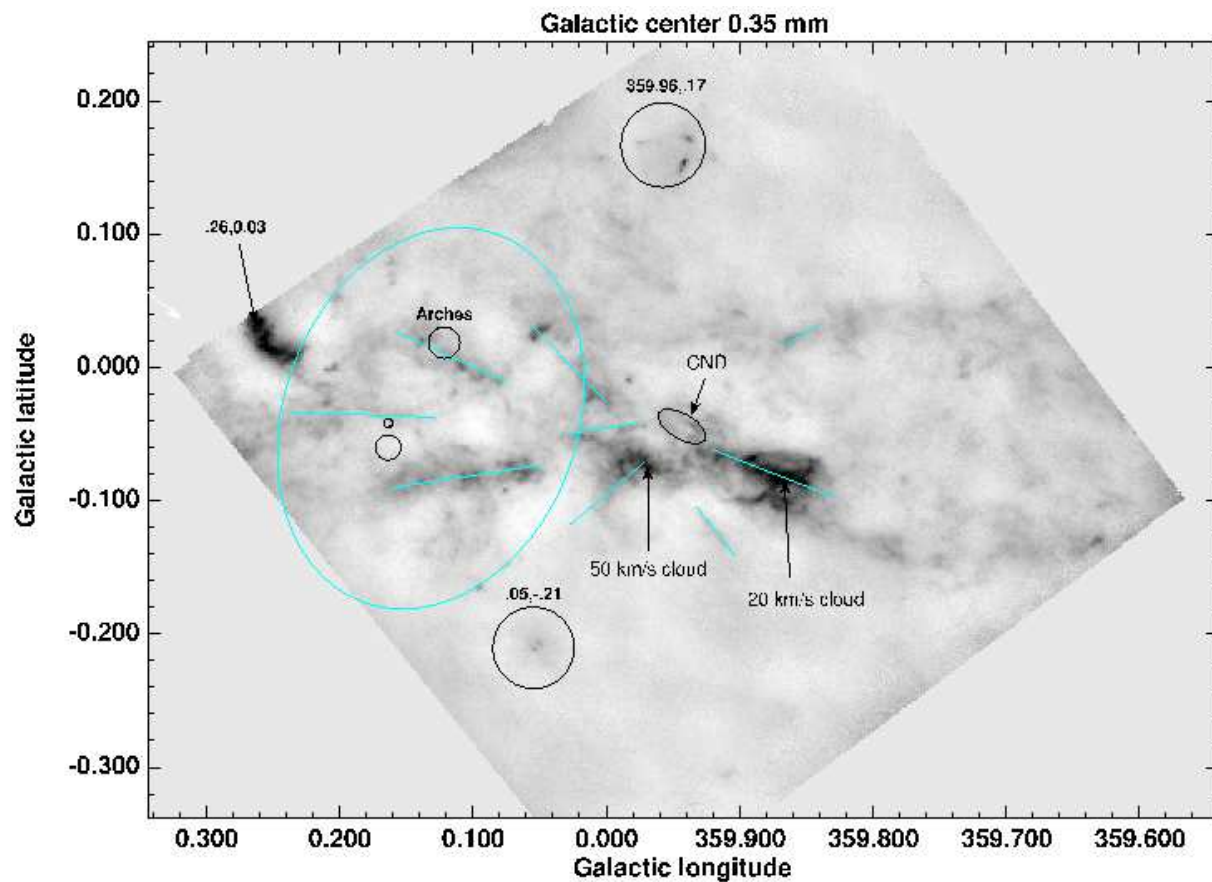
Fig. 12.— A SHARC-II 350 μm image showing warm dust continuum emission from the vicinity of Sgr A in the center of the Galaxy with 9″ resolution. This image has been "unsharp-masked" to suppress large scale structure and to match the spatial frequency response of the Bolocam 1.1 mm images.
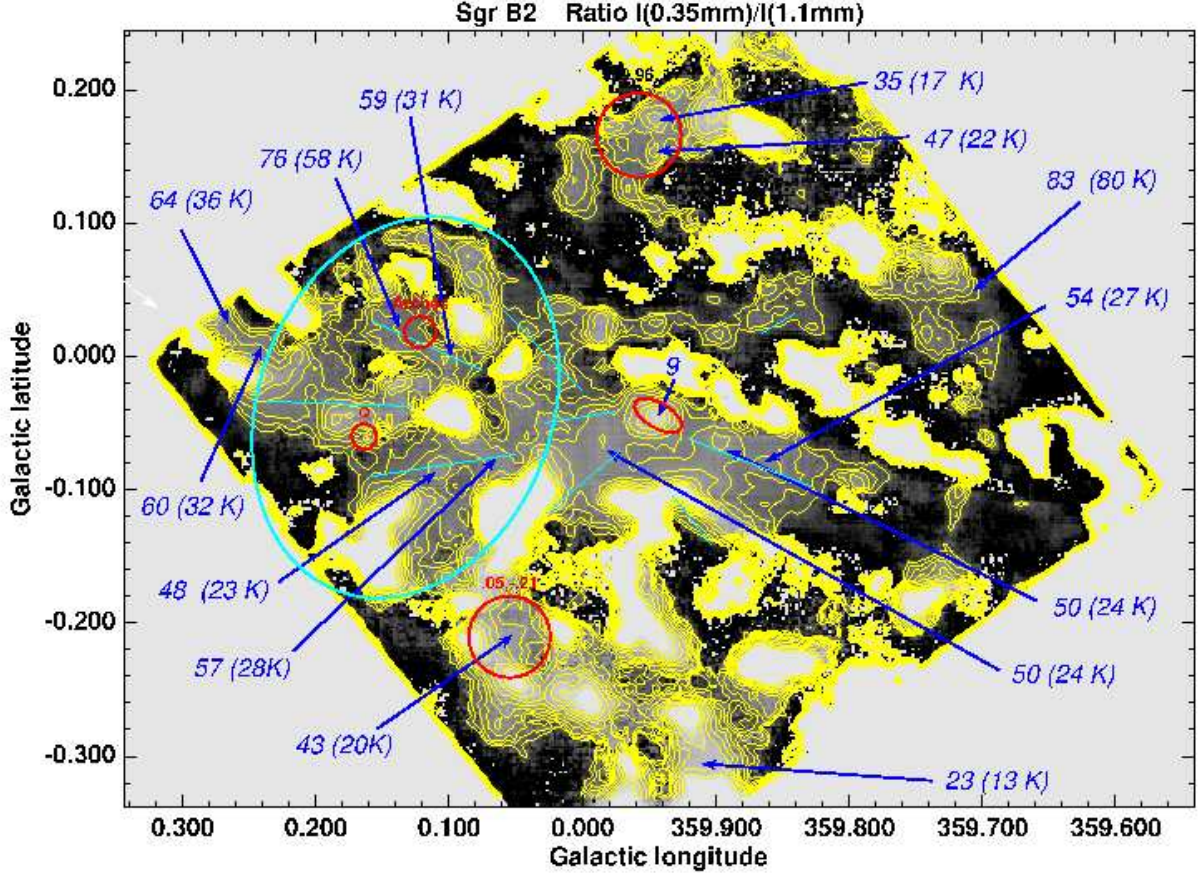
Fig. 13.— A map showing the ratio of the surface brightness of 350 μm emission divided by 1.1 mm emission in the vicinity of Sgr A. The display range goes from 0 (white) to 100 (black). Regions with ratios larger than 100, which corresponds to the Rayleigh-Jeans limit for $\beta = 2.0$ dust have been masked and are shown as white. The ratios at the edge of the SHARC-II field are spurious. As discussed in the text, the 350 μm map has been convolved with a gaussian kernel to have the same effective beam size as the 1.1 mm map ($33''$ effective beam). The italic numbers indicate the flux ratio at the locations indicated by the associated arrows. The numbers in parentheses give the derived dust temperatures for an emissivity power-law index of $\beta = 2.0$. Emission from the central black hole dominates the 1.1 mm flux originating in the center of the CND. Because the source of emission is unlikely to dust, no dust temperature is given.
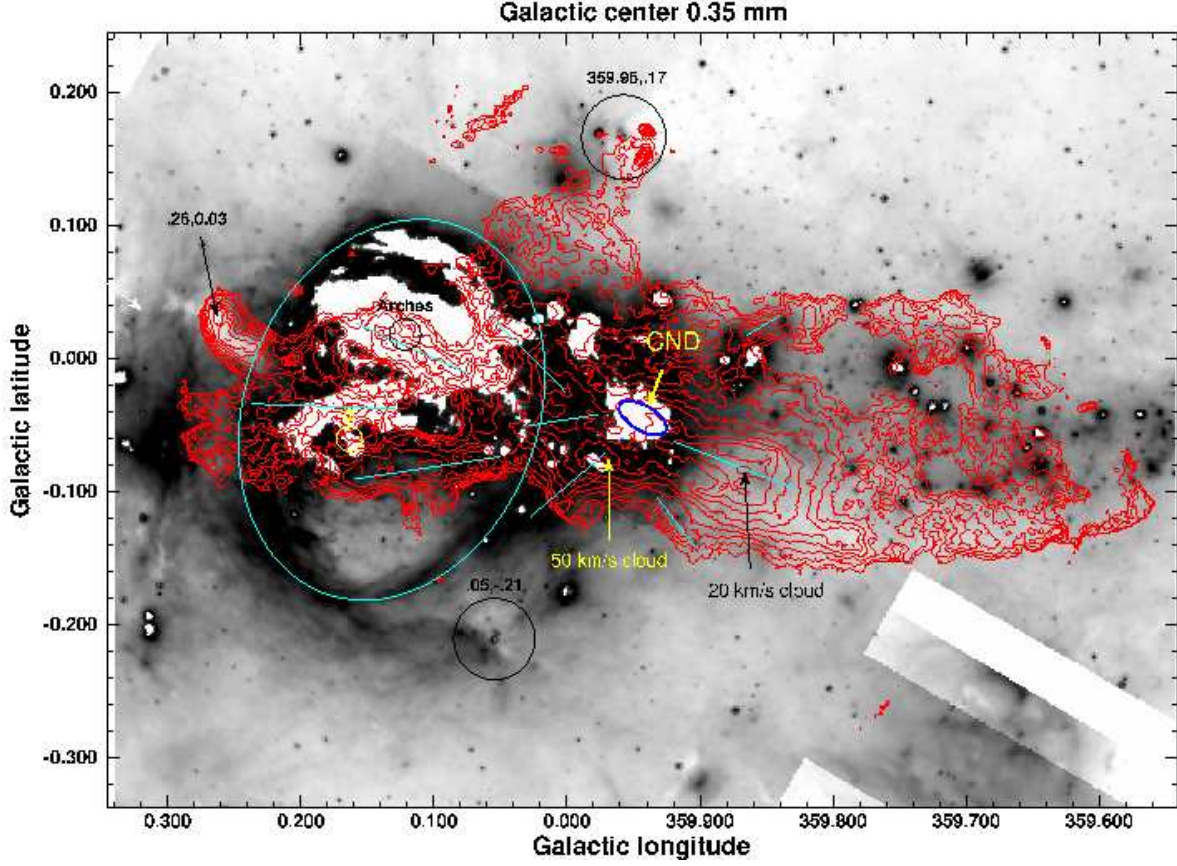
Fig. 14.— Contours of SHARC-II 350 μm emission superimposed on a greyscale rendition of the 24 μm Spitzer image showing the vicinity of Sgr A (Yusef-Zadeh et al. 2009) displayed on a logarithmic intensity scale. The sharp-edged white regions indicate locations where the Spitzer image is saturated. Contour levels are: 4.5, 7, 9.0, 13, 18, 26, 37, 53, 75, 106, and 150 Jy/beam.
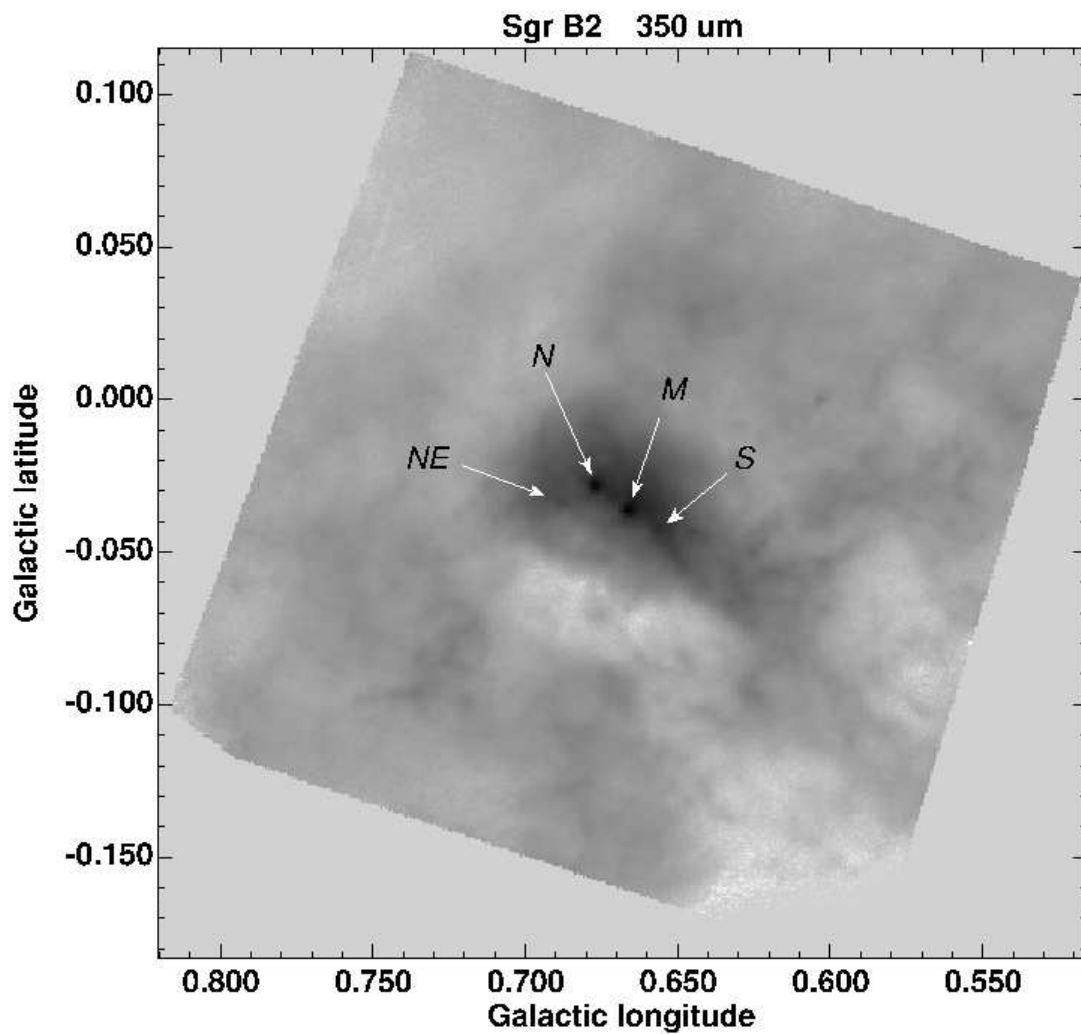
Fig. 15.— A SHARC-II 0.35 mm image showing the Sgr B2 complex on a logarithmic intensity scale. The bright emission is contoured with levels shown at 100, 130, 170, 220, 285, 371, 482, 627, 814, 1060, and 1375 Jy/beam. The two peaks in the center correspond to Sgr B2N and SgrB2 Main.
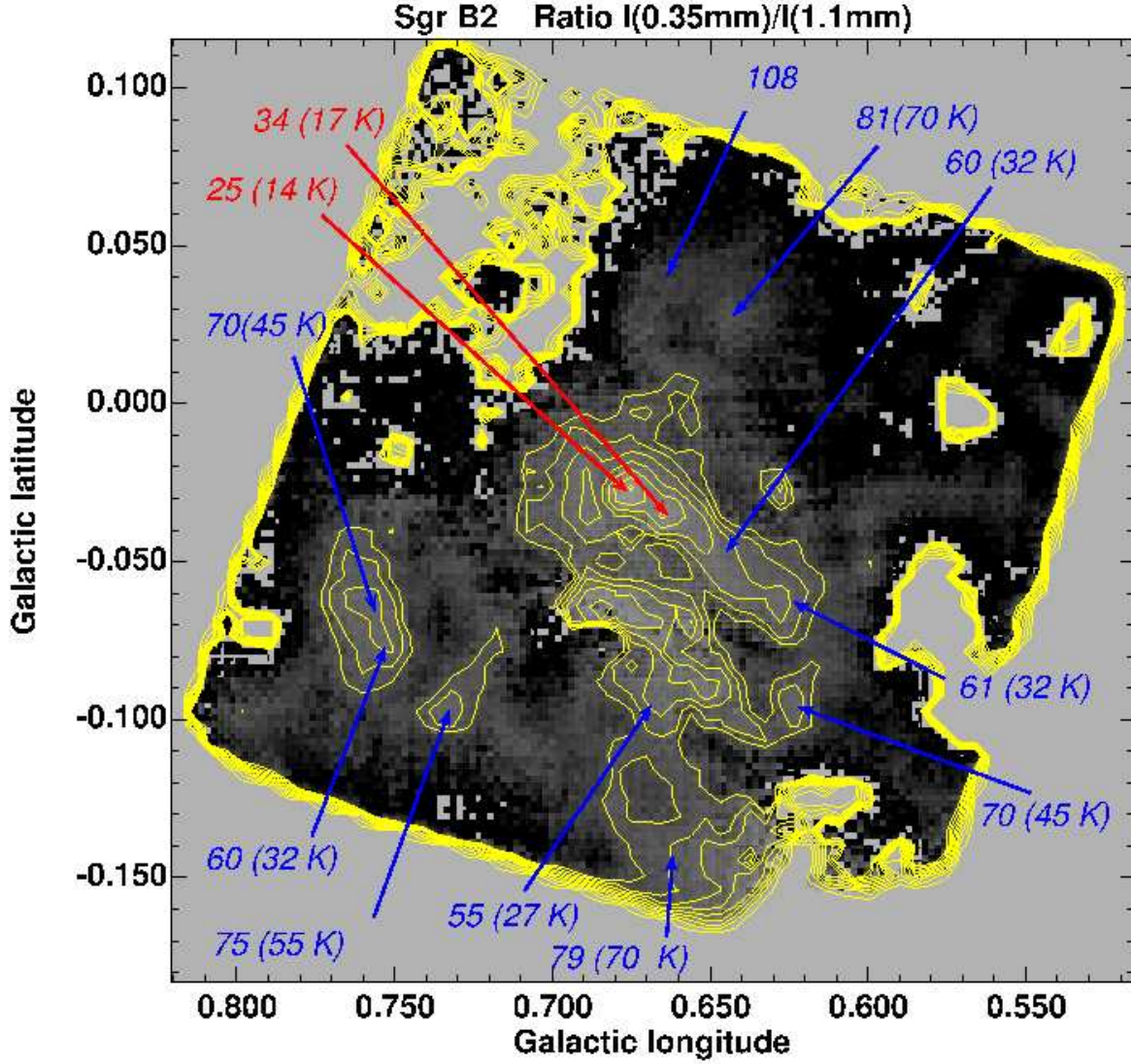
Fig. 16.— A map showing the ratio of the surface brightness of 350 μm emission divided by 1.1 mm emission in the vicinity of Sgr B2. The display range goes from 0 (white) to 100 (black). Regions with ratios larger than 100, which corresponds to the Rayleigh-Jeans limit for $\beta = 2.0$ dust have been masked and are shown as white. The ratios at the edge of the SHARC-II field are spurious. As discussed in the text, the 350 μm map has been convolved with a gaussian kernel to have the same effective beam size as the 1.1 mm map (33″ effective beam). The italic numbers indicate the flux ratio at the locations indicated by the associated arrows. The numbers in parentheses give the derived dust temperatures for an emissivity power-law index of $\beta = 2$.
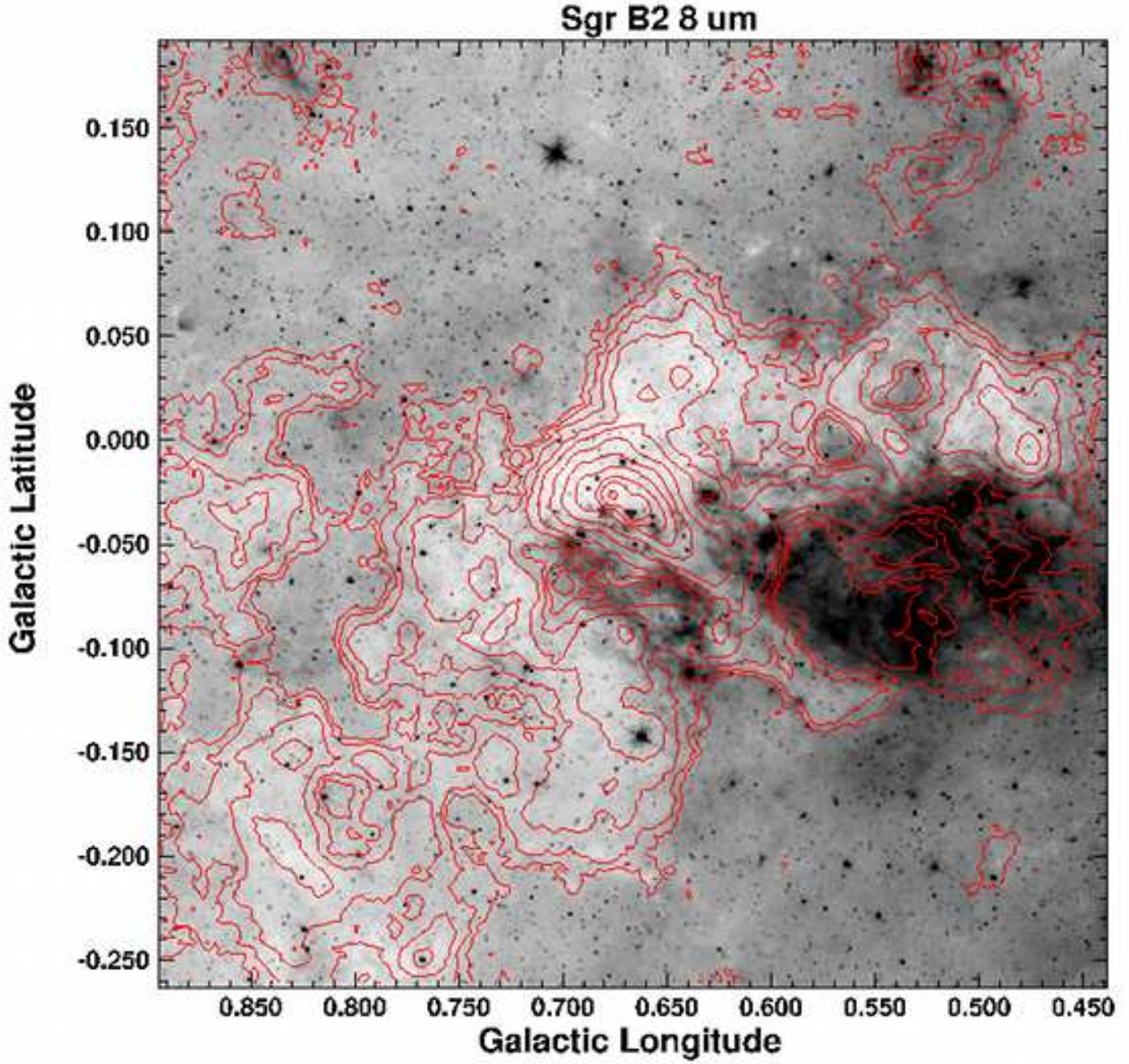
Fig. 17.— The Bolocam 1.1 mm contours superimposed on a Spitzer 8 μm image displayed in logarithmic intenstiy. Contour levels are at 0.30, 0.54, 1.0, 1.8, 3.3, 6.0, 11, 20, 36, 66, and 120.0 Jy/beam.
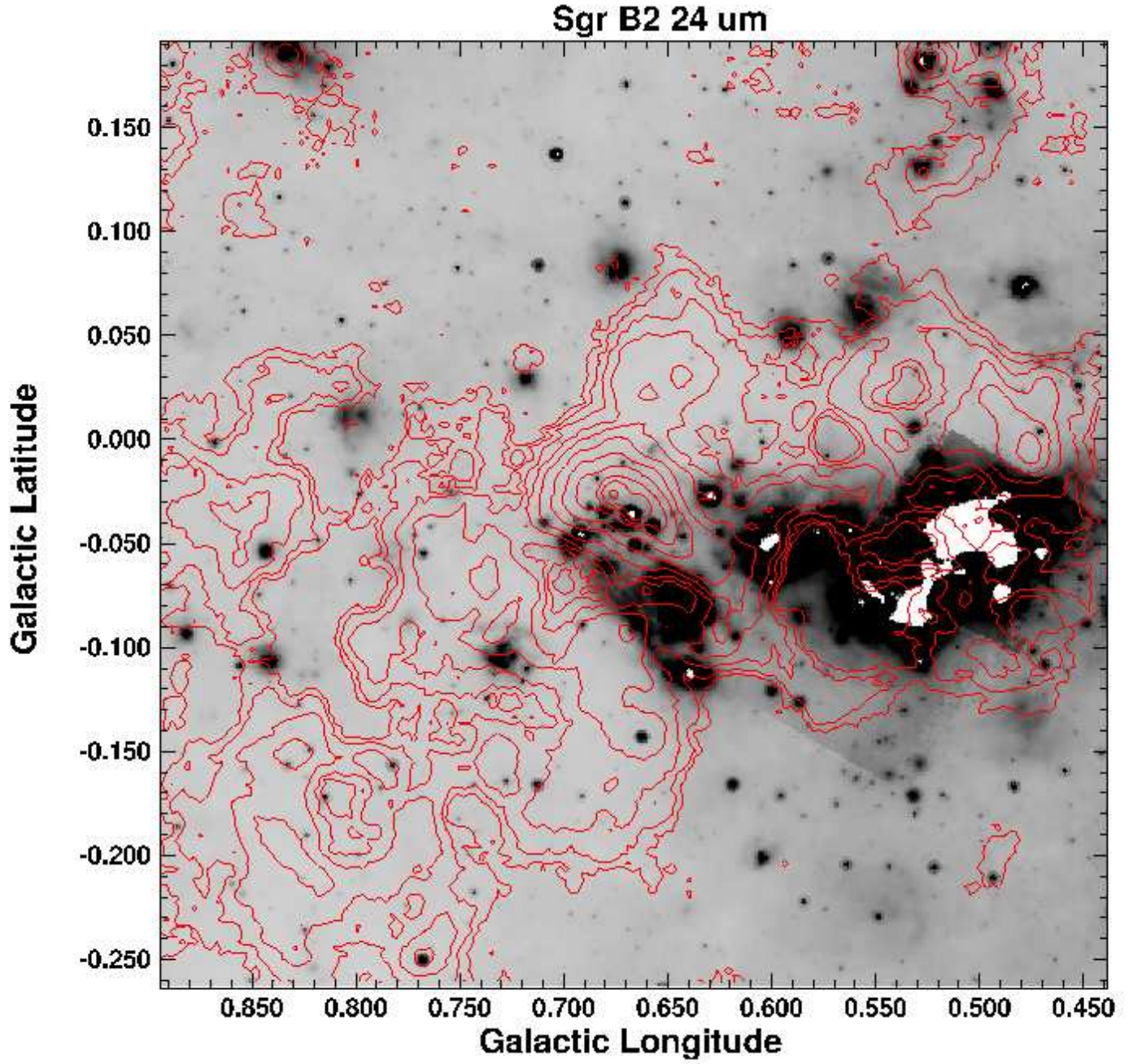
Fig. 18.— The Bolocam 1.1 mm contours superimposed on a Spitzer 24 μm image displayed in logarithmic intenstiy. Contour levels are at 0.30, 0.54, 1.0, 1.8, 3.3, 6.0, 11, 20, 36, 66, and 120.0 Jy/beam.
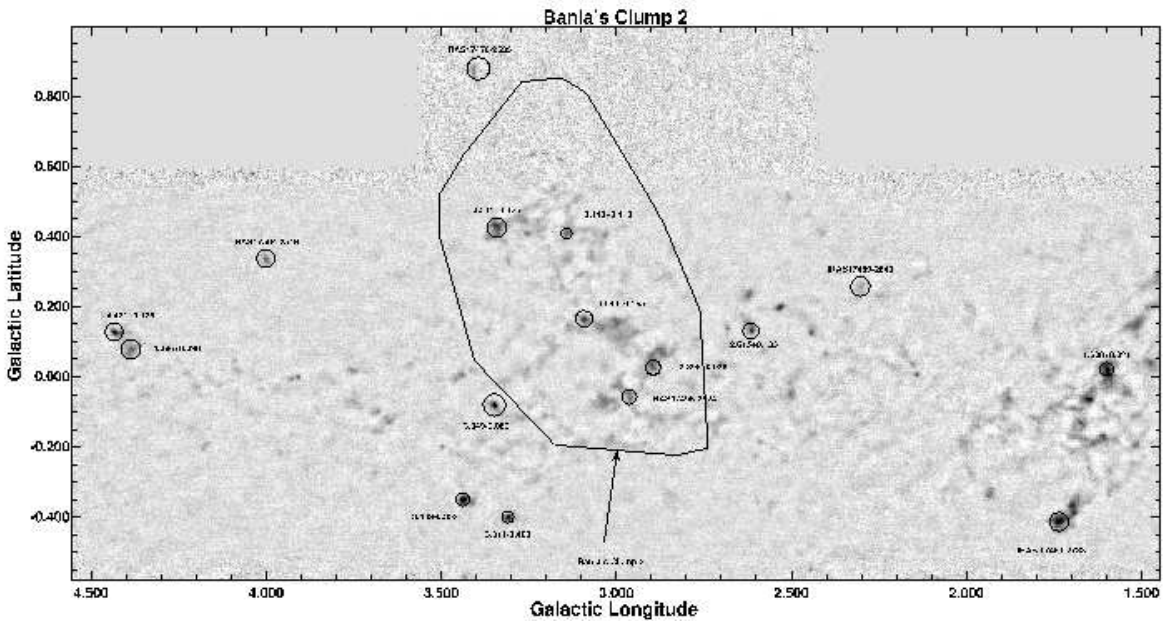
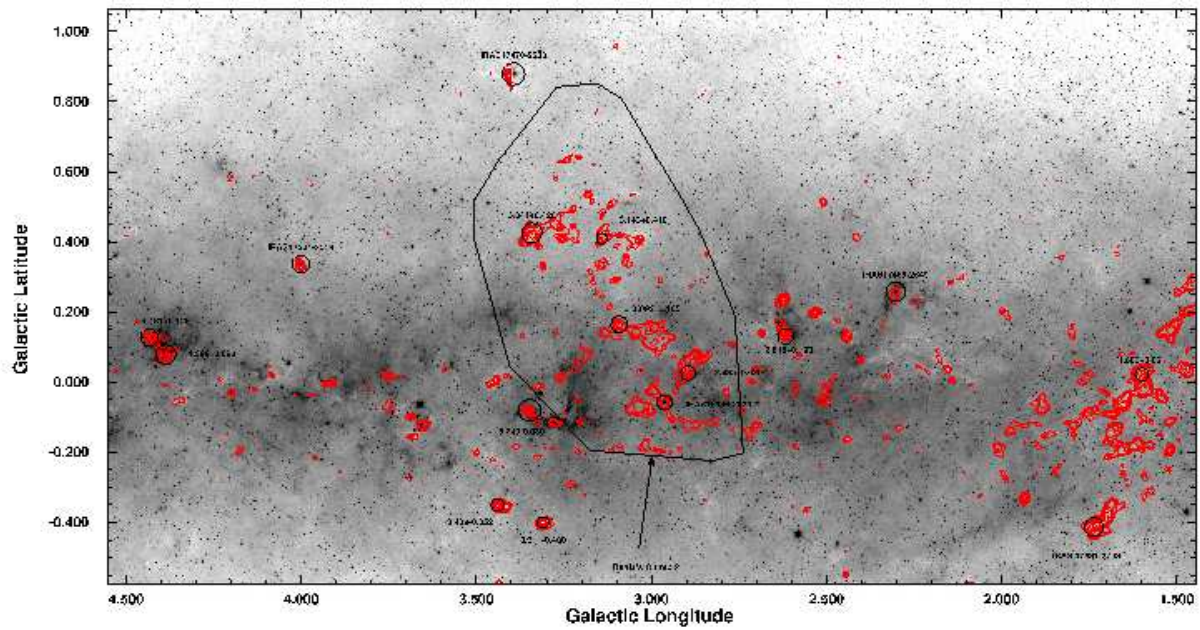Fig. 19.— A 1.1 mm image centered at $l = 3°$, the region that contains Bania's Clump 2 with carious clumps marked.

Fig. 20.— Contours of 1.1 mm continuum emission centered at $l = 3°$, the region that contains Bania's Clump 2 (red), superimposed on the GLIMPSE2 8 μm image. Contour levels are at 0.15, 0.24, 0.38, 0.6, 1.0, 1.5, 2.4, 3.8, 6.0, 10, and 15 Jy/beam.
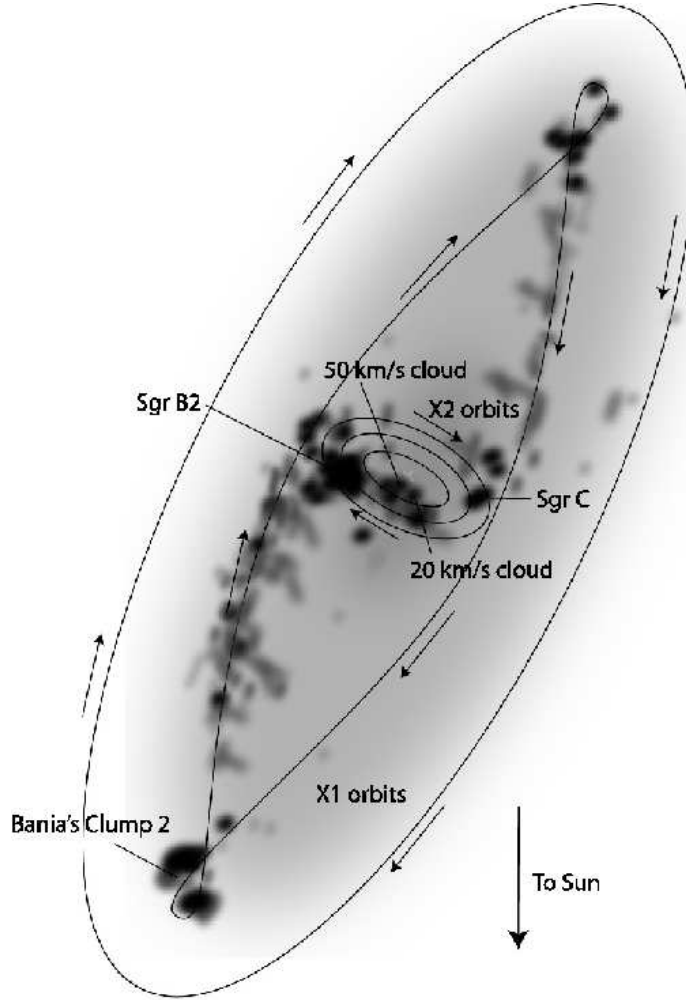
Fig. 21.— A cartoon showing a face-on view of the central 500 pc region of the Milky Way as viewed from the northern Galactic pole. The Sun is located below the figure and positive longitudes to the left. The diffuse grey-scale shows the current orientation of the stellar bar, thought to have its major axis tilted between 20 to 45° with respect to our line-of sight. The large oval show a non intersecting x1 orbit; Lower angular momentum x1 orbits become self-intersecting. The "rhombus" of molecular emission in *l-V* diagrams probably occupies the receding and approaching portions of the innermost x1 orbits. The 3 smaller inscribed ellipses show x2 orbits. Bania's Clump 2 is thought to be located on the receding portion the last stable x1-orbit where it is self-intersecting. Approaching gas presumably enters as an atomic phase; shock-copresison and subsequent cooling results in its conversion to the molecular phase. The receding gas above Bania's clump 2 traces the leading edge of the bar and populates extended network of positive velocity clouds in *l-V* diagrams such as Figure 4. The CMZ emission is associated with gas mostly located on the near-side of the Galactic center on the x2 orbits. The possible locations of the Sgr C, 20 km $^{-1}$, 50 km $^{-1}$, and Sgr B2 complexes are indicated.
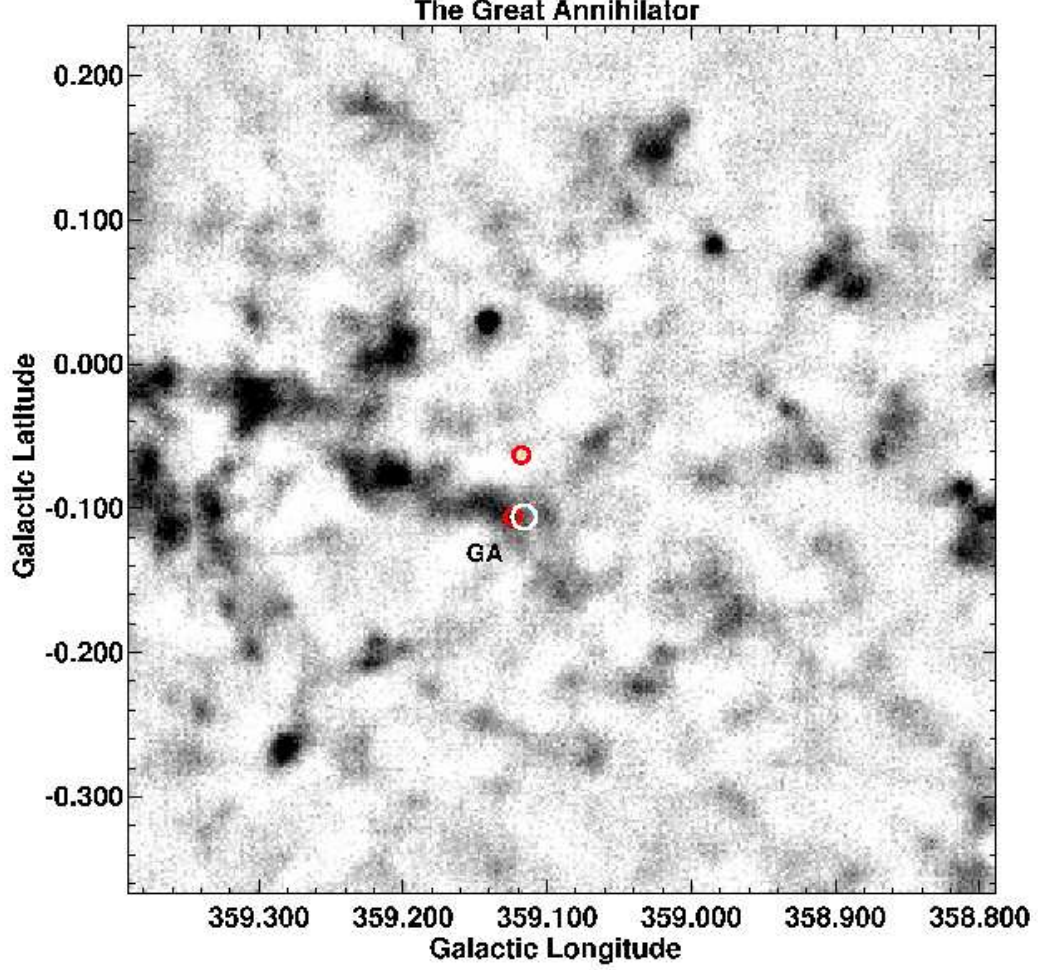
Fig. 22.— A 1.1 mm image showing the field of view surrounding the "Great Annihilator" (GA) thought to be a major source of 511 keV positronium emission. The large white circle is 40″ in diameter and shows the location of the X-ray source 1E1740.7-2942. The small circles mark the position centroids of two HCO^+ clumps detected by Hodges-Kluck et al. (2009). The circle next to the GA is their clump 1; the circle above is their clump 2b which does not appear to be associated with 1.1 mm emission. The display is linear intensity.

Table 3. 1.1 mm Masses, Column Densities, and Densities for 1428 Bolocat Clumps

BGPS (#)	l deg	b deg	R.A. J(2000)	Dec. J(2000)	$M(40'')^1$ $M_\odot$	$N_{40}(H_2)^1$ cm^{-2}	$n_{40}(H_2)^1$ cm^{-3}	$M(r)^1$ $M_\odot$	r) $('')$	$N_r(H_2)^1$ cm^{-2}	$n_r(H_2)^1$ cm^{-3}	$M(120'')^1$ $M_\odot$	M(gradient T) $M_\odot$
1	0.000	0.057	266.349	-28.906	269.6	5.7E+21	1660.5	946.4	38.4	2.0E+22	826.8	1434.5	99.3
2	0.004	0.277	266.138	-28.788	292.3	6.2E+21	1800.3	1983.6	79.6	4.2E+22	193.7	1410.4	137.0
3	0.006	-0.135	266.540	-29.001	312.2	6.6E+21	1922.7	2002.0	82.1	4.2E+22	178.3	1975.1	112.9
4	0.010	0.157	266.258	-28.846	861.3	1.8E+22	5304.9	5037.0	81.4	1.1E+23	459.8	3310.2	364.7
5	0.016	-0.017	266.431	-28.931	1755.1	3.7E+22	10810.8	15522.4	93.2	3.3E+23	945.7	8845.2	588.0
6	0.018	-0.431	266.837	-29.144	114.9	2.4E+21	707.9	217.1	33.0	4.6E+21	297.7	271.0	56.2
7	0.020	0.033	266.385	-28.902	1172.0	2.5E+22	7218.8	8606.9	77.2	1.8E+23	922.9	6892.9	425.0
8	0.020	-0.051	266.467	-28.946	1620.4	3.4E+22	9980.5	9038.2	62.3	1.9E+23	1841.8	8159.9	540.3
9	0.022	0.251	266.174	-28.786	140.5	3.0E+21	865.2	367.5	33.0	7.8E+21	503.9	614.4	64.8
10	0.034	-0.437	266.852	-29.134	89.4	1.9E+21	550.6	157.5	33.0	3.3E+21	216.0	254.0	43.9

Note. — [1] Assuming a dust temperature of 20 K. [2] This is only a sample table containing 10 entries. The electronic version of this paper contains 1428 entries.